

Copyright  
by  
Igor Shovkun  
2018

The Dissertation Committee for Igor Shovkun  
certifies that this is the approved version of the following dissertation:

**Coupled chemo-mechanical processes in reservoir geomechanics**

Committee:

---

David Nicolas Espinoza, Supervisor

---

Mukul M. Sharma

---

John T. Foster

---

Matthew T. Balhoff

---

Marc E. Hesse

**Coupled chemo-mechanical processes in reservoir geomechanics**

**by**

**Igor Shovkun**

**DISSERTATION**

Presented to the Faculty of the Graduate School of  
The University of Texas at Austin  
in Partial Fulfillment  
of the Requirements  
for the Degree of

**DOCTOR OF PHILOSOPHY**

THE UNIVERSITY OF TEXAS AT AUSTIN

May 2018

Dedicated to my wife Maria.

## Acknowledgments

Prima facea, I would like to express the deepest appreciation to my adviser, Dr. Nicolas Espinoza, who guided me through the long road of my PhD program and gave me enough freedom to satisfy my scientific curiosity. Without his supervision and persistent efforts, this dissertation would not have been possible.

I would like to extend my deep appreciation to Professor Mukul M. Sharma. His efforts provided me with an extensive knowledge on hydraulic fracturing, as well as an opportunity to gain industry exposure via his Hydraulic Fracturing and Sand Control JIP.

I would like to thank my committee members, Professor Matthew T. Balhoff and Professor Marc A. Hesse , whose work provided me with ideas for my research and served as a benchmark of excellence. I owe a great deal to Professor Foster who opened to me the frontiers of numerical methods.

Finally, I take this opportunity to express the profound gratitude to my beloved wife, Maria, for being with me through thick and thin, believing in me, and being patient to my engineering eccentricity.

# **Coupled chemo-mechanical processes in reservoir geomechanics**

Igor Shovkun, Ph.D.

The University of Texas at Austin, 2018

Supervisor: David Nicolas Espinoza

Reservoir geomechanics investigates the implications of rock deformation, strain localization, and failure for completion and production of subsurface energy reservoirs. For example, effective hydraulic fracture placement and reservoir pressure management are among the most important applications for maximizing hydrocarbon production. The correct use of these applications requires understanding the interaction of fluid flow and rock deformations. In the past a considerable amount of effort has been made to describe the role of poroelastic and thermal effects in geomechanics. However, a number of chemical processes that commonly occur in reservoir engineering have been disregarded in reservoir geomechanics despite their significant effect on the mechanical behavior of rocks and, therefore, fluid flow.

This dissertation focuses on the mechanical effects of two particular chemical processes: gas-desorption from organic-rich rocks and mineral dissolution in carbonate-rich formations. The methods employ a combination of laboratory studies, field data analysis, and numerical simulations at various length scales.

The following conclusions are the results of this work: (1) the introduced numerical model for fluid flow with effects of gas sorption and shear-failure-impaired permeability captures the complex permeability evolution during gas production in coal reservoirs; the simulation results also indicate the presence non-negligible sorption stresses in shale reservoirs, (2) mineral dissolution of mineralized fractures, similar to pore pressure depletion or thermal cooling/heating can increase stress anisotropy, which can reactivate critically-oriented natural fractures; in-situ stress chemical manipulation can be used advantageously to enlarge the stimulated reservoir volume, (3) semicircular bending experiments on acidized rock samples show that non-planar fractures follow high porosity regions and large pores, and that fracture toughness correlates well with local porosity. Numerical modeling based on the Phase-Field approach shows that a direct relationship between fracture toughness and porosity permits replicating fracture stress intensity at initiation and non-planar fracture propagation patterns observed in experiments, and (4) numerical simulations based on a novel reactive fluid flow model coupled with geomechanics show that mineral dissolution (i) lower fracture breakdown pressure, (ii) can bridge a transition from a toughness-dominated regime to uncontrolled fracture propagation at constant injection pressures, and (iii) can increase fracture complexity by facilitating propagation of stalled fracture branches.

The understanding of these chemo-mechanical coupled processes is critical for safe and effective injection of CO<sub>2</sub> and reactive fluids in the subsurface, such as in hydraulic fracturing, deep geothermal energy, and carbon geological sequestration applications.

# Table of Contents

<b>Acknowledgments</b>	<b>v</b>
<b>Abstract</b>	<b>vi</b>
<b>List of Tables</b>	<b>xii</b>
<b>List of Figures</b>	<b>xiii</b>
<b>Chapter 1. Introduction</b>	<b>1</b>
1.1 Natural chemo-mechanical coupled processes in rocks . . . . .	1
1.2 Chemo-poro-mechanical processes in petroleum engineering applications . . . . .	2
1.3 Outline of the dissertation . . . . .	4
<b>Chapter 2. sorption</b>	<b>6</b>
2.1 Introduction . . . . .	6
2.2 Model development . . . . .	11
2.2.1 Poromechanical model with sorption stress . . . . .	11
2.2.2 Fluid mass balance and flow . . . . .	13
2.2.3 Stress-dependent permeability model . . . . .	15
2.3 Numerical solution method . . . . .	17
2.3.1 Solution algorithm . . . . .	17
2.3.2 Finite Element implementation . . . . .	18
2.4 Validation . . . . .	18
2.4.1 Stresses in the vicinity of hydraulic fractures . . . . .	18
2.4.2 Gas flow . . . . .	19
2.4.3 Stress path . . . . .	20
2.5 Case studies . . . . .	20
2.5.1 San Juan coal basin . . . . .	20

2.5.1.1	Stress-dependent permeability: fracture compressibility only . . . . .	23
2.5.1.2	Stress-dependent permeability: fracture compressibility, dilation and shear failure . . . . .	28
2.5.2	Barnett shale . . . . .	30
2.6	Discussion . . . . .	33
2.6.1	Parametric analysis of the model with fracture compressibility only . . . . .	33
2.6.2	Parametric analysis of the model with shear failure . . . . .	38
2.6.3	Gas sorption stresses in shales . . . . .	40
2.7	Conclusions . . . . .	41
<b>Chapter 3. dissolution</b>		<b>45</b>
3.1	Introduction . . . . .	45
3.2	Analytical model of stress relaxation induced by localized mineral dissolution . . . . .	49
3.2.1	Dissolution of a single vein . . . . .	50
3.2.2	Critical amount of carbonates to attain shear reactivation . . . . .	53
3.3	Experimental evidence of stress relaxation . . . . .	55
3.3.1	Rock sample . . . . .	55
3.3.2	Procedure . . . . .	56
3.3.3	Vein dissolution results . . . . .	58
3.3.3.1	Constant deviatoric stress . . . . .	58
3.3.3.2	Constant total vertical stress . . . . .	59
3.4	Reservoir scale simulation . . . . .	60
3.4.1	Analogy of mineral dissolution with anisotropic thermal cooling . . . . .	60
3.4.2	Case problem . . . . .	63
3.4.2.1	State of stresses during consecutive fracturing . . . . .	63
3.4.2.2	State of stresses during alternate fracturing and stress reorientation . . . . .	65
3.4.2.3	Reactivation of natural fractures due to acidizing . . . . .	68
3.5	Discussion . . . . .	70
3.5.1	Uniform dissolution versus etching . . . . .	70

3.5.2	Reactive fluid flow modeling . . . . .	71
3.5.3	Impact of stress relaxation on permeability . . . . .	72
3.6	Conclusion . . . . .	73
<b>Chapter 4.</b>	<b>Fracture propagation in heterogeneous porous media: pore-scale implications of mineral dissolution</b>	<b>76</b>
4.1	Introduction . . . . .	76
4.2	Experimental determination of fracturing behavior . . . . .	79
4.2.1	Methods . . . . .	80
4.2.1.1	Rock samples . . . . .	80
4.2.1.2	Acidizing procedure . . . . .	80
4.2.1.3	Semicircular bending experiments . . . . .	81
4.2.1.4	X-ray microtomography and image processing . . . . .	82
4.2.2	Experimental results . . . . .	83
4.3	Numerical modeling of fracture initiation and propagation . . . . .	86
4.3.1	Phase-field method . . . . .	86
4.3.2	Material properties: Toughness mapping . . . . .	87
4.3.3	Phase-field fracture simulation results . . . . .	88
4.3.3.1	Homogeneous samples: fracture toughness from peak load in SCB experiments . . . . .	88
4.3.3.2	Heterogeneous samples: fracture propagation . . . . .	92
4.4	Discussion . . . . .	97
4.4.1	The impact of the toughness-porosity relation on fracture propagation . . . . .	97
4.4.2	Fracture propagation with heterogeneous maps of Young's modulus and fracture toughness . . . . .	99
4.4.3	Extension to reactive fluid flow models coupled with geomechanics . . . . .	103
4.4.4	Comparison with previous work, other methods and fluid-driven modeling approaches . . . . .	105
4.4.5	Implications to natural and engineering geosystems . . . . .	107
4.5	Conclusions . . . . .	108

<b>Chapter 5. Propagation of toughness-dominated fluid-driven fractures in reactive porous media</b>	<b>110</b>
5.1 Introduction . . . . .	110
5.2 A coupled phase-field model for fluid-driven fractures in reactive poroelastic media . . . . .	114
5.2.1 Mechanics formulation . . . . .	115
5.2.2 Fluid mass balance and flow . . . . .	116
5.2.3 Reactive flow modeling . . . . .	117
5.2.4 Toughness-porosity model . . . . .	118
5.2.5 Numerical solution method . . . . .	119
5.2.6 Validation . . . . .	120
5.3 Results . . . . .	124
5.3.1 Mineral dissolution-assisted fracture propagation . . . . .	125
5.3.2 Sensitivity analysis . . . . .	129
5.4 Discussion . . . . .	133
5.4.1 Extension to fully-coupled reactive flow including modeling of wormholes . . . . .	133
5.4.2 Experimental validation . . . . .	135
5.4.3 Applications for acid fracturing in tight formations . . . . .	136
5.5 Conclusions . . . . .	137
<b>Chapter 6. Conclusions</b>	<b>139</b>
<b>Bibliography</b>	<b>143</b>

## List of Tables

2.1	Simulation parameters and initial conditions. (*) Assumed, (**) Best fit. . . . .	25
2.2	Simulation parameters used in history matching of the data from San Juan coal using the model with shear failure. (*) Best fit. . . . .	29
3.1	Typical in-situ stresses, shale properties and multi-stage hydraulic fracturing geometry for the Barnett Shale . . . . .	64

## List of Figures

2.1	Typical values of Young's moduli and maximum volumetric sorption-induced swelling strains in various organic shale and coal reservoirs. . . . .	10
2.2	Validation of the numerical model. (a) Stresses profile along x-axis starting from the center of the fracture. (b) Stress profile along y-axis starting from the fracture tip. (c) Pressure profile as a function of distance from the wellbore. (d) Total horizontal stress path predicted by plane strain and pseudo 3D linear poroelasticity (used in the study) models. . . . .	21
2.3	History matching of field data from a CBM well in Fruitland coal [130] using fracture compressibility only (no dilation/failure) and shear failure with fracture dilation and fines migration cases. (a) Production rates. (b) Average reservoir permeability evolution. (c) Bottom-hole and average reservoir pressure as functions of time. . . . .	24
2.4	Near-fracture and far-field evolution of coal-seam permeability and stresses considering fracture compressibility only. (a) Permeability as a function of time near fracture and far from the fracture. (b) Permeability as a function of pore pressure near fracture and far from the fracture. (c) Reservoir Biot effective stresses as a function of pore pressure near fracture and far from the fracture. . . . .	26
2.5	Near-fracture and far-field evolution of permeability in the case with shear failure and fracture dilation. (a) Temporary permeability profiles near fracture and far from the fracture. (b) Permeability as a function of pore pressure near fracture and far from the fracture. . . . .	31
2.6	History matching of the field data from the Barnett shale. (a) Comparison of production gas rates and cumulative production for the cases with zero and non-zero sorption stress. (b) Near-fracture and far-field permeabilities as a function of time for the cases with zero and non-zero sorption strains. . . . .	34
2.7	Effective stresses as a function of time for the cases with zero and non-zero desorption-induced strains in the vicinity of the hydraulic fracture. Swelling strains lower compressive horizontal effective stress $\sigma_{xx}$ . . . . .	35

2.8	Sensitivity analysis of stress-dependent permeability model considering only fracture compressibility. Base case: $\alpha_H = 0.2 \text{ MPa}^{-1}$ , $k_{H0} = 80 \text{ mD}$ , $x_f = 70 \text{ m}$ , $\partial p_w / \partial t = 2.76 \text{ kPa/day}$ . Parameters from San Juan coal basin. (a) Sensitivity study to fracture compressibility $\alpha_H$ . (b) Sensitivity study to reference permeability $k_{H0}$ . (c) Sensitivity study to fracture half-length $x_f$ . (d) Sensitivity study to wellbore schedule. . . . .	37
2.9	Sensitivity analysis of stress-dependent permeability model considering shear failure. Parameters from San Juan coal basin. Base case: $\gamma = 0.45 \text{ MPa}^{-1}$ , $\kappa = 10^{-4} \text{ s/m}$ , $C = 1.38 \text{ MPa}$ . (a) Sensitivity study to fracture dilation coefficient $\gamma$ (b) Sensitivity study to permeability degradation parameter $\kappa$ (c) Sensitivity study to cohesive strength $C$ . . . . .	39
2.10	Sorption isotherms for San Juan coal and Devonian and Barnett shales. (a) Volume of adsorbed methane (at standard conditions) per unit volume of rock matrix as a function of pore pressure. (b) Swelling sorption-induced strains in San Juan coal and Niutitang and Barnett shales as functions of pore pressure. (c) Product of the rock's bulk modulus and the maximum swelling strain $K \cdot \varepsilon_L$ as a function of the maximum swelling strain $\varepsilon_L$ for various shales and coals. . . . .	42
3.1	Different modes of calcite occurrence in shales. (a) Carbonates (CB) in the matrix (after [208]). In the lower half of the image one can see a substantial area occupied by carbonates. Carbonates can also localize in the matrix forming rings and islands. They can share mixed regions with organic matter (OM) and clays. (b) Calcites in a form of veins. Carbonate-rich regions can span for several inches (after [65]). (c) Interaction of a open-mode fracture with a mineralized vein (after [108]). When hitting a natural fracture, an open-mode fracture may deviate and start propagating in the direction of the vein. . . . .	46
3.2	(a) Schematic representation of tight formation with a set of parallel mineralized fractures and abundant natural fractures subjected to in-situ stresses. (b) Representative elementary volume, where $\alpha$ is the dip of the mineralized fractures, $h$ is the thickness, $L$ is the spacing between fractures, $E$ is the shale Young's modulus, and $\nu$ is the shale Poisson's ratio. . . . .	49
3.3	Effect of mineral dissolution. (a) Calcite veins dissolve and shale expands due to Poisson's effect. (b) Change of effective stresses with dissolution. Perfect plasticity assumed: the red marker designates a perfect plastic yield transition. (c) Change of stress state represented as a movement of the respective Mohr's circle. At the plastic transition point the circle is tangent to the failure envelope. . . . .	53

3.4	Minimum volume fraction of calcite veins in shale necessary to attain reactivation of critically-oriented natural fractures assuming full dissolution and vein strike perpendicular to $S_h$ . (a) Impact of Young's modulus: less calcite is to be dissolved to reactivate fractures in a stiff shale. (b) Impact of pore pressure: less calcite is required to be dissolved to fail an overpressured shale. . . . .	55
3.5	Vein dissolution experiments monitoring axial and deviatoric stresses, confining pressure, and horizontal strain as functions of time. Stages: (I) before dissolution commences, (II) during dissolution while lateral strain is maintained constant, (III) vertical and horizontal stresses are held, sample contracts as a result of dissolution. (a) Constant deviatoric stress experiment. (b) Constant vertical stress experiment. . . . .	57
3.6	Minimum horizontal effective stress as a function of decrease in reservoir temperature and volume fraction of carbonates in veins. Anisotropic thermal cooling and mineral dissolution have similar effects on horizontal stress. Thermal expansion coefficient can be used to estimate an equivalent volume fraction of carbonates. . . . .	63
3.7	Effect of dissolution in a consecutive fracturing application. Total horizontal stresses in the near-fracture and far-field (at 400 ft) regions as functions of a distance traveled by a dissolution front. (a) Isotropic case - 2 sets of veins oriented perpendicular and parallel to $S_h$ . One can see both reduction in $S_{xx}$ and $S_{yy}$ . (b) Veins are oriented parallel to $S_h$ . Only $S_{yy}$ decreases. (c) Veins are oriented perpendicular to $S_h$ . Only $S_{xx}$ decreases. . . . .	66
3.8	Alternate fracturing. (a) Veins are oriented perpendicular to $S_h$ . Initially higher $S_{xx}$ (because of stress shadows) drops below $S_{yy}$ due to acidizing. Without acidizing a new fracture placed in the middle would propagate in x-direction instead of y-direction. (b) Veins are oriented parallel to $S_{hmin}$ . Initially low $S_{yy}$ reduces below $S_h$ . A new fracture always propagates in x-direction. . . . .	69
3.9	Alternate fracturing: effect of mineral dissolution on critically-oriented natural fracture reactivation. Vertical mineralized veins with strike $\beta = 45^\circ$ and dip $\alpha = 90^\circ$ . (a) Total vertical and horizontal stresses as functions of the overall amount of dissolution. (b) Mohr's circle corresponding to the stress state before dissolution and the shear failure point. . . . .	70

4.1	$\mu$ CT images of Indiana Limestone sample subjected to acidizing and SCB testing. (a) Full core oriented vertically before cutting. Black color indicates the voids (wormhole), the rock matrix is transparent, the red rectangle shows the outer contour of the cylindrical sample. (b-d) $\mu$ CT images of the horizontal slices after SCB testing (left) and processed images with fractures highlighted in blue: (b) high amount of dissolution end-member, (c) moderate amount of dissolution case, and (d) negligible amount of dissolution end-member. . . . .	84
4.2	(a) SCB Experimental loading results: the load on the sample as a function of the top-roller displacement. (b) Fracture toughness obtained from SCB experiments as a function of rock macro-porosity from X-ray $\mu$ CT image processing. The relationship indicates a clear trend of toughness reduction with an increase in porosity. Blue circles indicate slices taken from the “top” of the sample, which corresponds to the acid injection point. These samples feature high amounts of mineral dissolution (similar to the sample in Fig. 4.1b). Green squares indicate slices taken from the “middle” of the sample: they still contain the wormhole but are farther from the injection point than the samples shown with blue circles. Red squares indicate the slices taken from the “bottom” of the sample: they have negligible amounts of mineral dissolution. . . . .	85
4.3	Image processing workflow for setting material property distribution for numerical simulation. (a) Mineral/void binary image obtained from $\mu$ CT scan with a threshold value. (b) Porosity map obtained with a Gaussian blur filter. (c) Fitted toughness-porosity experimental data. (d) Toughness map. . . . .	89
4.4	Schematics for the SCB numerical simulation. The point at the top of the sample moves down at a fixed displacement rate. The two points at the bottom equidistant from the notch have fixed y-displacement. Additionally, the left point at the bottom has fixed x-displacement. . . . .	90
4.5	Sensitivity study SCB simulation. (a) Sensitivity to fracture toughness $K_{IC}$ . High fracture toughness results in high values of the peak load. (b) Sensitivity to Young’s modulus $E$ . High Young’s modulus values result in steep slope of the loading curve. . . . .	91
4.6	Comparison of two experimental SCB loading curves with numerical simulation. The fracture toughness values obtained from the experimental loading curves are $K_{IC}^* = 0.34 \text{ MPa} \sqrt{\text{m}}$ and $0.23 \text{ MPa} \sqrt{\text{m}}$ for the red and green lines, respectively. . . . .	93

4.7	Comparison of fracture propagation in a SCB experiments with numerical simulations in heterogeneous media: $\mu$ CT image of the fracture in the laboratory experiment (left) and fracture path ( $\varphi < 0.15$ shown in red) obtained from numerical simulation superimposed on the numerical model based on the $\mu$ CT image (right). (a) Sample with a high amount of dissolution. (c) Sample with a moderate amount of dissolution. (d) Sample with a negligible amount of dissolution. . . . .	96
4.8	The impact of the toughness-porosity relation on fracture propagation. (a) A $\mu$ CT image of a fractured rock sample with low amount of dissolution. (b) Toughness-porosity functions used to obtain the distribution of fracture toughness $K_{IC}$ for numerical simulations. (c-g) The results of numerical simulations with various toughness distributions as input. (c) Case I. Fracture toughness is obtained with a concave-up relation that fits the experimental data. Numerical simulation matches well the experimental data. (d) Case II. Fracture toughness depends linearly on local macro-porosity. The fracture geometry is similar to that in case I but deviates more from the experimentally-observed fracture. (e) Case III. Fracture toughness is a concave-down function of porosity. The fracture geometry is nearly-planar due to nearly-homogeneous toughness distribution in the domain. (f-g) Case IV. Fracture toughness is distributed uniformly within the sample. The fracture is nearly-planar in (f) and is planar in (g) computed on a twice-finer mesh. . . . .	98
4.9	Correlation of Young's modulus with limestone porosity used in the numerical simulations (after [38]). . . . .	100
4.10	Comparison of fracture propagation in a SCB experiments with numerical simulations in heterogeneous media: the effect of heterogeneous distribution of fracture toughness $K_{IC}$ and Young's modulus $E$ . (a) $\mu$ CT image of a SCB sample with a moderate amount of dissolution. (b-d) The results of numerical simulations with heterogeneous material properties. Fracture path ( $\varphi < 0.15$ ) obtained from numerical simulation is superimposed on the distribution of (b) fracture toughness and (c-d) Young's modulus in the domain. (b) Variable fracture toughness $K_{IC}$ only: the simulation repeats the experimental fracture path. (c) Variable Young's modulus $E$ only: the fracture avoids high-porosity regions. (d) Variable fracture toughness $K_{IC}$ and Young's modulus $E$ : the simulation repeats the experimental fracture path. . . . .	102
5.1	Regimes of fluid-driven fracture propagation. (after [24]). . . . .	112

5.2	Comparison of FEM phase-field numerical simulations with analytical solutions. (a) Aperture of a static pressurized fracture as a function of x-coordinate compared to Sneddon's solution. (b) Pore pressure as a function of distance from the fracture tip and comparison with Darcy flow for steady state solution of wellbore equation. (c) Pressure in the fracture center as a function of time. Comparison of the breakdown pressure with Sneddon's solution. Comparison of the pressure decline after the breakdown with the KGD solution. (d) Comparison of the fracture half-length in the numerical simulation with the KGD model. . . . .	122
5.3	Schematics of a domain with a fracture with half-length $x_f$ . Acid is injected with constant injection pressure $p^{inj}$ which results in stress intensity $K_I$ at the fracture tip. The intact rock has fracture toughness $K_{IC}^0$ . . . . .	125
5.4	(a) An ideal case of mineral-dissolution-assisted fracture propagation with an infinite reaction rate and infinitely slow fracture growth. Fracture toughness and stress intensity at the fracture tip as functions of fracture half-length. Initially high fracture toughness at the tip of the fracture reduces due to mineral dissolution caused by acid leak-off until it reaches the value of tip stress intensity. Fracture starts propagating with the help of dissolution in a toughness-dominated regime with fracture toughness at the tip being approximately equal to stress intensity. At the critical length $x_f^* = 0.77$ m stress intensity equals the intact rock toughness, and the fracture engages in uncontrolled propagation. (b) The results of “near-reach” (high acid power) and “far-reach” (low acid power) numerical simulations of the poroelastic model coupled with phase-field and single-component reactive fluid flow. Reaction rates are the same in both cases. . . . .	128
5.5	Phase-field, pressure, dimensionless HCl concentration, and toughness at various time instants for two simulation cases: the onset of propagation, time when $x_f = 1$ m, time when $x_f = 2$ m. The phase-field and pressure distributions are approximately the same at the chosen times for each simulation case. The toughness images show superimposed phase-field maps with $\varphi < 0.2$ for visual aid of fracture length. . . . .	130
5.6	Fracture half-length as a function of time. Base case: $\tilde{\alpha}_s = 10^2$ m <sup>3</sup> /mol and $\tilde{k}_s = 10^{-4}$ s <sup>-1</sup> . (a) Sensitivity to effective reaction rate $\tilde{k}_s$ . (b) Sensitivity to effective dissolving power $\tilde{\alpha}_s$ . . . . .	132
5.7	The width of the high-concentration region as a function of the effective reaction rate $\tilde{k}_s$ . . . . .	132

5.8	An example of an experimental setup to explore the effects of acid injection on break-down pressure. . . . .	135
5.9	Acid-assisted fracture propagation. . . . .	137

# **Chapter 1**

## **Introduction**

### **1.1 Natural chemo-mechanical coupled processes in rocks**

Chemo-mechanical processes play a key role in rock diagenesis [78]. Geochemical reactions are specific to rock type and brine chemistry with mineral reactions that depend on temperature and vary over a wide range of time scales [162, 184]. These chemical reactions, often irreversibly, alter pore pressure, the rock skeleton and stress-bearing solid members. As a consequence, various mechanical processes may be triggered such as rock compaction, alteration of cohesive and shear strength, changes in fracture toughness and fracture propagation velocity, overpressure, swelling stresses and strains, stress relaxation, microfracturing, and induced seismicity [177, 101, 118, 53, 43, 213, 186]. Unlike temperature or pore-pressure-induced mechanical effects, chemical processes involve reactions with various time scales and rates, affect specific parts of the rock solid skeleton, and require combined reactive diffusion-advection formulations to predict large-scale phenomena. Examples of naturally occurring chemo-mechanical coupled processes include pressure solution creep, stylolites, and fracture propagation induced by crystallization pressure [162, 48, 16].

## 1.2 Chemo-poro-mechanical processes in petroleum engineering applications

The following competitive geomechanical processes are known to affect stresses in reservoirs during drilling, completion, and production: pressure depletion, temperature changes, chemically-induced strains, and biologically-mediated changes of pore pressure and rock skeleton.

Decreases in pore pressure associated with reservoir depletion cause increases in effective stresses, which often lead to fracture closure and a decrease in permeability [74, 220]. For example, linear isotropic poroelasticity predicts Biot effective vertical stress  $\sigma_v$  to change  $\Delta\sigma_v = -b\Delta p$  and Biot effective horizontal stress  $\sigma_h$  to change  $\Delta\sigma_h = -\frac{\nu}{1-\nu}b\Delta p$  with a change of pressure  $\Delta p$  (negative for depletion) in a horizontally extensive reservoir with constant total vertical stress, where  $b$  is the Biot coefficient and  $\nu$  is the Poisson ratio [167]. Depletion causes maximum horizontal effective stress  $\sigma_{Hmax}$  and minimum horizontal effective stress  $\sigma_{hmin}$  to change the same amount, assuming that the medium is homogeneous and isotropic and equally-sized in both horizontal directions. These equations are applicable for small strains. At large strains, shear failure may also limit stresses. Anisotropic changes of effective stresses induced by depletion have the potential to reactivate and create new fractures in shear, both within and outside the reservoir in some geologic environments [75]. At shear yield, stresses are no longer controlled by linear poroelasticity but by the frictional strength of the formation [93, 220]. These changes have been measured in the field as changes of total stresses (total stress rather than effective stress is measured in the field) [74, 192, 30]. Varia-

tions in reservoir geometry, caprock stress arching and poroximity to faults, among others, can modify changes of stresses in the reservoir and induce stress reorientation [168, 154]. There have been a number of case studies in which both fluid withdrawal and fluid injection appear to have induced fault reactivation in oil and gas reservoirs [75, 223, 159, 221, 91]. Since total vertical stress  $S_v$  is expected to remain essentially constant during depletion of laterally extensive reservoirs, reservoir depletion may change the faulting regime of the reservoir, especially if it was not originally homogeneous throughout it such as in anticlines with residual flexural stresses [192, 220].

Changes in reservoir temperature due to the injection of fluids with temperature different from the reservoir temperature can induce thermal stresses. For example, the injection of hot water results in compressive stresses, which play a substantial role in geothermal applications [167]. During cold-water or cold-CO<sub>2</sub> injection, in contrast, the formation temperature around the wellbore decreases resulting in decreases in reservoir effective stresses (less compressive) and, as a consequence, a lower fracture gradient and reduced reservoir stresses [1, 32, 100, 91]. The equations governing this process are dictated by the theory of thermoporoelasticity, but sometimes are simplified to thermoelasticity for numerical simulations [71, 220]. The thermomechanical effects of fluid injection depend on the difference between the temperatures of the injected and reservoir fluids, injection times, and thermal and mechanical properties of the geological formation such as thermal conductivity, volumetric heat capacity, thermal expansion coefficient, and Young's modulus [109, 35, 169].

Geomechanical alterations in oil and gas reservoirs during depletion may be also induced by the changes in chemical potential of the reservoir fluid. For example, aqueous composition of the drilling mud or injected fluid different from that of the formation has been known to cause clay swelling that results in increased compressive stresses and a decrease in permeability [189]. Another chemo-mechanical process that may affect the stresses in a reservoir is gas desorption. In contrast to pore pressure depletion, desorption and matrix shrinkage result in a drop in effective stresses and an increase in fracture permeability [173, 137, 140]. Additionally, decrease of effective horizontal stress gives rise to high ratio of vertical to horizontal stress and potential shear failure [128, 130, 54]. Strains in a reservoir can be induced by mineral dissolution as well, which may take place during the acidizing of calcite-rich rocks [177].

### 1.3 Outline of the dissertation

This dissertation is organized into four central chapters. Chapter 2 presents a coupled reservoir model that includes the impact of sorption-induced stresses and permeability impairment caused by shear failure. This model is used to analyze and compare two field cases with strong and weak chemo-mechanical coupling.

Chapter 3 discusses reservoir-scale geomechanical implications of chemical dissolution of mineralized fractures in carbonate-rich shale reservoirs. A combination of elasto-plastic analytical methods, analogous thermo-elastic solutions, and laboratory experiments is used to quantify changes of local in-situ stresses due to mineral dissolution.

Chapter 4 investigates the effect of mineral dissolution on rock mechanical properties and fracture propagation and proposes a coupling mechanism for reactive fluid flow in porous media with geomechanics. Semicircular bending experiments, X-Ray Microtomography and image processing, and Finite-Element numerical simulations based on the phase-field approach and linear elastic fracture mechanics are used to investigate open-mode fracture propagation in heterogeneous porous media altered by mineral dissolution.

Chapter 5 addresses the impact of reactive fluid leak-off during hydraulic fracturing and introduces a concept of acid-assisted fracture propagation. A novel advection-diffusion-reaction model is coupled with the previously-developed phase-field formulation for single-phase fluid flow and mechanics.

Finally, Chapter 6 summarizes the main conclusions of this work and potential research directions and engineering applications.

## Chapter 2

# Coupled fluid flow-geomechanics simulation in stress-sensitive coal and shale reservoirs: impact of desorption-induced stresses, shear failure, and fines migration <sup>1</sup>

### 2.1 Introduction

Natural gas consumption currently constitutes a fifth of the total energy sources [197]. About a half of non-associated gas accrues to non-conventional gas reservoirs, mainly organic shales and coal seams [194]. Non-conventional tight reservoirs have an extremely low matrix permeability, with natural fractures often acting as main fluid conduits. The openings of these fractures are dictated by lithology and in-situ stresses, which may alter during reservoir development [146, 220, 50, 160]. The following competitive geomechanical processes are known to affect stresses during depletion in fractured reservoirs: pressure depletion, temperature changes, and chemically-induced strains, among others.

Decreases in pore pressure associated with reservoir depletion cause increases in effective stresses, which often leads to fracture closure and a decrease

---

<sup>1</sup> Igor Shovkun and D. Nicolas Espinoza. Coupled fluid flow-geomechanics simulation in stress-sensitive coal and shale reservoirs: Impact of desorption-induced stresses, shear failure, and fines migration. Fuel, 195, 260-272. (2017) All authors contributed equally.

in permeability [74, 220]. For example, linear isotropic poroelasticity predicts Biot effective vertical stress  $\sigma_v$  to change  $\Delta\sigma_v = -b\Delta p$  and Biot effective horizontal stress  $\sigma_h$  to change  $\Delta\sigma_h = -\frac{\nu}{1-\nu}b\Delta p$  with a change of pressure  $\Delta p$  (negative for depletion) in a horizontally extensive reservoir with constant total vertical stress, where  $b$  is the Biot coefficient and  $\nu$  is the Poisson ratio [167]. If horizontal stresses differ, depletion would cause maximum horizontal effective stress  $\sigma_{Hmax}$  and minimum horizontal effective stress  $\sigma_{hmin}$  to change the same amount, assuming that the medium is homogeneous and isotropic. These equations are applicable for small strains. At large strains, shear failure may also limit stresses. Anisotropic changes of effective stresses induced by depletion have the potential to reactivate and create new fractures in shear, both within and outside the reservoir in some geologic environments [75]. At shear failure, stresses are no longer controlled by linear poroelasticity but by the frictional strength of the formation [93, 220]. These changes have been measured in the field as changes of total stresses (total stress rather than effective stress is measured in the field) [74, 192, 30]. Variations in reservoir geometry, caprock stress arching and proximity to faults, among others, can modify changes of stresses in the reservoir and induce stress reorientation [168, 154]. There have been a number of case studies in which both fluid withdrawal and fluid injection appear to have induced fault reactivation in oil and gas reservoirs [75, 223, 159, 221, 91]. In light of the fact that total vertical stress  $S_v$  is expected to remain essentially constant during depletion of laterally extensive reservoirs, reservoir depletion may change the faulting regime of the reservoir, especially if it was not originally homogeneous throughout the reservoir such as in anticlines with residual flexural stresses

[192, 220].

Changes in reservoir temperature due to the injection of fluids with temperature different from the reservoir temperature can induce thermal stresses. For example, the injection of hot water results in compressive stresses, which play a substantial role in geothermal applications [167]. During cold-water or cold-CO<sub>2</sub> injection, in contrast, the formation temperature around the wellbore decreases resulting in decreases in reservoir stresses (less compressive) and, as a consequence, a lower fracture gradient and reduced reservoir stresses [1, 91, 100, 32]. The equations governing this process are dictated by the theory of thermoporoelasticity, but sometimes are simplified to thermoelasticity for the numerical estimations [71, 220]. The thermomechanical effects of fluid injection depend on the difference between the temperatures of the injected and reservoir fluids, injection times, and thermal and mechanical properties of the geological formation such as thermal conductivity, volumetric heat capacity, thermal expansion coefficient, and Young's modulus [109, 35, 169].

Geomechanical alterations in oil and gas reservoirs during depletion may be also induced by the changes in chemical potential of the reservoir fluid. For example, aqueous composition of the drilling mud or injected fluid different from that of the formation has been known to cause clay swelling that results in increased compressive stresses and a decrease in permeability [189]. Strain in a reservoir can be induced by mineral dissolution as well, which may take place during the acidization of calcite-rich rocks [177]. Another chemo-mechanical process that may affect the stresses in a reservoir is gas desorption. Gas desorption is of significant impor-

tance in coals because sorbed gas constitutes more than 50% of total gas in place and desorption induces a substantial amount of rock shrinkage and effective stress relaxation [129, 150, 138]. Sorbed gas in hydrocarbon-bearing shales constitutes 5-15% of the total gas in place. Sorption capacity is usually proportional to total organic carbon (TOC) in shales [67]. In contrast to pore pressure depletion, desorption and matrix shrinkage result in a drop in effective stresses and an increase in permeability [137, 173, 140]. Additionally, decrease of effective horizontal stress gives rise to high ratio of vertical to horizontal stress and potential shear failure [128, 130, 54]. Desorption-induced changes of stresses have been modeled previously using an analogy with thermoelasticity [175, 139] and recently by using an extension of poromechanics to microporous media [21, 55]. Sorption-mechanical couplings depend on sorptive properties of the rock matrix as well as mechanical properties. Fig. 2.1 summarizes typical values of Young's moduli and maximum sorption-induced strains measured for various coal and organic-rich shale rocks [175, 55, 139, 31, 9, 86, 207]. of magnitude higher than those of coals. At the same time, maximum sorption-induced swelling strains in coals exceed sorption-induced strains in shales by about an order of magnitude. Since sorption swelling stress is proportional to the product of the bulk modulus and sorption strain (shown in Section 2.2.1), a soft coal exhibiting large sorption strains and a stiff shale exhibiting small sorption strains may cause sorption stresses of similar magnitude. To the best of our knowledge, there are no studies of the impact of sorption stresses on fracture permeability of shales conducted so far.

The objectives of this paper are to present a fully coupled reservoir model

for non-conventional natural gas engineering applications and to include the impact of sorption-induced stress changes and shear failure on long-term reservoir development via numerical simulation. We first introduce a model of a single phase gas flow coupled with linear elastic geomechanics accounting for sorption and then describe the numerical solution method. Second, we investigate production rates and permeability alterations due to changes in effective stresses induced by depletion by analyzing and comparing two field cases: San Juan Basin coal and Barnett shale gas reservoirs. Finally, we discuss the governing parameters of the permeability evolution due to geomechanical processes and highlight the limitations of a linear elastic formulation.

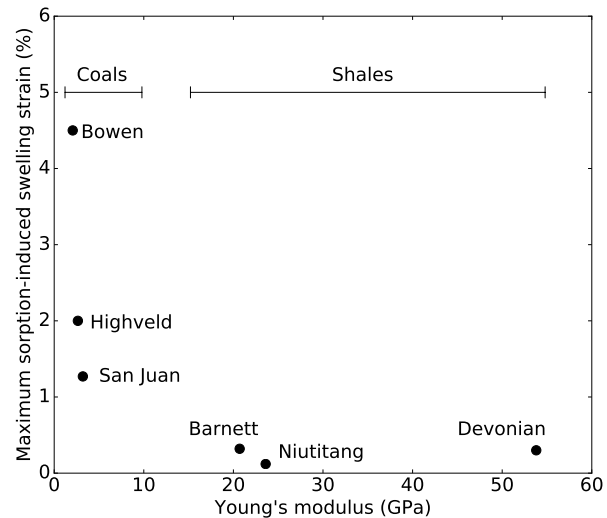


Figure 2.1: Typical values of Young's moduli and maximum volumetric sorption-induced swelling strains in various organic shale and coal reservoirs.

## 2.2 Model development

In this section we introduce the equations that describe single-phase ideal gas flow, coupled with linear elastic geomechanics in a sorptive medium. We first introduce a poromechanical model and then we derive the corresponding fluid flow equation. Last, we introduce a permeability model of an equivalent fractured medium accounting for fracture compressibility, shear dilation, and fine production from shear failure.

### 2.2.1 Poromechanical model with sorption stress

The equilibrium of stresses is dictated by Cauchy's equation:

$$\nabla \cdot \mathbf{S} = -\rho_b \vec{g}, \quad (2.1)$$

where  $\mathbf{S}$  is the total stress tensor,  $\rho_b$  is the bulk mass density of the rock, and  $\vec{g}$  is gravity acceleration. In porous media, effective stresses define the material deformation instead of the totals stresses. The following relation between total and effective stresses is valid for isotropic rocks with the typical values of porosity  $\phi \ll 1$ :

$$\mathbf{S} = \boldsymbol{\sigma} + bp\mathbf{I}, \quad (2.2)$$

where  $\boldsymbol{\sigma}$  is the effective stress tensor,  $p$  is pore pressure,  $b$  is the Biot coefficient of the rock mass, and  $\mathbf{I}$  is the unit tensor. The stress-strain relation for a linear isotropic poroelastic material with sorption-induced strains is written as follows:

$$\boldsymbol{\sigma} = \lambda \operatorname{tr}(\boldsymbol{\varepsilon}) + 2G\boldsymbol{\varepsilon} + \boldsymbol{\sigma}_s, \quad (2.3)$$

where  $\sigma$  is the effective stress tensor,  $\varepsilon$  is the small strain tensor,  $\lambda$  and  $G$  are the Lamé constants of the rock, and  $\sigma_s$  is a swelling stress tensor. Assuming constant total vertical stress  $S_{zz}$ , Eq. 2.3 can be written as follows:

$$\sigma = \begin{bmatrix} \sigma_{xx} \\ \sigma_{yy} \\ \sigma_{xy} \end{bmatrix} = \frac{1}{2G + \lambda} \begin{bmatrix} 4G(G + \lambda) & 2G\lambda & 0 \\ 2G\lambda & 4G(G + \lambda) & 0 \\ 0 & 0 & 2G(2G + \lambda) \end{bmatrix} \begin{bmatrix} \varepsilon_{xx} \\ \varepsilon_{yy} \\ \varepsilon_{xy} \end{bmatrix} + \begin{bmatrix} 1 \\ 1 \\ 0 \end{bmatrix} \left( \frac{S_{zz} - bp}{2G + \lambda} + \sigma_s \right) \quad (2.4)$$

Vertical components of displacement  $\vec{u}$  and stress and strain tensors are not included into the model explicitly, but can be obtained as follows:

$$u_z = h\varepsilon_{zz}; \quad \begin{cases} \varepsilon_{zz} = \frac{1}{E} [\sigma_{zz} - \nu(\sigma_{xx} + \sigma_{yy})] \\ \varepsilon_{xz} = \frac{1}{2} \left( \frac{\partial u_z}{\partial x} + \frac{\partial u_x}{\partial z} \right) \\ \varepsilon_{yz} = \frac{1}{2} \left( \frac{\partial u_z}{\partial y} + \frac{\partial u_y}{\partial z} \right) \end{cases}; \quad \begin{cases} \sigma_{zz} = S_{zz} - bp \\ \sigma_{xz} = 2G\varepsilon_{xz} \\ \sigma_{yz} = 2G\varepsilon_{yz} \end{cases} \quad (2.5)$$

where  $h$  is the formation thickness.

We assume swelling stresses to be isotropic, monotonically increasing according to Langmuir isotherm with respect to the asymptotic value of sorption-induced swelling strain  $\varepsilon_L$  [82, 31]:

$$\sigma_s = K\varepsilon_L \frac{p}{p + p_L} \mathbf{I}, \quad (2.6)$$

where  $p_L$  is the Langmuir pressure and  $K = \lambda + 2G/3$  is the elastic bulk modulus of the rock. A rigorous poromechanical derivation of the swelling stress tensor for anisotropic sorbing media is found elsewhere [56, 55]. Sorption stress is assumed to be a function of fluid pressure in fractures. This assumption may not hold under transient conditions.

### 2.2.2 Fluid mass balance and flow

The derivation of the fluid flow equation starts with a continuity equation including sorption into the rock matrix:

$$\frac{\partial [\phi \rho_f + (1 - \phi) \rho_{fsc} V_s \rho_m]}{\partial t} = \nabla (\rho_f \vec{q}), \quad (2.7)$$

where  $\phi$  is the rock porosity,  $\rho_f$  is the pressure-dependent fluid density,  $\rho_{fsc}$  is the fluid mass density at standard conditions,  $\rho_m$  is the rock matrix density,  $\vec{q}$  is fluid superficial velocity, and  $V_s$  is the volume of sorbed gas at standard conditions. Assuming a Langmuir behavior of the sorption isotherm, as in Eq. 2.6, we can write  $V_s$  as a function of pressure in fractures:

$$V_s = \frac{V_L p}{p + p_L}, \quad (2.8)$$

where  $V_L$  is Langmuir volume. Again, the pressure in the rock matrix may differ from that in fractures under transient conditions. In a compressible porous solid, variations of the porosity depend on the fluid pore pressure and the volumetric strain of the rock  $\varepsilon_V$  as follows [35]:

$$\phi - \phi_o = b \varepsilon_V + \frac{p}{N}, \quad (2.9)$$

where  $\phi_o$  is the initial porosity of the solid. A poroelastic modulus  $N$  and the Biot coefficient  $b$  are defined by the following expressions:

$$\begin{aligned} N &= \frac{K_s}{b - \phi_o} \\ b &= 1 - \frac{K}{K_s}, \end{aligned} \quad (2.10)$$

where  $K$  is the drained bulk modulus of the fractured rock mass and  $K_s$  is the bulk modulus of the rock matrix.

The first term on the right-hand side of Eq. 2.9 is a term that couples the effect of the rock deformations on mass balance. In the case of a gaseous fluid and Darcy flow, the right-hand side of Eq. 2.7 becomes [35]

$$\nabla(\rho_g \vec{q}) = \frac{\rho_g k}{2\mu} \frac{\nabla^2 p^2}{p}, \quad (2.11)$$

where  $k$  is the permeability of the rock,  $\mu$  is the fluid viscosity, and  $\rho_g$  is the fluid in-situ density. Using Eq. 2.8 to 2.11 and the equation of state of an ideal gas, Eq. 2.7 becomes

$$\begin{aligned} & \left( bp - bp_{sc}\rho_m V_L \frac{p}{p + p_L} \right) \frac{\partial \varepsilon_V}{\partial t} + \\ & \left[ \phi + \frac{p}{N} - \frac{p_{sc}\rho_m V_L}{N} \frac{p}{p + p_L} + (1 - \phi)p_{sc}\rho_m V_L \frac{p}{(p + p_L)^2} \right] \frac{\partial p}{\partial t} = \nabla \cdot \left( \frac{k}{2\mu} \nabla p^2 \right), \end{aligned} \quad (2.12)$$

where  $p_{sc}$  is the pressure at standard conditions (1 atm). In conjunction with the stress equilibrium equation Eq. 2.4, Eq. 2.12 completes the system. Eq. 2.12 can be expanded to real gases by considering the gas deviation factor. We neglect the real-gas behavior in our simulations because the ideal-gas approximation results in an approximately 4% error in density estimation within the bounds reservoir pressure for each considered case. This estimate was obtained from the data provided by NIST and assuming constant reservoir temperature 80°[114].

### 2.2.3 Stress-dependent permeability model

Porosity-permeability models commonly used in reservoir simulation are not accurate enough for describing variations of permeability in fractured media due to the strong non-linear dependence of the permeability on the reservoir stress state. Instead of conventional permeability models, we use the following empirical relationship for horizontal permeability  $k_H$  [161]:

$$k_H = k_{Hr} + k_{H0} \exp(-\alpha_H \Delta\sigma_H - \alpha_V \Delta\sigma_V) \quad (2.13)$$

where  $k_{Hr}$  is the residual fracture permeability,  $k_{H0}$  is the reference value for reservoir permeability,  $\alpha_H$  and  $\alpha_V$  are horizontal and vertical fracture compressibility, respectively,  $\Delta\sigma_H = \bar{\sigma}_H - \sigma_{H0}$  is the difference between the current mean Terzaghi horizontal stress  $\bar{\sigma}_H$  and a reference value  $\sigma_{H0}$ ,  $\Delta\sigma_V = \sigma_V - \sigma_{V0}$  is the difference between the current Terzaghi vertical stress  $\sigma_V$  and a reference value  $\sigma_{V0}$ . Fracture compressibility parameters depend on the asperities of fractures, rock ductility, and the presence of proppants [203, 214]. Note that variations of stresses can impart anisotropic changes of permeability [128]. We limit the discussion here to horizontal permeability and consider it equal in any horizontal direction.

The permeability model proposed in the study also accounts for shear failure and permeability deterioration due to fines migration and clogging. We adopt a simple shear failure criterion

$$\tau = C + \sigma_n \tan(\varphi), \quad (2.14)$$

where  $\tau$  is shear effective stress,  $\sigma_n$  is normal effective stress,  $C$  is the cohesive strength of the rock, and  $\varphi$  is the internal friction angle.

When the shear stresses at a location in the reservoir surpass a Mohr-Couloumb failure envelope, the permeability at that location is controlled by shear fracture dilation and fines accumulation (we assume brittle and stress-softening rocks, hence, shear bands and self-healing are discarded [37, 196, 120]). We assume that permeability after failure is affected by the product of a deterioration factor  $D$  and shear dilation factor  $S$  as follows:

$$k_H = k_{Hf} DS, \quad (2.15)$$

where  $k_{Hf}$  is horizontal permeability immediately before failure. According to several experimental studies, permeability can decay exponentially with the amount of produced fluid during fines generation [41, 79]. The field data from San Juan coal basin, analyzed later in Section 2.5.1 also suggests an exponential decrease of field permeability with time associated with fines migration upon shear failure [130]. Therefore, we assume the permeability deterioration factor to decrease exponentially with the cumulative fluid mass  $M_f$  flown at a location after failure:

$$D = \exp(-\chi M_f), \quad (2.16)$$

where  $\chi$  is a proportionality constant. For an ideal gas,  $M_f$  is given as

$$M_f = \int_{t_f}^t |\vec{q}| \rho_g dt = \int_{t_f}^t \rho_{sc} |\vec{q}| \frac{p}{p_{sc}} dt, \quad (2.17)$$

where  $\rho_{sc}$  is the gas density at standard conditions.

The shear dilation permeability-enhancement factor  $S$  has been reported in several studies as follows [128, 160]:

$$S = \exp(\gamma \Delta \tau), \quad (2.18)$$

where  $\gamma$  is the fracture dilation coefficient, and  $\Delta\tau = \tau - \tau_0$  is the difference between the current shear stress  $\tau$  (the radius of the largest Mohr's circle) and a reference value  $\tau_0$ . Combining 2.15, 2.17, and 2.18 we arrive at the following permeability model:

$$k_H = k_{Hf} \exp \left( \int_{t_f}^t -\kappa |\vec{q}| \frac{P}{P_{sc}} dt \right) \cdot \exp(\gamma \Delta\tau), \quad (2.19)$$

where  $\kappa$  is a permeability deterioration coefficient given by  $\kappa = \chi \rho_{sc}$ . One of the outcomes of this relation is that permeability is deteriorated the most in the near-wellbore region due to steeper pressure gradients. This equation calculates the variations of permeability at or beyond failure and make up for the limitations of a linear elastic formulation. A more rigorous analysis requires an elasto-plastic mechanical formulation.

## 2.3 Numerical solution method

### 2.3.1 Solution algorithm

Stress equilibrium and fluid flow equations are solved simultaneously on the current time step to obtain displacements and pore pressure. These data are then used to compute fluid density, the amount of sorbed gas, effective stresses, strains, porosity, and permeability. Fluid density, the amount of sorbed gas, porosity, and permeability for the next time step are obtained using an equation-of-state, Eq. 2.8, 2.9, and 2.13, respectively.

### 2.3.2 Finite Element implementation

The system of equations presented above is solved using the Finite Element Method by means of the FreeFem++ solver [84]. The Continuous Galerkin method is applied to Eq. (1, 9) to derive a Finite Element model. Assuming constant total vertical stress at every point of the domain (pseudo-3D conditions), we solve the problem in a 2D domain discretized with triangles. Piecewise quadratic and linear basis functions are used to approximate the displacements and pore pressure, respectively, to satisfy Ladyzhenskaya-Babuska-Brezzi conditions [190]. The equilibrium equation is solved using a full implicit scheme, and a semi-implicit scheme is used to solve the flow equation. The resulting symmetric linear system is solved with the Conjugate Gradient method.

## 2.4 Validation

### 2.4.1 Stresses in the vicinity of hydraulic fractures

The analytical expressions for stresses around a penny-shaped fracture were derived by Sneddon and Elliot [182]. Fig. 5.2a shows the comparison of stresses induced by a static fracture with half-length  $x_f = 20$  m pressurized with constant pressure  $p_0 = 1$  MPa along a line perpendicular to the fracture and obtained from both analytical and numerical solutions. The analytical solution for this case pre-

scribes the stresses as follows:

$$\begin{aligned}\sigma_{xx} &= \frac{2}{\pi} \int_0^\infty \Omega(\rho)(1 + \rho x)e^{-\rho x} \cos(\rho y) d\rho \\ \sigma_{yy} &= \frac{2}{\pi} \int_0^\infty \Omega(\rho)(1 - \rho x)e^{-\rho x} \cos(\rho y) d\rho \\ \Omega(\rho) &= -\frac{\pi}{2} p_0 x_f J_1(x_f \rho)\end{aligned}\quad (2.20)$$

where  $J_1$  is the Bessel function of the first order. Fig. 5.2b shows the validation of stresses calculated near the tip of the same fracture with the following analytical solution [198]:

$$\sigma_{yy}(x, 0) = p_0 \left[ \frac{x}{\sqrt{x^2 - x_f^2}} - 1 \right] \quad (2.21)$$

#### 2.4.2 Gas flow

We first perform the validation of gas gas flow model by comparison with the analytical solution [209]. It assumes a horizontal ideal gas flow in an infinite, uniform formation with initial pressure  $p_i$  into a wellbore with a constant mass flow rate  $Q_m$ . The analytical solution gives the following expression for the pressure at an arbitrary point and arbitrary time after the beginning of production/injection:

$$p^2(r, t) = p_i^2 - \frac{\mu Q_m}{2\pi k h \beta} \text{Ei}\left(-\frac{r^2}{4at}\right), \quad (2.22)$$

where  $h$  is the formation thickness,  $\text{Ei}$  is the exponential integral, and  $\beta$  is the gas compressibility factor given by

$$\beta = M_g / RT, \quad (2.23)$$

with  $M_g$  being the gas molecular weight,  $R$  the universal gas constant, and  $T$  being the constant formation temperature.

The comparison of the numerical and analytical solutions is illustrated on Fig. 5.2c, which shows radial pressure profiles at 1, 5, 10 and 20 hours, assuming a domain with the radius of 10 m and other parameters as follows:  $Q_m = 10^{-5} \text{ m}^3/\text{s}$ ,  $\mu = 1.84 \cdot 10^{-5} \text{ Pa-s}$ ,  $k = 10^{-15} \text{ m}^2$ ,  $\beta = 1.18 \cdot 10^{-5} \text{ kg/J}$ ,  $\phi = 0.3$ , and  $p_i = 1 \text{ atm}$ .

### 2.4.3 Stress path

In this section we show the advantages of the pseudo 3D model over the plane strain approach in the reservoir simulation coupled with geomechanics workflow. Linear isotropic poroelasticity predicts a decrease in total horizontal stress induced by pore pressure depletion under constant total vertical stress and no change of horizontal strain conditions [23]:

$$\frac{\Delta S_h}{\Delta p} = \frac{1 - 2\nu}{1 - \nu} b \quad (2.24)$$

Fig. 5.2d shows the comparison of the results produced by a plane strain poroelastic model, pseudo 3D model presented in this paper, and the Eq. 2.24 using the values of Biot coefficient  $b = 0.8$  and Poisson ratio  $\nu = 0.339$ . As it is shown in Fig. 5.2d, the plane strain model yields a significantly larger decrease in total horizontal stresses induced by pore pressure depletion.

## 2.5 Case studies

### 2.5.1 San Juan coal basin

The San Juan basin is a coalbed methane (CBM) reservoir in North America and spans through sections of Colorado and New Mexico [140]. This bituminous

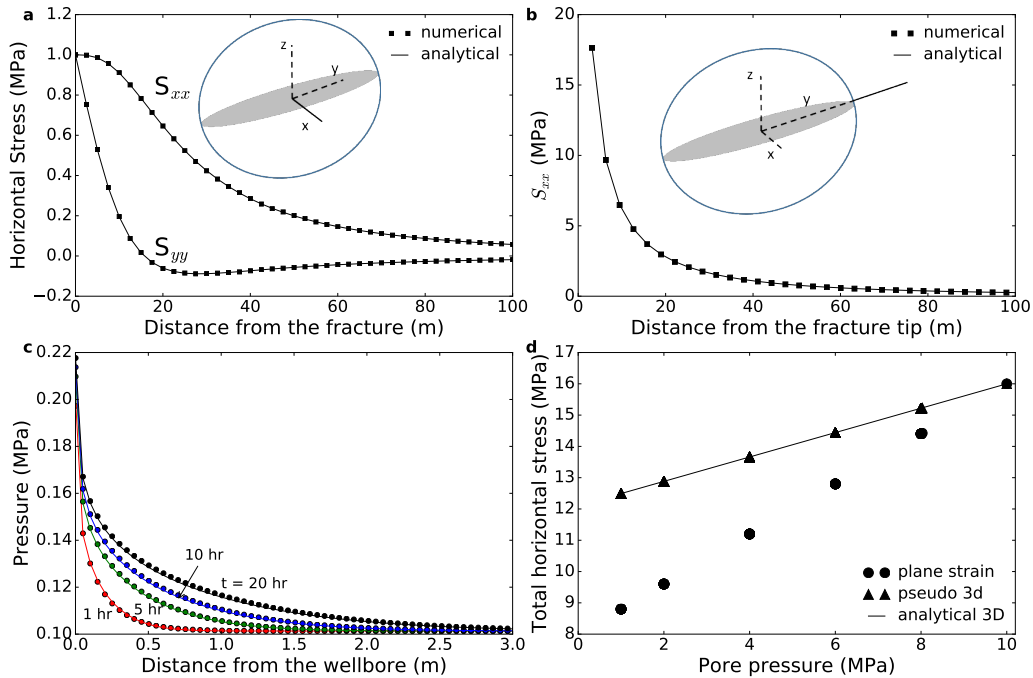


Figure 2.2: Validation of the numerical model. (a) Stresses profile along x-axis starting from the center of the fracture. (b) Stress profile along y-axis starting from the fracture tip. (c) Pressure profile as a function of distance from the wellbore. (d) Total horizontal stress path predicted by plane strain and pseudo 3D linear poroelasticity (used in the study) models.

coal is cleated and therefore has predominantly vertically-oriented natural fractures [33, 130]. Field data from the Fruitland coals fairway have been chosen for analysis, since the gas flow behavior manifests strong flow-mechanical-coupling [130]. An example of gas production is presented in Fig. 2.3a. Reported field permeability was obtained from bottom-hole pressure using the equation of pseudo steady-state radial flow with an appropriate skin factor and is shown in Fig. 2.3b. According to these data, reservoir permeability rapidly increases during the first 1100 days of production, followed by an almost instantaneous permeability drop and a slow and steady growth afterwards. The study reported massive production of fines that indicated shear failure and started on the day of permeability drop [130]. Such behavior of reservoir permeability cannot be simulated using conventional reservoir simulators or even the mechanically-coupled numerical models that do not take into account desorption-induced strains and shear failure. We present the results of history matching performed with two variations of the model presented in Section 2.2. The first simulation accounts for permeability changes due to stress relaxation, similar to most CBM models, but does not include other effects induced by shear failure. The second model includes effects induced by shear failure, such as fracture dilation and fines clogging. The simulated section of the fairway extends by an equivalent coal seam volume of 1200 m in length, 1200 m in width, and 33.5 m in height. The reservoir is set with a 100-meter-long hydraulic fracture at the center [132]. San Juan coal basin has a normal-faulting stress regime, the average depth of 840 m, and the average total minimum horizontal stress of 16 MPa that was obtained from instantaneous shut-in pressure data from 155 wells [36, 148]. As-

suming the overburden gradient 22.6 kPa/m, we calculated the total vertical stress of 19 MPa. The rest of the simulation parameters were collected from the literature, assumed, or best-fitted and are listed in Table 2.1. Due to the lack of data referring to well completion details and well schedule, among others, we present an illustrative history matching using the aforementioned model. Section 2.6 evaluates the sensitivity of some of these parameters.

### 2.5.1.1 Stress-dependent permeability: fracture compressibility only

Here we present the results of history matching of the field production data from Fruitland coal using only fracture compressibility (Eq. 2.13). In this case we do not account for shear failure, fracture dilation, and fines migration, so that Eq. 2.13 is applied throughout the entire production period. As a consequence of this approach, reservoir permeability steadily increases due to depletion and desorption-induced stress relaxation (Fig. 2.3b). The bottom-hole pressure values have a significant impact on the gas flow rates at early times: a large drawdown increases effective stresses near the fracture resulting in a decrease in permeability due to fracture compressibility. The simplified bottom-hole pressure schedule that best fits gas production data is shown in Fig. 2.3c.

Fig. 2.3a shows the results of history matching of the gas production history using the effects on permeability of fracture compressibility only. The model is capable of capturing the main trend, although it tends to underestimate early production rates ( $t < 1500$  days) and overestimate late production rates ( $t > 2000$  days). These trends are also observable in Fig. 2.3b that compares field-measured gas

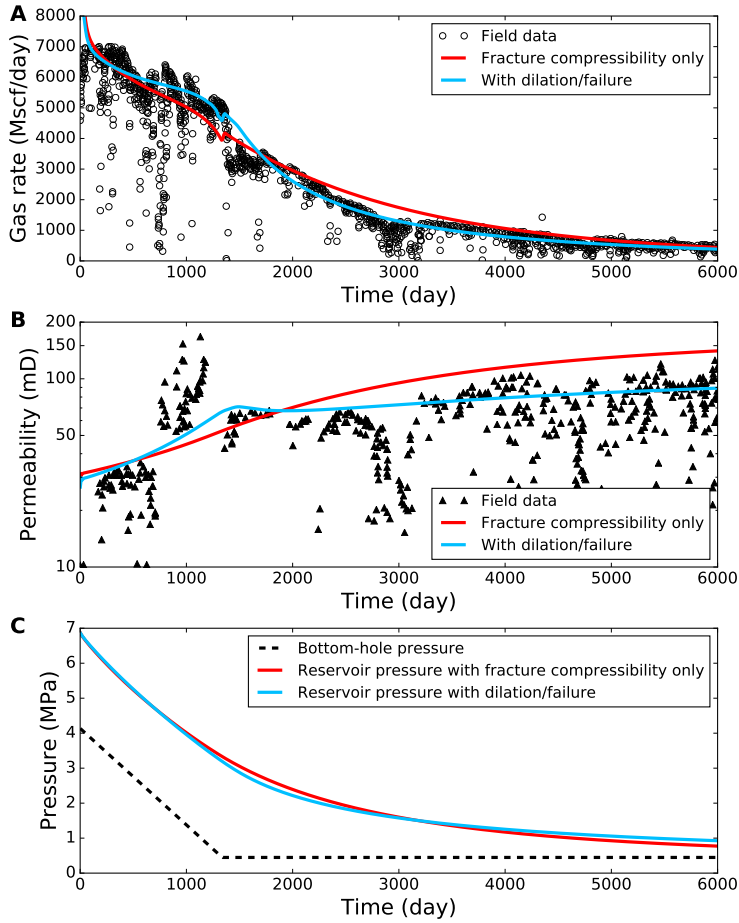


Figure 2.3: History matching of field data from a CBM well in Fruitland coal [130] using fracture compressibility only (no dilation/failure) and shear failure with fracture dilation and fines migration cases. (a) Production rates. (b) Average reservoir permeability evolution. (c) Bottom-hole and average reservoir pressure as functions of time.

Table 2.1: Simulation parameters and initial conditions. (\*) Assumed, (\*\*) Best fit.

Property	San Juan coal	Barnett shale
Fracture half-length $x_f$ , m	50 (*)	47.2 [214]
Young's Modulus $E$ , GPa	3.2 [138]	24.0 [214]
Poisson's ratio $\nu$	0.34 [138]	0.30 (*)
Biot coefficient $b$	0.8 (*)	0.8 (*)
Langmuir pressure $P_L$ , MPa	6.11 [174]	4.48 [214]
Langmuir volume $V_L$ , $m^3/kg$	0.0096 [138]	0.0027 [214]
Maximum swelling strain $\varepsilon_L$	0.0127 [175]	0.0012 [86]
Rock matrix density $\rho_m$ , g/cm <sup>3</sup>	1.40 [55]	2.58 [214]
Total porosity $\phi$ , %	10 (*)	6 [214]
Reference permeability $k_{H0}$ , mD	80 (**)	$10^{-4}$ (**)
Residual permeability $k_{Hr}$ , mD	1 (*)	$10^{-5}$ (*)
Reference effective horizontal mean stress $\sigma_H$ , MPa	7 (**)	7 (**)
Reference effective vertical mean stress $\sigma_V$ , MPa	7 (**)	7 (**)
Horizontal fracture compressibility $\alpha_H$ , MPa <sup>-1</sup>	0.25 (**)	0.080 (**)
Vertical fracture compressibility $\alpha_V$ , MPa <sup>-1</sup>	0.05 (**)	0.016 (**)
Initial minimum total horizontal stress $S_{hmin}$ , MPa	16 [148]	26.8 [214]
Initial maximum total horizontal stress $S_{hmax}$ , MPa	17 (*)	29.0 (*)
Total vertical horizontal stress $S_V$ , MPa	19 (*)	37.7 [214]
Initial reservoir pressure, MPa	6.9 [130]	20.3 [214]

permeability and average permeability from simulations. Non-uniform stresses

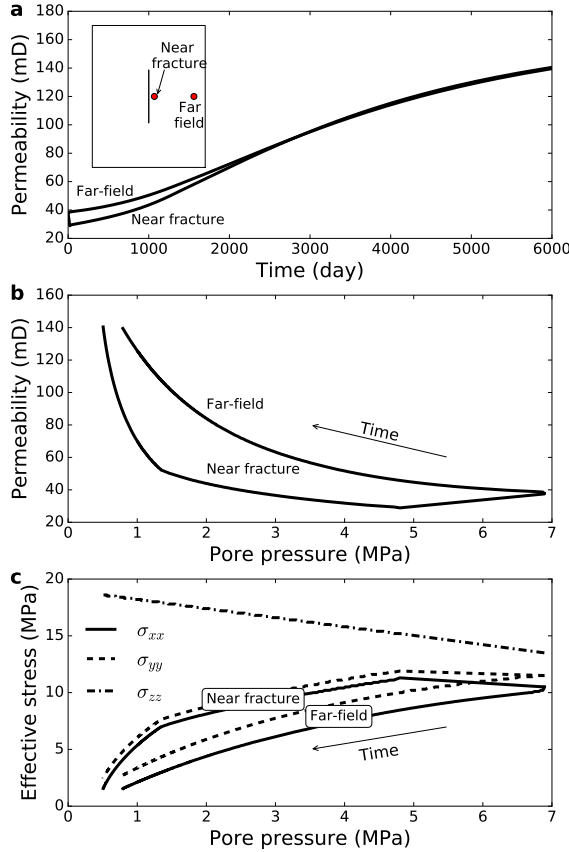


Figure 2.4: Near-fracture and far-field evolution of coal-seam permeability and stresses considering fracture compressibility only. (a) Permeability as a function of time near fracture and far from the fracture. (b) Permeability as a function of pore pressure near fracture and far from the fracture. (c) Reservoir Biot effective stresses as a function of pore pressure near fracture and far from the fracture.

induced the propped hydraulic fracture and pore pressure drawdown results in a non-uniform distribution of permeability in the reservoir. Far field (450 m from the fracture) and near-fracture (20 m from the fracture) permeability profiles as functions of time are shown in Fig. 2.4a. Near-fracture permeability decreases

at the beginning of production because of high compressive stresses in the vicinity of the hydraulic fracture. At later times, the effect of pore-pressure depletion and desorption-induced shrinkage hinder stresses induced by the propped fracture so that near-fracture and far-field permeabilities converge to the same values. The effect of bottom-hole pressure reduction can be easily seen when plotting permeabilities as functions of pore pressure (Fig. 2.4b). Permeability in the fracture proximity grows slower than that in the far-field (pore pressure range  $1.3 \text{ MPa} < p < 4.8 \text{ MPa}$ ) during the period of lowering the bottom-hole pressure. During that period desorption-induced stresses are not developed yet, and the stress state in the reservoir is controlled by pressure depletion. After the bottom-hole pressure has been lowered, near-fracture permeability starts growing more rapidly approaching permeability in the far-field zone.

The near-fracture and far-field stress paths are shown in Fig. 2.4c. Biot vertical effective stress  $\sigma_{zz}$  exhibits a linear growth as predicted by linear poroelasticity, and the curves coincide near the hydraulic fracture and in the far-field, because of the assumption of constant total vertical stress. Effective horizontal stresses, however, exhibit a more complicated behavior. The initial deviation ( $5 \text{ MPa} < p < 7 \text{ MPa}$ ) of near-fracture and far-field stress paths is caused by the presence of the hydraulic fracture that results in higher compressive horizontal stresses perpendicular to the fracture. Subsequent reduction of horizontal effective stresses between pore pressure range  $1.2-5 \text{ MPa}$  is similar in the far-field and in the proximity of the hydraulic fracture. The non-linear shape of the stress-path curve is due to the non-linearity of the sorption-strain isotherm. A kink in the near-fracture stress-path

curve at pore pressure approximately equal to 1.2 MPa is caused by a change in the wellbore schedule, when the bottom-hole pressure reaches the minimum value of 0.45 MPa. This effect is not observed in the far-field because pore pressure in the far-field does not readily react on the changes in the bottom-hole pressure.

The case including fracture compressibility only does not allow a fair capture of the complicated behavior of the production gas rate curves and tends to overestimate permeability at the end of production period and underestimate it at the moment of shear failure. Due to that reason we present matching field production data using another simulation case that includes shear failure and its consequences, such as natural and induced fracture dilation and permeability deterioration due to fines migration and clogging.

### **2.5.1.2 Stress-dependent permeability: fracture compressibility, dilation and shear failure**

In this section we present history matching of the same CBM-field data using a model that accounts for fracture dilation and shear failure. As discussed in Section 2.2.3, reservoir permeability is calculated with Eq. 2.13 before shear failure occurs, whereas Eq. 2.19 is used to compute permeability after it occurs. The results of history matching are shown in Fig. 2.3a. The original paper reported sporadic increases of permeability (up to  $\approx 2000$  mD) followed by a pressure drop at approximately 1500 days associated with shear failure and posterior fines production and clogging [130]. The simulation parameters related to fracture dilation and shear failure used in the simulation are shown in Table 2.2. The model with shear

failure reproduces the behavior of the field data better than the model with fracture compressibility only (Fig. 2.3a). The earlier part of the curve (before  $\approx 1500$  days of production) is reproduced with a value of fracture compressibility  $\alpha_H = 0.3 \text{ MPa}^{-1}$ , higher than the one with fracture compressibility only and yielding a closer fit to the field permeability measurements as shown in Fig. 2.3b. Later-time production (after  $\approx 1500$  days) is governed by two competitive processes: fracture permeability enhancement due to fracture dilation and permeability deterioration due to fines migration and clogging. The best-fitting parameters of fracture dilation coefficient are  $\gamma = 0.45 \text{ MPa}^{-1}$  and  $\kappa = 10^{-4} \text{ s/m}$ . This combination of parameters results in a slight decrease of average reservoir permeability after failure with a later steady increase as shown in Fig. 2.3b. The simulation data does not match the field data exactly immediately after the shear failure due to a simplification: Moore's study reported several wellbore clean-up interventions, which we do not attempt to simulate here. The effect of fines migration/clogging and permeability deterioration is discussed in more detail in Section 2.6. Average reservoir permeability per se, as it is shown in Fig. 2.3b, is insufficient to understand the reservoir permeability be-

Table 2.2: Simulation parameters used in history matching of the data from San Juan coal using the model with shear failure. (\*) Best fit.

Property	Value
Fracture dilation coefficient $\gamma$ , $\text{MPa}^{-1}$ (*)	0.45
Fracture compressibility $\alpha$ , $\text{MPa}^{-1}$ (*)	0.3
Reference permeability $k_{H0}$ , $\text{mD}$ (*)	80
Cohesive strength $C$ , $\text{MPa}$ (*)	0.35
Friction angle, $^\circ$ [219]	27
Permeability deterioration coefficient $\kappa$ , $\text{s/m}$ (*)	$10^{-4}$

havior. In contrast to the average value, Fig. 2.5a shows the evolution of far-field and near-fracture permeability values with depletion. The permeability trends in the far-field (450 m from the hydraulic fracture) and near-fracture (20 m from the hydraulic fracture) zones manifest opposite trends after shear failure occurs. In the near-fracture zone fines migration and clogging dominates over fracture dilation and causes a decrease in permeability (high amount of flow). Conversely, permeability in the far-field increase due to dominance of fracture dilation (lower flow rates).

Another noticeable difference between far-field and near-fracture permeability can be seen when plotting permeabilities versus pore pressure (Fig. 2.5b). The initial deviation of the curves in the pore-pressure region of 5-7 MPa is due to the imposed change of bottom-hole pressure. While sorption strains are undeveloped, stress-shadow effects induced by a propped fracture reduce permeability near it. Until the failure point the far-field and near-fracture permeabilities exhibit the same increasing trends caused by desorption-induced stress relaxation, but a change occurs at failure (different values of pore pressure  $p=1.2$  MPa for the near-fracture zone and  $p=2.9$  MPa for the far-field zone). Because of assumed linear elasticity, the stresses are unaffected by surpassing shear failure envelope and are similar to these in Fig. 2.5c.

### 2.5.2 Barnett shale

The Barnett shale formation is an organic-rich shale gas reservoir in north-east Texas, USA. This formation has extremely low permeability and commercial

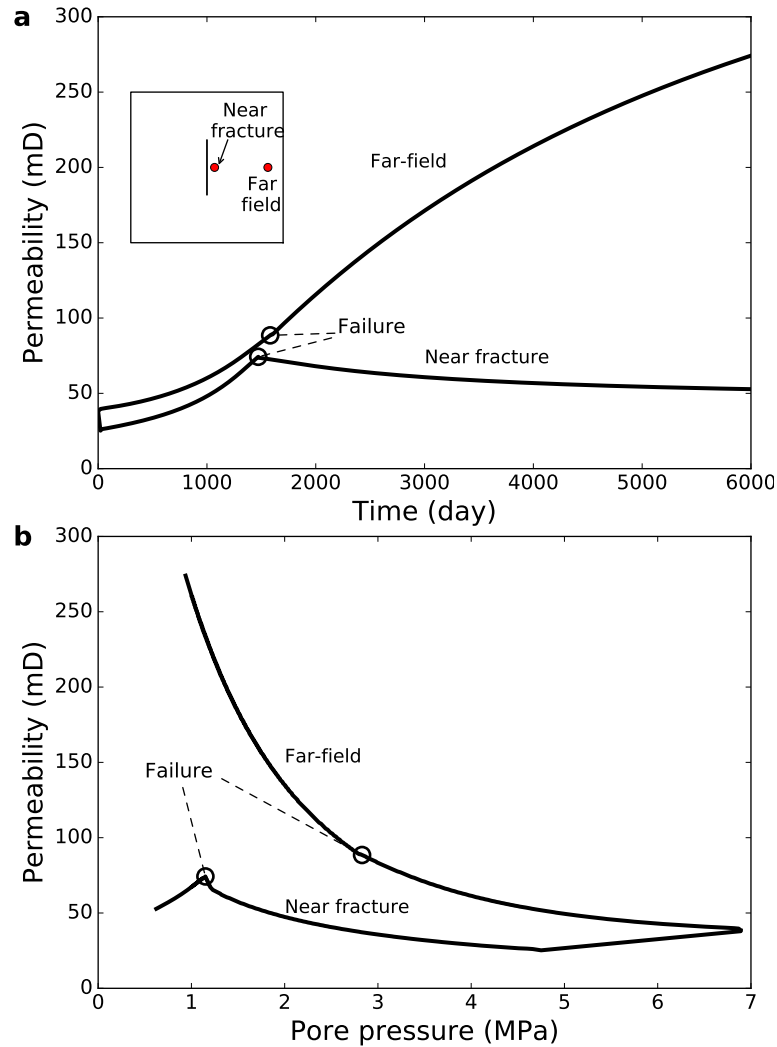


Figure 2.5: Near-fracture and far-field evolution of permeability in the case with shear failure and fracture dilation. (a) Temporary permeability profiles near fracture and far from the fracture. (b) Permeability as a function of pore pressure near fracture and far from the fracture.

production requires hydraulic fracturing [59]. We performed history matching of field data [4, 214] from the Barnett shale as an example of a formation that can develop small gas-sorption strains. The simulation domain size is  $914.1 \times 457.2 \times 91.4$  m<sup>3</sup> ( $3000 \times 1500 \times 300$  ft<sup>3</sup>) comprising 28 hydraulic fractures with half-length of 47.2 m (155 ft), height of 91.4 m (300 ft), and spaced every 30.5 m (100 ft). In shales swelling strains induced by gas sorption have been measured directly only in samples from Niutitang shale [31]. In the case of the Barnett shale we use values from extrapolations suggested by Heller and Zoback [86]. Other parameters used in simulation are listed in Table 2.1. The fracture compressibility parameter of hydraulically-fractured shales is not straightforward to determine. This parameter could depend on whether fractures are propped or not and depends highly on the rock lithology [125]. We use a best-fitting average value  $\alpha = 0.1$  MPa<sup>-1</sup> everywhere in the domain. Other parameters were assumed, best-fitted, or taken from the literature and are listed in Table 2.1. The bottom-hole pressure is kept at a constant value  $P_w = 4.14$  MPa [214]. History matching of the production data from the Barnett shale is shown in Fig. 2.6. Two cases were computed to estimate the impact of sorption-induced stresses: (1) with zero swelling stress and stress-dependent permeability and (2) with non-zero sorption stress and stress-dependent permeability. Ignoring stress-dependent permeability results in a poor fitting (not shown in figure). Fig. 2.6a shows gas flow rate and cumulative production as functions of time. Flow rate in case (1) is slightly lower than in case (2) causing the cumulative difference in total production of 12.5% after 1600 days of production. Gas rates are higher in case (2) because expansive desorption-induced strains cause less compres-

sive effective stresses and, therefore, higher permeability. Near-fracture (50 ft from the fracture) and far-field (at  $0.5x_f$  from the tip of the hydraulic fracture). are shown in Fig. 2.6b. Far-field permeability values are higher than those in the near-fracture region because the hydraulic fracture imposes additional compressive stresses, thus lowering permeability. The effect of desorption-induced strains is clearly seen in Fig. 2.6b: permeabilities in cases with zero and non-zero sorption strains are the same initially initially but deviate with depletion with higher values in the case (2). Change of stresses induced by gas desorption in this simulation are small compared to the effective stresses due to overburden, as shown in Fig. 2.7, and have a minor impact on permeability. However, the impact of sorption strains on horizontal effective stress  $\sigma_{xx}$  is rather significant ( $\approx 4$  MPa at the end of depletion) and would be enough to change local stress orientation and alter fracture propagation direction from infill wells. Desorption-induced strains do not significantly alter horizontal effective stress  $\sigma_{yy}$ , which is controlled by the Poisson effect in the vicinity of the hydraulic fracture. Vertical effective stress  $\sigma_{zz}$  takes the same values with both zero and non-zero effective stresses due to the assumption of constant total vertical stress in the entire domain.

## 2.6 Discussion

### 2.6.1 Parametric analysis of the model with fracture compressibility only

The simulation parameters used for history matching of the field data from Fruitland coal (Fig. 2.3a) are used as a base case scenario with  $\alpha_H = 0.25 \text{ MPa}^{-1}$ ,  $k_{H0} = 80 \text{ mD}$ , and  $x_f = 50 \text{ m}$ . The bottom-hole pressure schedule is a linear de-

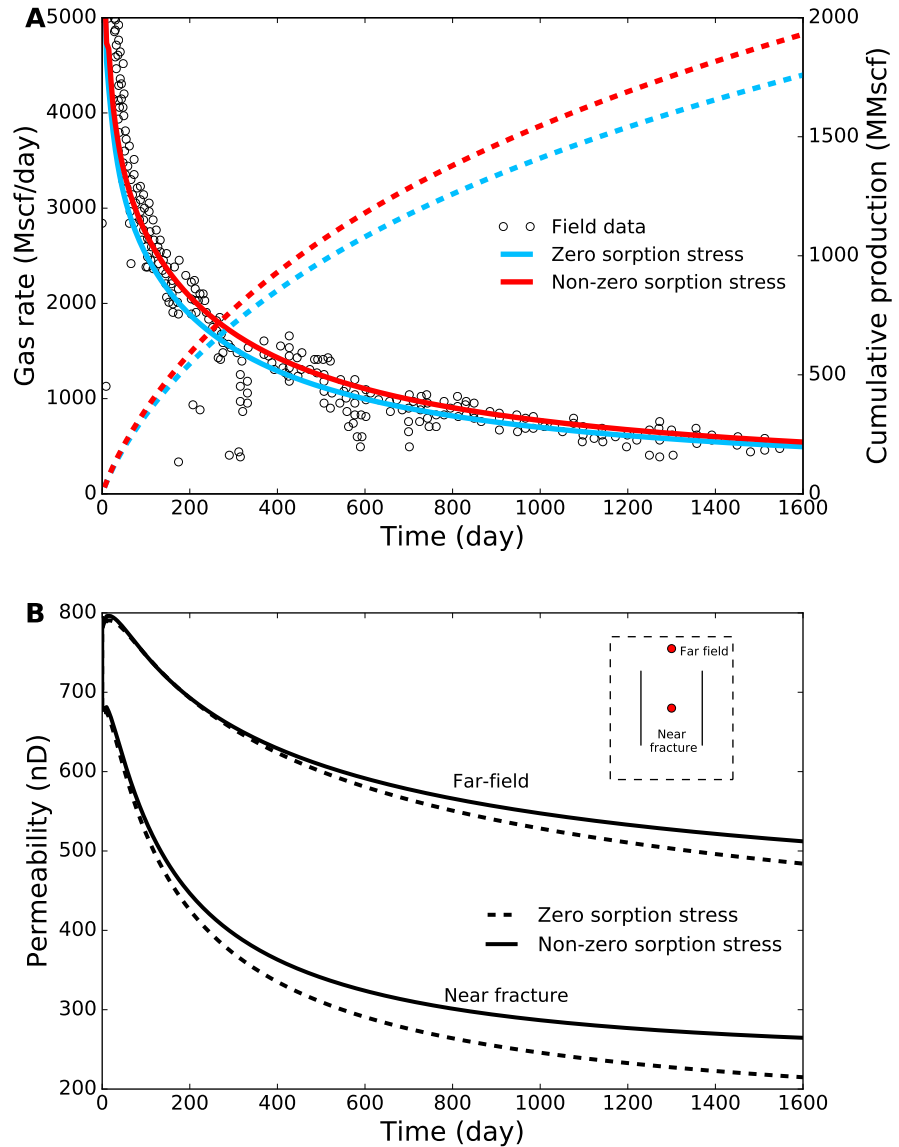


Figure 2.6: History matching of the field data from the Barnett shale. (a) Comparison of production gas rates and cumulative production for the cases with zero and non-zero sorption stress. (b) Near-fracture and far-field permeabilities as a function of time for the cases with zero and non-zero sorption strains.

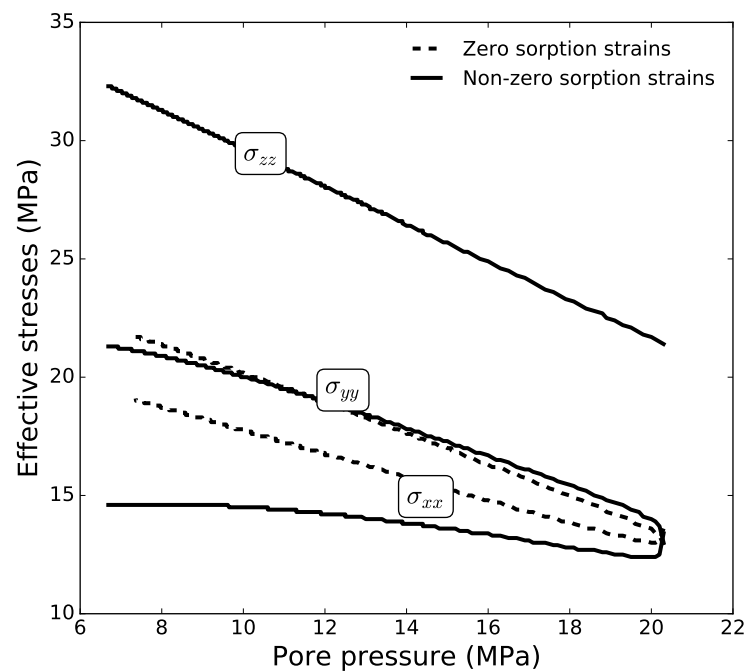


Figure 2.7: Effective stresses as a function of time for the cases with zero and non-zero desorption-induced strains in the vicinity of the hydraulic fracture. Swelling strains lower compressive horizontal effective stress  $\sigma_{xx}$ .

crease from  $p_w=3.45$  MPa to  $p_w=0.59$  MPa with the rate  $\partial p_w/\partial t=2760$  Pa/day. The results of the analysis varying  $\alpha_H$  ( $\alpha_V=\alpha_H/5$ ),  $k_{H0}$ , and  $x_f$ , and the wellbore schedule are summarized in Fig. 2.8. Fig. 2.8a shows the sensitivity analysis to fracture compressibility  $\alpha_H$ . Low values of  $\alpha_H$  result in high initial production rates and low production rates after reaching pseudo-steady-state flow regime. In contrast, high values of fracture compressibility  $\alpha_h$  cause low initial production rates because high effective compressive stresses near the draining fracture and undeveloped sorption strains result in a significant decrease in permeability. Late production rates are higher for high values of  $\alpha_H$  than for low  $\alpha_H$  because desorption-induced stress relaxation causes higher increases of permeability. According to this result, reservoirs such as coal with high fracture compressibility and significant desorption-induced shrinkage exhibit slow decreases in production rates. On the other hand, when sorption-induced strains are small, such as in shales, higher fracture compressibility would result in faster fracture closure and steeper production decline rates.

As expected, high reference (and therefore initial) horizontal permeability  $k_{H0}$  results in higher production rates and faster depletion than low values of reference permeability (Fig. 2.8b). As shown in Fig. 2.8b, relative increase in permeability does not depend on  $k_{H0}$ , whereas the difference in magnitude between initial and late-time reservoir permeabilities is higher for the higher  $k_{H0}$ .

Hydraulic fracture length also affects permeability evolution. As shown in Fig. 2.8c, short fractures cause lower production rates than long fracture and result in slower depletion and lower increases in permeability.

Fig. 2.8d summarizes the effect of bottom-hole pressure schedule. Fast

decreases in bottom-hole pressure result in high initial gas production rates but may show unusual rapid transient declines due to large increases of effective stress near the fracture and adversely affect permeability. The opposite is observed when slow bottom-hole pressure reduction is implemented.

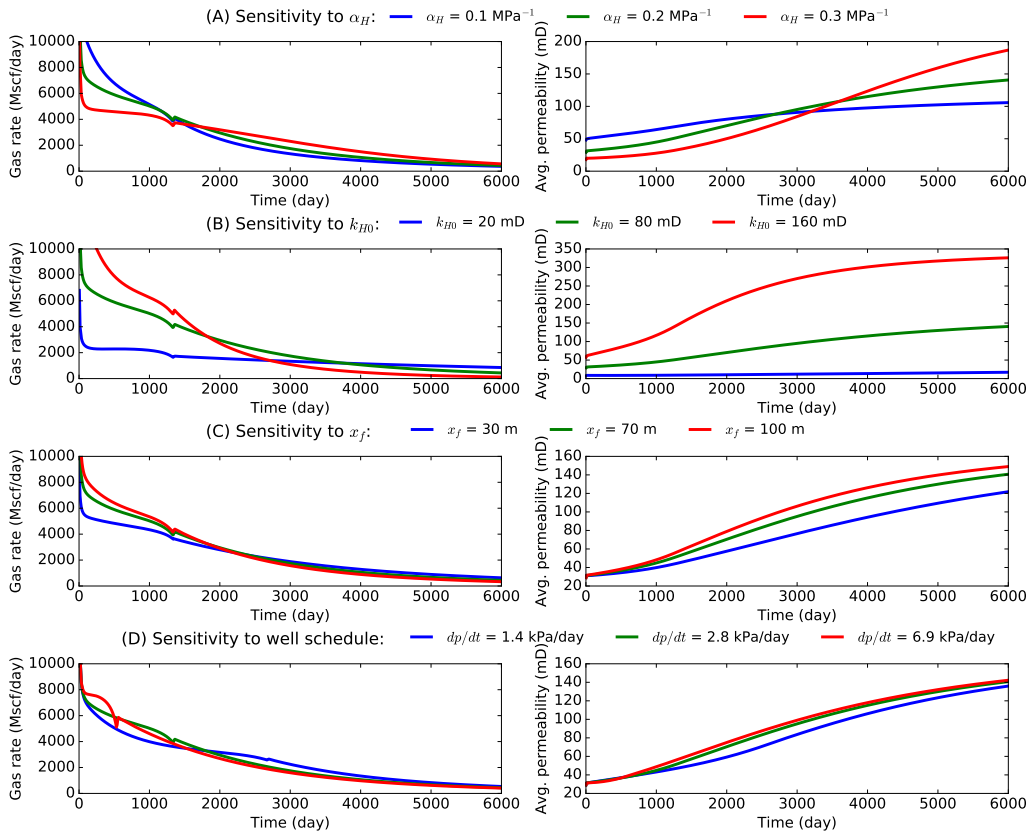


Figure 2.8: Sensitivity analysis of stress-dependent permeability model considering only fracture compressibility. Base case:  $\alpha_H = 0.2 \text{ MPa}^{-1}$ ,  $k_{H0} = 80 \text{ mD}$ ,  $x_f = 70 \text{ m}$ ,  $\partial p_w / \partial t = 2.76 \text{ kPa/day}$ . Parameters from San Juan coal basin. (a) Sensitivity study to fracture compressibility  $\alpha_H$ . (b) Sensitivity study to reference permeability  $k_{H0}$ . (c) Sensitivity study to fracture half-length  $x_f$ . (d) Sensitivity study to wellbore schedule.

### 2.6.2 Parametric analysis of the model with shear failure

In this section we present parametric analysis of the parameters that affect gas production in a coal seam reservoir after shear failure occurs (Fig. 2.9). The base-case scenario parameters are fracture dilation coefficient  $\gamma = 0.45 \text{ MPa}^{-1}$ , permeability deterioration coefficient  $\kappa = 10^{-4} \text{ s/m}$ , and the cohesive strength of the rock  $C = 1.38 \text{ MPa}$ . Internal friction angle is kept constant for all simulations  $\varphi = 27^\circ$ . Note that the variation of the production and permeability curves starts after the point of shear failure since the parameters varied in this subsection do not control pre-failure reservoir permeability. The sensitivity analysis to fracture dilation coefficient  $\gamma$  is shown in Fig. 2.9a. High values of fracture dilation  $\gamma$  results in higher values of permeability after failure than small  $\gamma$ . The dominance of the effect of fracture dilation on permeability over fines migration and pore clogging is clearly seen in the case of  $\gamma = 0.55 \text{ MPa}^{-1}$ , whereas  $\gamma = 0.1 \text{ MPa}^{-1}$  indicates the dominance of permeability deterioration due to fines migration.

The sensitivity analysis of the effect of permeability deterioration coefficient  $\kappa$  is illustrated in Fig. 2.9b. When  $\kappa = 0$ , the average permeability monotonically increases similar to the case of fracture compressibility only. In contrast, when  $\kappa = 10^{-3} \text{ s/m}$ , average permeability starts rapidly decreasing after the shear failure.

Various values of rock cohesive strength delay or accelerate the advent of shear failure, as shown in Fig. 2.9c. Lower values of cohesive strength result in earlier times of shear failure, and strong rocks with high cohesive strength exhibit shear failure later.

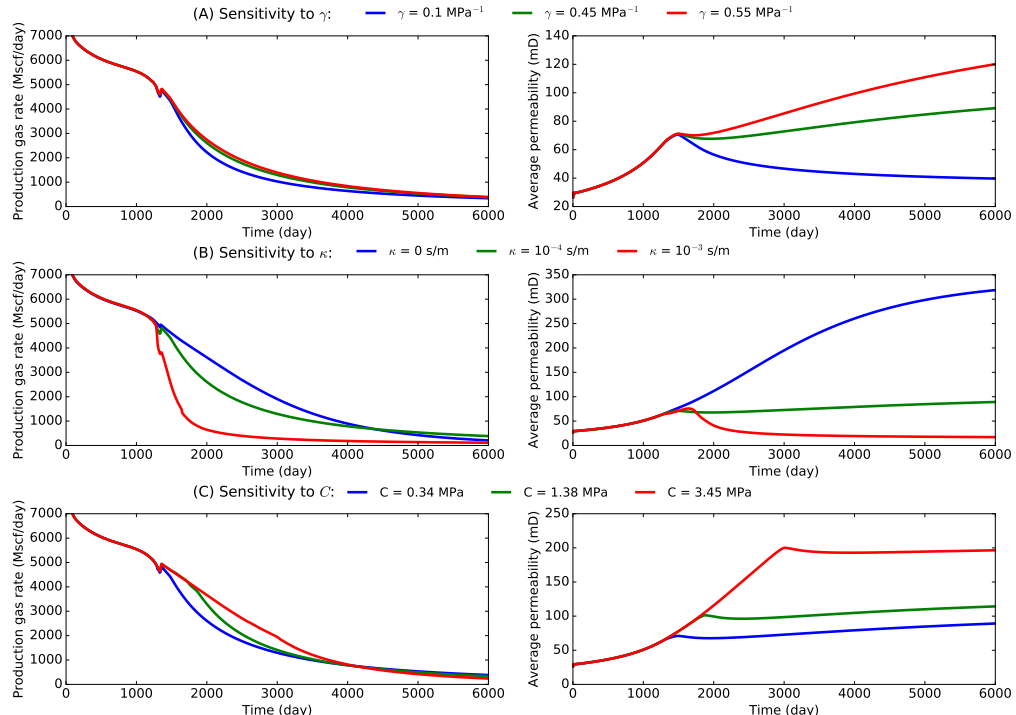


Figure 2.9: Sensitivity analysis of stress-dependent permeability model considering shear failure. Parameters from San Juan coal basin. Base case:  $\gamma = 0.45 \text{ MPa}^{-1}$ ,  $\kappa = 10^{-4} \text{ s/m}$ ,  $C = 1.38 \text{ MPa}$ . (a) Sensitivity study to fracture dilation coefficient  $\gamma$  (b) Sensitivity study to permeability degradation parameter  $\kappa$  (c) Sensitivity study to cohesive strength  $C$ .

### 2.6.3 Gas sorption stresses in shales

Sorption-induced stresses, which lead to significant changes in the permeability of coal reservoirs, may also have a non-negligible impact in shales. The magnitude of these changes depends on the sorption capacity of the rock as well as its clay content, elastic properties and fracture compressibility. Fig. 2.10a shows the amount of sorbed gas (at standard conditions) per unit volume of rock matrix for San Juan coal and Barnett and Devonian shales [86, 207, 31]. Coals, in general, have higher sorption capacity than shales and exhibit higher gas sorption strains. Sorption-induced strains measured in San Juan coal and Niutitang and Devonian organic-rich shale are shown in Fig. 2.10b [207, 31]. Sorption strains in Niutitang and Devonian shales (and presumably in the Barnett shale) are an order smaller than those in San Juan coal likely because of larger elastic modulus of the shale and the patchy distribution of organic matter. Besides swelling of organic macromolecules, other evidence suggests that the intercalation of  $\text{CH}_4$  and  $\text{CO}_2$  molecules between clay platelets can induce strains and stresses [43, 86, 25]. Despite small sorption-induced strains  $\varepsilon_L$ , sorption could have a noticeable impact on in-situ stresses because sorption stresses are directly proportional to the bulk elastic moduli of rocks  $K$ . Hence, given a change of pore pressure  $\Delta p$ , the contribution of sorption-induced stresses to the change of stress would be the same as long as the product  $K \cdot \varepsilon_L$  remains constant (Eq. 2.6). Fig. 2.10c shows the product  $K \cdot \varepsilon_L$  as a function of  $\varepsilon_L$  for the shales and coals discussed before. The parameter  $K \cdot \varepsilon_L$  is a proportionality factor of sorption-induced stress as a function of pressure, and, according to Fig. 2.10c, it is of similar magnitudes in coals and shales. Differences may arise in coals

and shales, however, due to the range of pressures during depletion with respect to the Langmuir pressure  $P_L$ . Fig. 2.10a highlights this difference in changes of gas sorption amount and expected strains in unjacketed conditions.

The variations of permeability caused by reservoir depletion in turn depend on the fracture compressibility  $\alpha$ . This parameter can be directly measured at the core scale but is considerably difficult to measure at the reservoir scale. Reservoir-scale fracture compressibility is a factor that depends on many parameters, such as the fracture spacing, width, and asperity; elastic, and plastic properties of the rock [128]. Moreover, fracture compressibility can be much higher in propped fractures than in un-propped fractures and can be substantially enhanced when proppant embedment occurs [49]. History matching in this study implies that fracture compressibility parameters is about 10 times lower in shale reservoirs than in coal. However, comprehensive studies on fracture compressibility are needed to better understand the sensitivity of natural and induced fracture permeability to stresses in organic-rich shales.

## 2.7 Conclusions

- The presented fully-coupled poromechanical model is capable of accounting for sorption stresses changes in permeability in stress-sensitive dry gas reservoirs and allows for simulation of non-trivial production rate evolution as a function of time.
- We successfully simulated evolution of permeability assuming a simplified

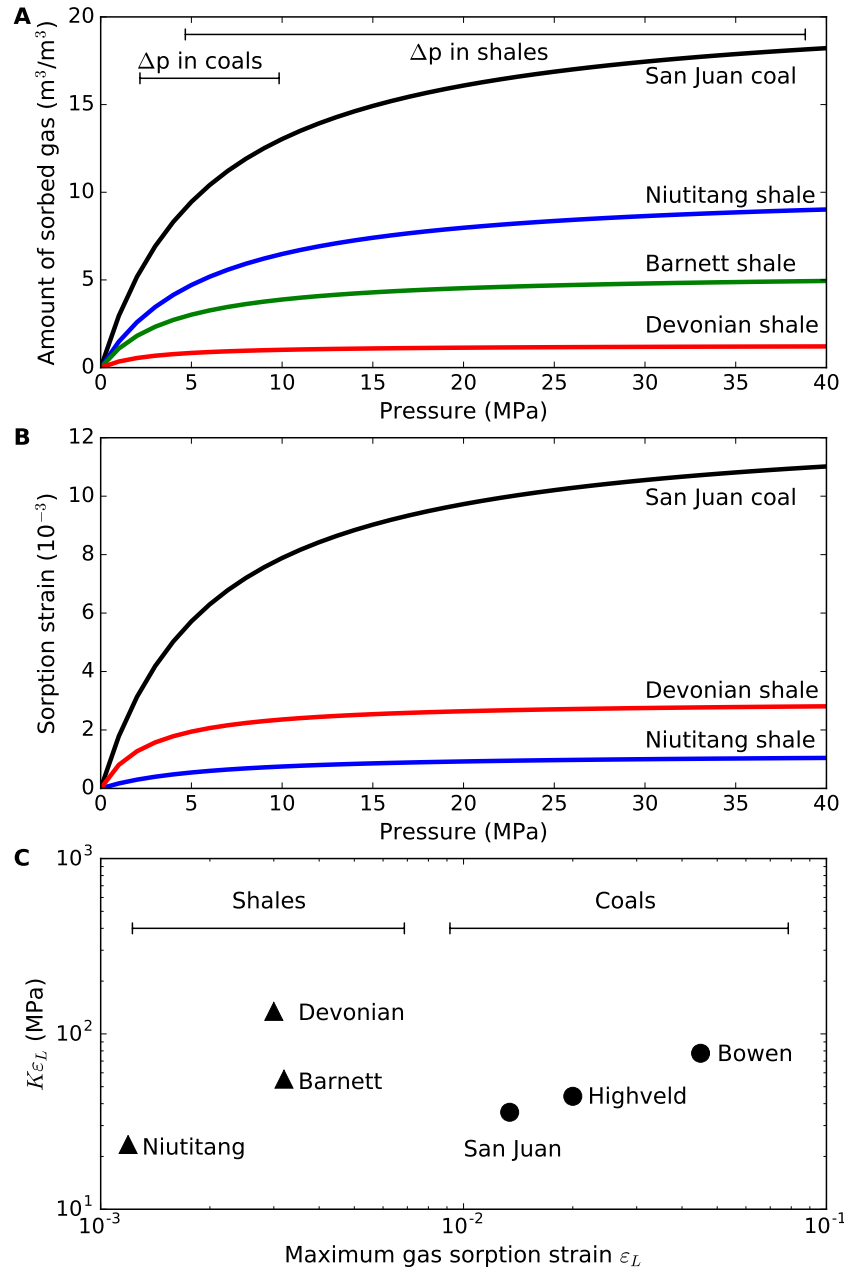


Figure 2.10: Sorption isotherms for San Juan coal and Devonian and Barnett shales. (a) Volume of adsorbed methane (at standard conditions) per unit volume of rock matrix as a function of pore pressure. (b) Swelling sorption-induced strains in San Juan coal and Niutitang and Barnett shales as functions of pore pressure. (c) Product of the rock's bulk modulus and the maximum swelling strain  $K \cdot \varepsilon_L$  as a function of the maximum swelling strain  $\varepsilon_L$  for various shales and coals.

model of permeability deterioration and fines production and showed that permeability models taking into account only fracture compressibility tend to overestimate permeability at late production times.

- Permeability alterations are not uniform throughout the reservoir: they vary from the draining fracture to the far-field zones due to stress heterogeneity, stress shadows from propped fractures, and the enhancement of clogging near draining sinks.
- Shear failure related to gas production in San Juan reservoir may occur at a range of pore pressure values (1-3 MPa) depending on local stresses and the distance from draining fractures.
- Numerical simulation confirmed that desorption-induced strains in shales may induce changes of horizontal stresses of several MPa. These changes of stress may have a minor effect on permeability but can significantly affect horizontal stress anisotropy and should be considered while planning refracturing.
- Reservoir permeability is highly sensitive to the rock mass Young's modulus, maximum swelling strain of the rock, and the formation fracture compressibility.
- Our study demonstrates that well-known changes in permeability in coals could be present in shales as well at a lower level.
- Based on these findings, we recommend that modern reservoir simulators use a fluid flow model coupled with geomechanics to model fractured reservoirs

where stresses change significantly during production.

# **Chapter 3**

## **Geomechanical implications of dissolution of mineralized natural fractures in shale formations<sup>1</sup>**

### **3.1 Introduction**

Hydrocarbon-bearing shale formations can extend over large areas, and contain vast amounts of oil and gas. However, they are distinguished by extremely low permeability and low recovery factors [164]. Not all shale plays are equally productive [144]. Sweetspots, places exhibiting high production rates, usually contain a fair amount of natural fractures, among other features [64]. Hydraulic fracturing, the primary stimulation technology in shales, has been known to significantly increase production rates. In shales, in particular, hydraulic fracturing provides access to the systems of natural fractures and substantially increases the drainage area connected to the wellbore, commonly referred to as stimulated reservoir volume [58]. Furthermore, natural fracture networks can promote hydraulic fracture “branching”, enhance their complexity, and allow hydrocarbons in the shale matrix to reach the wellbore more easily through both propped and un-propped fractures [58, 185, 108, 172, 52]. Production from hydraulically fractured shale reservoirs,

---

<sup>1</sup> Igor Shovkun and D. Nicolas Espinoza. Geomechanical implications of dissolution of mineralized natural fractures in shale formations. *Journal of Petroleum Science and Engineering*, 160:555564, 2018. All authors contributed equally.

however, suffers from rapid production declines [142]. One of the reasons of rapid decline is the closure of natural fractures caused by the depletion-induced increase in effective stresses [40]. Therefore, both extending fracture network and reducing the closure of natural fractures are desirable to increase and maintain reservoir fracture permeability.

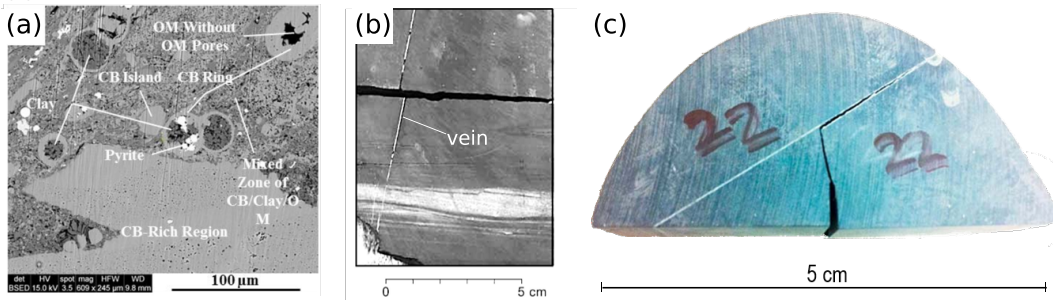


Figure 3.1: Different modes of calcite occurrence in shales. (a) Carbonates (CB) in the matrix (after [208]). In the lower half of the image one can see a substantial area occupied by carbonates. Carbonates can also localize in the matrix forming rings and islands. They can share mixed regions with organic matter (OM) and clays. (b) Calcites in a form of veins. Carbonate-rich regions can span for several inches (after [65]). (c) Interaction of an open-mode fracture with a mineralized vein (after [108]). When hitting a natural fracture, an open-mode fracture may deviate and start propagating in the direction of the vein.

Acidizing is the oldest stimulation technology applied in oil and gas reservoirs [145]. Acid treatments fall into three categories: wellbore acidizing used to clean the wellbore surface, matrix acidizing used to reduce near-wellbore formation damage, and acid fracturing [163, 6]. Carbonate rocks are the most common targets for acidizing with hydrochloric acid (HCl) in 5-15% solution, which may result in formation of wormholes, highly branched channels preferential for reactive fluid flow [88, 68]. Acid fracturing in carbonates seeks to etch fracture surfaces so that

they remain conductive after closure [171].

Carbonates, however, are not the only type of rocks featuring high carbonate content: some organic-rich shales may contain a substantial amount of carbonates either in matrix (Fig. 3.1a) or localized in natural fractures (Fig. 3.1b). Matrix of some organic-rich shales, such as Barnett, Haynesville, and Eagle Ford, may contain as well over 50 % of carbonates [115, 183]. Barnett, Wolfcamp, and Haynesville shale formations also feature multiple systems of natural fractures, some of which are filled with calcite [65, 83, 204]. For example, the aperture of mineral-filled natural fractures in the Barnett Shale varies from 0.05 mm to 2.7 mm and their height – in field cores – has been documented as high as 80 cm [65]. These fractures are usually found in en-échelon arrays. The same study shows that the strike of the calcite-filled veins in the Barnett shale is predominantly oriented in northwest direction, which is perpendicular to the present-day maximum horizontal stress. In addition to thin mineralized veins, organic-rich shales (e.g. Vaca Muerta, Haynesville) may contain relatively thick (up to 10 cm) mostly bedding-parallel fibrous calcite veins (“beef”) [155, 5]. Owing to this calcareous nature of same hydrocarbon-bearing shales, it results appealing to perform hydraulic fracturing combined with acidizing as an enhanced stimulation technique in calcareous shales. A recent study suggests that shale acidizing can create a network of openings from 10 to 100  $\mu\text{m}$  in natural fractures due to non-uniform etching, resulting in channels that could increase the transmissibility of fractures and improve the productivity of acidized completions [208]. Vein-dissolution extent and reach may also be enhanced by carbonate localization. When a propagating open-mode frac-

ture encounters a mineralized natural fracture (i.e. mineralized vein), it can turn into the direction of the vein (Fig. 3.1c) or even split the vein in half [108]. Hence, shale acidizing combined with hydraulic fracturing could enhance fracture network complexity and mineral dissolution effectiveness since acid solutions would preferentially flow through localized carbonate interfaces.

The objective of this work is to explore the consequences of localized carbonate dissolution on the state of stresses of hydrocarbon-bearing shale formations imposed by shale acidizing. We attempt to justify acidizing of carbonate-rich shales as a means of improving production of hydrocarbons. In this study we put emphasis on stress reorientation and the potential enhancement of the size and permeability of the stimulated reservoir volume. Rather than looking at the effects of acidizing on shale matrix, we assess the effect of dissolution on change of local stress state and, therefore, on permeability enhanced by shear fracture reactivation and stress relaxation. We use linear elasticity and Mohr-Coulomb shear failure criterion to explore the influence of geometric characteristics of mineralized fractures, such as volume fraction and orientation, on changes of stresses imposed by localized mineral dissolution. Triaxial experiments conducted on a fractured shale seek to confirm expectations from analytical results. Reservoir-scale effects and implications of acidizing are simulated with the Finite Element Method by means of a thermo-elastic analogy.

### 3.2 Analytical model of stress relaxation induced by localized mineral dissolution

Consider an idealized shale formation with Young's modulus  $E$  and Poisson's ratio  $\nu$  (Fig. 3.2), subjected to in-situ stresses as follows: total vertical stress  $S_v$ , maximum total horizontal stress  $S_h$ , and minimum total horizontal stress  $S_h$ . The shale has continuous mineralized fractures of thickness  $h$ , spaced by a distance  $L$ , dipping at an angle  $\alpha$ , and striking at an angle  $\beta$  (counterclockwise from the direction of  $S_h$ ). As discussed above, natural fractures are frequently present in a systematic fashion, so that strike and dip of mineralized veins are consistent on a reservoir scale in a given formation. We additionally assume abundant non-mineralized natural fractures, some of which are critically-oriented with respect to the in-situ stresses.

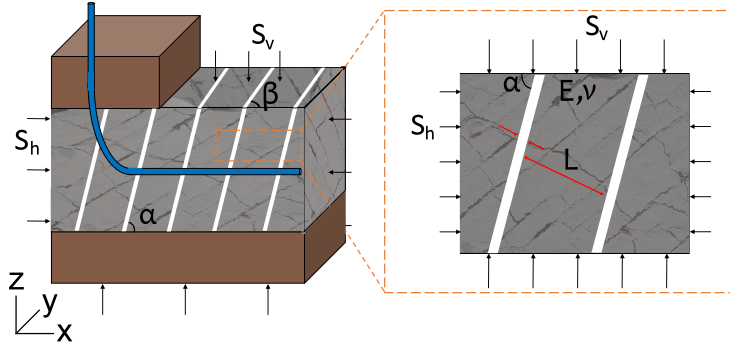


Figure 3.2: (a) Schematic representation of tight formation with a set of parallel mineralized fractures and abundant natural fractures subjected to in-situ stresses. (b) Representative elementary volume, where  $\alpha$  is the dip of the mineralized fractures,  $h$  is the thickness,  $L$  is the spacing between fractures,  $E$  is the shale Young's modulus, and  $\nu$  is the shale Poisson's ratio.

Let us find an upper-bound solution in which we assume that carbonates are

homogeneously dissolved along the fracture faces (net reduction in vein thickness). The assumption is reasonable for small areas considering rapid reaction rates with HCl, the fact that calcite veins are highly localized, and the shale matrix has an extremely low permeability, so that mineralized fractures would act as preferential flow paths. Part of the dissolved minerals are assumed to precipitate in the shale matrix after leak-off.

Total vertical stress remains constant assuming that the overburden does not change with time and no overarching stresses develop. The dissolution zone is assumed to be much larger than the representative elementary volume (REV) so that a perfect lateral containment condition applies (no lateral displacements). As dissolution progresses, the thickness of the veins decreases, and shale matrix expands laterally due to Poisson's effect. The following two subsections explore the parameters governing stress relaxation and required volume fraction needed for shear reactivation of critically-oriented fractures within the shale. Both stress relaxation and shear reactivation contribute to increases of permeability of the stimulated reservoir volume. We use the term "stress relaxation" to refer to reduction of compressive stress caused by the removal of the dissolved material rather than visco-elastic effects.

### 3.2.1 Dissolution of a single vein

Geometrical analysis of Fig. 3.2 permits finding strains  $\Delta\varepsilon_{xx}$  and  $\Delta\varepsilon_{yy}$  on the non-dissolved rock matrix induced by homogeneous dissolution  $\Delta h$  of a vein with dip angle  $\alpha$  and strike angle  $\beta$  (between the direction of minimum horizontal

stress  $S_h$  and the vein strike).

Assuming homogeneous dissolution along the vein faces and zero lateral displacement, the x-component of the displacement of the non-dissolved material on the edge of a vein is  $u_x = -\Delta h \sin \beta \cos(\pi/2 - \alpha)$ . The x-component of a vector perpendicular to the vein planes between two nearest veins is  $L_x = \frac{L}{\sin \beta \cos(\pi/2 - \alpha)}$ . The resulting strain  $\varepsilon_{xx}$  is given by the ratio of these two quantities  $\varepsilon_{xx} = u_x/L_x$ . The derivation of the strain component  $\varepsilon_{yy}$  is similar to that of  $\varepsilon_{xx}$ . Thus, we can write out the expressions for the components of horizontal strain as follows:

$$\begin{cases} \Delta \varepsilon_{xx} = -\frac{\Delta h}{L} \sin^2 \beta \sin^2 \alpha \\ \Delta \varepsilon_{yy} = -\frac{\Delta h}{L} \cos^2 \beta \sin^2 \alpha \end{cases} \quad (3.1)$$

resulting in total volumetric strain in the rock matrix  $\Delta \varepsilon_V = -\frac{\Delta h}{L} \sin^2 \alpha$ . Here and throughout the paper compressive stresses and strains are assumed positive. Assuming uniform vein spacing, one can write Eq. 3.1 in terms of volumetric fraction of carbonates  $f = \frac{h}{L}$  in a reservoir and the fraction of dissolved carbonates  $\chi = \frac{\Delta h}{h}$  as follows:

$$\begin{cases} \Delta \varepsilon_{xx} = -f \chi \sin^2 \beta \sin^2 \alpha \\ \Delta \varepsilon_{yy} = -f \chi \cos^2 \beta \sin^2 \alpha \end{cases} \quad (3.2)$$

Assuming linear isotropic elasticity, one can write the following expressions for the dissolution-induced variations in effective horizontal stresses  $\sigma_{xx}$  and  $\sigma_{yy}$ :

$$\begin{cases} \Delta \sigma_{xx} = -\frac{E}{1-\nu^2} f \chi (\sin^2 \beta + \nu \cos^2 \beta) \cos^2 \alpha \\ \Delta \sigma_{yy} = -\frac{E}{1-\nu^2} f \chi (\nu \sin^2 \beta + \cos^2 \beta) \cos^2 \alpha \end{cases} \quad (3.3)$$

Note that the variations in total horizontal stresses  $S_{xx}$  and  $S_{yy}$  are equal to those in horizontal effective stresses assuming that there is no change in pore pressure:

$\Delta S_{xx} = \Delta\sigma_{xx}$  and  $\Delta S_{yy} = \Delta\sigma_{yy}$ . The equations are analogous to those used to calculate horizontal stresses with a given tectonic strain.

The rock starts to manifest shear plastic behavior when the stress state reaches yield conditions, specified by Mohr-Coulomb failure criterion

$$\tau = C + \sigma_n \tan(\varphi), \quad (3.4)$$

where  $\tau$  is the yield shear stress,  $\sigma_n$  is the effective stress normal to the shear failure plane,  $C$  is the cohesive strength, and  $\varphi$  is the friction angle.

For the sake of simplicity, let us consider a case of vertical ( $\alpha = 90^\circ$ ) mineral veins striking perpendicular to minimum horizontal stress ( $\beta = 90^\circ$ ,  $S_{xx} = S_h$ ) in a normal faulting stress regime environment (Fig. 3.3a). Gradual dissolution results in a decrease of the minimum horizontal stress while the vertical stress remains constant (Fig. 3.3b). From Eq. 3.3, the change of effective minimum horizontal stress  $\sigma_h$  (assuming no change in pore pressure) due to uniform dissolution of veins is

$$\Delta\sigma_h = \sigma_h - \sigma_h^0 = -\frac{E}{1-\nu^2} f \chi, \quad (3.5)$$

where  $\sigma_h = S_h - p$  is effective horizontal stress after dissolution and  $\sigma_h^0 = S_h^0 - p$  is effective horizontal stress before dissolution.

Continued dissolution lowers the horizontal stress  $\sigma_h$  increasing stress anisotropy until a plastic limit is reached according to the shear failure properties of the formation. Using Mohr-Coulomb failure criterion (Eq. 3.4), this plastic limit is

$$\sigma_h = \sigma_v \frac{1 - \sin \varphi}{1 + \sin \varphi} - 2C \frac{1 + \sin^2 \varphi}{(1 + \sin \varphi) \cos \varphi} \quad (3.6)$$

Assuming perfect plastic material, upon continued dissolution the rock will yield preventing  $\sigma_h$  to decrease at the “elastic” rate, and the Mohr circle will stay tangent to the failure envelope. However, multiple phenomena may occur that affect fluid flow at failure, such as fracture dilation and fines production among others. Depending on effective confining stresses and the properties of the fractured rock, the shale may show strain-softening or strain-hardening behavior. Fig. 3.3b-c shows an example of dissolution-induced change in effective minimum horizontal stress for  $f = 10^{-3}$ ,  $E = 3 \times 10^6$  psi,  $\nu = 0.275$ ,  $\sigma_v = 5000$  psi,  $\sigma_{h0} = 1900$  psi,  $C = 0$  psi, and  $\varphi = 31^\circ$ . Zero cohesive strength implies that a large rock mass has natural fractures that are cohesionless and critically-oriented with respect to principal stresses.

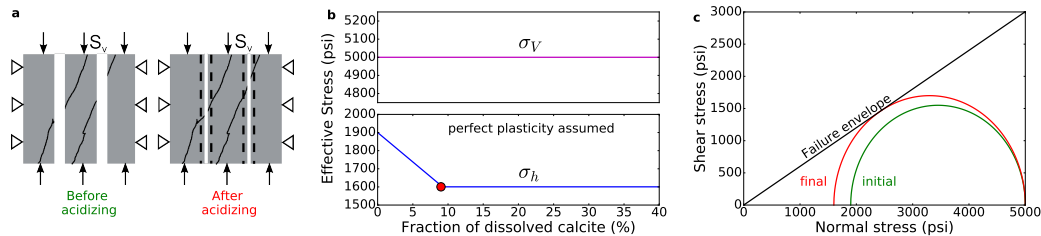


Figure 3.3: Effect of mineral dissolution. (a) Calcite veins dissolve and shale expands due to Poisson’s effect. (b) Change of effective stresses with dissolution. Perfect plasticity assumed: the red marker designates a perfect plastic yield transition. (c) Change of stress state represented as a movement of the respective Mohr’s circle. At the plastic transition point the circle is tangent to the failure envelope.

### 3.2.2 Critical amount of carbonates to attain shear reactivation

Using the concepts elaborated in Section 3.2.1, we estimate an upper-bound solution for the volume fraction of calcite veins a shale should contain in order to initiate shear reactivation of critically-oriented fractures in a reservoir subjected to

normal faulting stress regime. This consideration implies full dissolution of all the veins ( $\chi=1$ ). We assess the impact of two governing parameters of the problem: shale Young's modulus and initial vertical-to-horizontal stress anisotropy  $\sigma_v - \sigma_h^0$ . Eq. 3.7 combines Eq. 3.3 and Eq. 3.6, and predicts the critical volume fraction  $f_c$  of calcite required to reactivate critically-oriented natural fractures in shear as function of the vertical and initial minimum horizontal effective stresses  $\sigma_v$  and  $\sigma_h^0$ :

$$f_c = \frac{1 - \nu^2}{E \cos^2 \alpha (\sin^2 \beta + \nu \cos^2 \beta)} \left[ \sigma_h^0 - \sigma_v \frac{1 - \sin \varphi}{1 + \sin \varphi} \right] \quad (3.7)$$

The equation assumes negligible change in pore pressure. To demonstrate the application of Eq. 3.7, we analyze critical volume fraction of veins  $f_c$  as a function of initial normalized vertical-to-horizontal stress anisotropy  $\frac{\sigma_v - \sigma_h^0}{\sigma_v}$  (varied as an independent variable while keeping other parameters fixed as follows: total vertical stress  $S_v = 8200$  psi, pore pressure  $p = 4000$  psi,  $\nu = 0.25$ ,  $C = 0$ ). Fig. 3.4a shows the  $f_c$  for three shales with different stiffnesses ( $E = 2 \times 10^6$  psi,  $4 \times 10^6$  psi, and  $8 \times 10^6$  psi) while the same friction angle  $\varphi = 30^\circ$ . In the isotropic case ( $\sigma_v = \sigma_h^0$ ) one needs to dissolve the most (0.3-1.3 mm per every meter of shale) calcite to reactivate critically-oriented fractures in shear. As  $\sigma_v - \sigma_h$  increases, lesser amount of calcite is required. For typical values of vertical-to-horizontal stress anisotropy  $\sim 1700-2500$  ( $\frac{\sigma_v - \sigma_h^0}{\sigma_v} \sim 0.45 - 0.60$ ) psi in hydrocarbon-producing shales in the US, the minimum amount of calcite required to reactivate fractures lays between 50 and 500  $\mu\text{m}$  every meter of shale, an amount that is not inconceivable.

Fig. 3.4b illustrates the effect of pore pressure ( $p = 4100$  psi,  $p = 6500$  psi, and  $p = 7800$  psi) on the critical amount of mineralized veins  $f_c$ . The rock Young's

modulus is  $E = 4 \times 10^6$  psi, and all other parameters are the same as in the previous example. Overpressured shales require to dissolve less mineralized veins (as low as  $f_c = 10^{-5}$ ) than reservoirs with normal pressure.

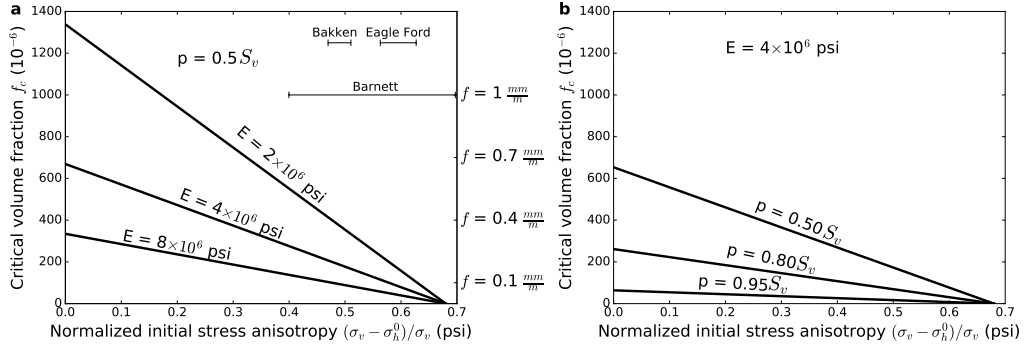


Figure 3.4: Minimum volume fraction of calcite veins in shale necessary to attain reactivation of critically-oriented natural fractures assuming full dissolution and vein strike perpendicular to  $S_h$ . (a) Impact of Young's modulus: less calcite is to be dissolved to reactivate fractures in a stiff shale. (b) Impact of pore pressure: less calcite is required to fail an overpressured shale.

### 3.3 Experimental evidence of stress relaxation

In this section we show experimental evidence of the thought experiment presented in Fig. 3.3. The experiment consists of dissolving localized mineral filling in a shale rock subjected to no-lateral-displacement condition, i.e., zero lateral strain.

#### 3.3.1 Rock sample

Experiments were conducted using rock plugs from field cores retrieved from the Eagle Ford formation. The sample was cut to 1 inch in diameter and 2.28

inches in length. The sample fractured during the process of coring leaving a planar fracture cutting through the core and oriented at approximately  $79^\circ$  with respect to the endface. The static Young's modulus  $E=5.3\times10^6$  psi and Poisson's ratio  $\nu = 0.22$  were measured with triaxial tests by axial loading with constant confining stress. This fractured sample was used to create a synthetic mineral vein by placing air-dry NaCl grains into the fracture, putting the two halves back together, and applying confining stresses until observing negligible creep strains. NaCl was used instead of CaCO<sub>3</sub> to simplify the procedure and dissolve minerals with fresh water. The shale did not exhibit appreciable swelling strains upon the contact with fresh water.

### 3.3.2 Procedure

The sample was tested in a triaxial cell equipped with local strain transducers (Terratek 20,000 psi triaxial system). Lateral (radial) strain  $\varepsilon_h$  is measured perpendicular to the fracture strike. The experiment consists of (1) taking the sample to a nearly isotropic initial state of stress at approximately 500 psi of confining stress and zero pore pressure (where creep occurs and deformation reach asymptotic values) and (2) injecting fresh water into the sample to dissolve the mineral filling while simultaneously keeping constant lateral strain perpendicular to the fracture strike. Constant lateral strain  $\varepsilon_h$  was achieved by modifying confining (radial) stress. During this entire process the system records confining stress, axial stress, upstream pore pressure (atmospheric pressure held downstream), and axial and radial strains.

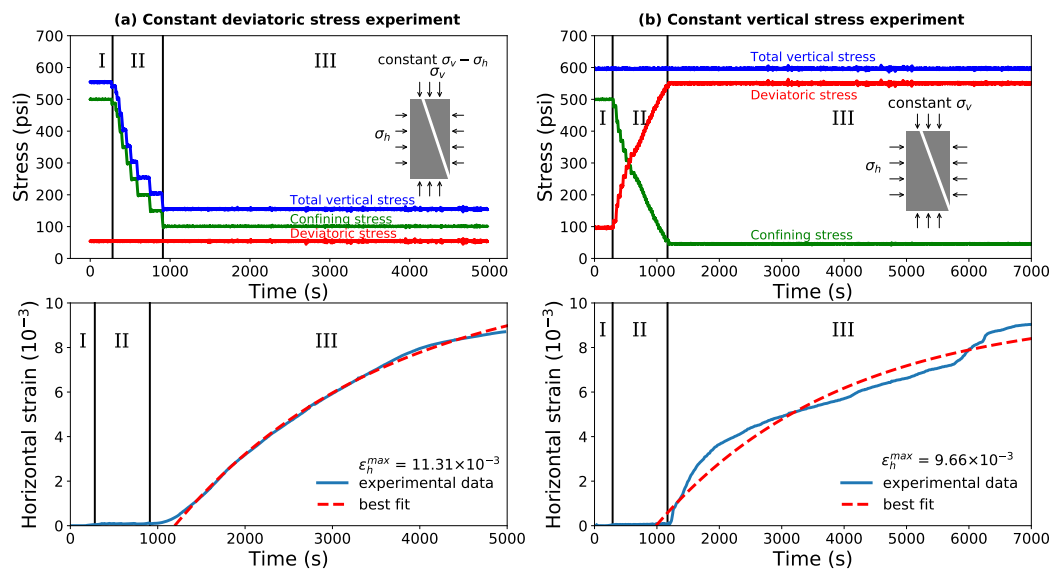


Figure 3.5: Vein dissolution experiments monitoring axial and deviatoric stresses, confining pressure, and horizontal strain as functions of time. Stages: (I) before dissolution commences, (II) during dissolution while lateral strain is maintained constant, (III) vertical and horizontal stresses are held, sample contracts as a result of dissolution. (a) Constant deviatoric stress experiment. (b) Constant vertical stress experiment.

### 3.3.3 Vein dissolution results

#### 3.3.3.1 Constant deviatoric stress

The sample was prepared with 0.35 g of NaCl distributed in fracture area of approximately 10 cm<sup>2</sup>. Assuming porosity of fracture filling salt  $\phi_f = 0$  yields a minimum fracture thickness equal to  $h = 159 \mu\text{m}$ , and  $\phi_f = 0.47$  yields vein thickness  $h = 297 \mu\text{m}$ . For the first experiment the rock sample was subjected to a constant-lateral-strain condition by means of varying lateral stress during dissolution. Deviatoric stress was set to remain constant during the experiment. The experimental results are shown in Fig. 3.5a. The sample was loaded with axial (vertical) stress of 550 psi and confining (lateral) stress of 500 psi constituting an initial deviatoric stress of 50 psi. After the creep strains became negligible  $1.67 \times 10^{-9} \text{ s}^{-1}$  (data not shown in figure), fresh water was injected to dissolve the salt filling the fracture. During stage I water advances through air-filled tubes and does not reach the sample yet and, therefore, it does not affect stresses. When water reaches the sample (the beginning of stage II), salt dissolution immediately commenced. The pore pressure has a small value of a few psi and was neglected when computing effective stresses. Axial and confining stresses were changed simultaneously in steps to maintain the original lateral strain keeping the value of deviatoric stress equal to 50 psi. Upon reaching 100 psi of lateral stress, stresses were fixed constant letting the salt dissolve completely without holding a constant lateral in any longer (stage III). Lateral stress was not lowered below 100 psi to avert shear slip and preserve the sample for more experiments. During stage III, the lateral strain perpendicular to the plane of fracture approached an asymptotic value of  $\varepsilon_h^{max} = 11.3 \times 10^{-3}$  obtained

by curve-fitting and extrapolation with exponential function

$$g(t) = c \left[ 1 - \exp\left(\frac{-3(t - t_0)}{a}\right) \right], \quad (3.8)$$

where  $a$ ,  $c$ , and  $t_0$  are fitting coefficients.

These maximum strain data can be used to estimate the actual fracture thickness  $h$ , and the amount of salt  $\chi_{II}$  dissolved during stage II. According to Eq. 3.1, the thickness of the salt-filled fracture was  $h = \frac{\varepsilon_h^{max} D}{\sin^2 \alpha} = 297 \mu\text{m}$ , ( $D$  is the diameter of the sample) which yields fracture-filling porosity  $\phi_f = 0.47$ . Using Eq. 3.3, the amount of salt dissolved during stage II was  $\chi_{II} = 16.8 \%$ .

### 3.3.3.2 Constant total vertical stress

For the second experiment 0.22 g of salt were distributed in the same fracture area of approximately  $10 \text{ cm}^2$ . During the second experiment the sample was subjected to a constant-lateral-strain condition by means of manipulating confining stress while the total axial stress was held constant. The experimental results are shown in Fig. 3.5b. The sample was loaded with axial (vertical) stress of 600 psi and confining (lateral) stress of 500 psi constituting deviatoric stress of 100 psi (neglecting low pore pressure). After the creep strains became negligible, the system (fluid-bearing tubes) began to fill up with fresh water (stage I). When water reached the sample (stage II), the confining stress was lowered to 50 psi in steps in order to hold fixed the value lateral strain perpendicular to the mineralized fracture face, while the axial stress was kept constant at 600 psi. Upon reaching the value of 50 psi, the confining stress was fixed letting the sample contract due to mineral dissolution (stage III). Thus, the deviatoric stress increased from 100 psi to 550 psi during

stage II. During stage III, the lateral strain perpendicular to the plane of fracture approached a quasi-asymptotic value of  $\varepsilon_h^{max} = 9.66 \times 10^{-3}$  obtained by best-fit with Eq. 3.8. According to Eq. 3.1, vein thickness is  $h = 255 \mu\text{m}$ , which yields fracture-filling porosity  $\phi_f = 0.61$ . Using Eq. 3.3, the amount of salt dissolved during stage II is  $\chi_{II} = 22.1 \%$ .

## 3.4 Reservoir scale simulation

### 3.4.1 Analogy of mineral dissolution with anisotropic thermal cooling

In this section we seek to investigate the implications of mineral-vein dissolution during acidizing at the reservoir-scale. In this study we put emphasis on changes of stresses rather than on reactive fluid flow. The effects of stress relaxation are simulated through thermal stresses and the advance of the acidizing front through temperature diffusion.

Let us consider a rock volume subjected to constant compressive effective stresses and undergoing dissolution of veins, so that its bulk volume decreases as a result of solid mass loss and active compressive stresses. The same volumetric effect can be achieved with thermal cooling. Similarly, if one fixes the displacement at boundaries of a compressed rock volume (instead of fixing stresses), mean stress would decrease upon vein dissolution. An identical response can also be achieved with thermal cooling. Problems in thermoelasticity have been well-studied [131]. Decrease of fracture gradient due to drilling with cold mud and changes of reservoir stresses due to cold fluid injection are examples of induced thermal stresses in petroleum engineering [73, 1]. Potential applications of cold fluid injection have

also been suggested for hydraulic fracturing [51].

Section 3.2.1 shows that vein dissolution under constant horizontal displacement results in a decrease of stress perpendicular to the vein  $\Delta\sigma_h = -\frac{E}{1-\nu^2}f\chi$  (Eq. 3.5) until a yield stress is achieved, where  $f$  is the volume fraction of calcite in a reservoir and  $\chi$  is the fraction of dissolved vein. The same effects can be achieved considering an anisotropic thermoelastic solid with a decrease of temperature  $\Delta\theta$ :

$$\Delta\sigma_h = \frac{E}{1-2\nu}\eta_h\Delta\theta, \quad (3.9)$$

where  $\eta_h$  is a horizontal component of the rock thermal expansion tensor  $\boldsymbol{\eta}$ . The anisotropic thermal expansion tensor  $\boldsymbol{\eta}$  can be manipulated to account for the strike and dip of mineralized natural fractures. For example, in the case of vertical veins oriented perpendicular to the direction of minimum horizontal stress  $\sigma_h$ , only one component of the thermal expansion tensor will be non-zero. Hence combining Eq. 3.5 and 3.9, the change of temperature  $\Delta\theta$  required to induce a change in stress equivalent to dissolving a fraction  $\chi$  of minerals with volume fraction  $f$  is

$$\Delta\theta = -\frac{(1-2\nu)}{(1-\nu^2)}\frac{f\chi}{\eta_h} \quad (3.10)$$

In general, the system of equations of thermoelasticity with isotropic mechanical behavior and anisotropic thermal dilation tensor is as follows:

$$\begin{cases} \nabla_i\sigma_{ij} = 0 \\ \sigma_{ij} = \lambda\varepsilon_{kk}\delta_{ij} + 2G\varepsilon_{ij} + (3\lambda+2G)\eta_{ij}\theta \\ \frac{d\theta}{dt} = \frac{\kappa}{\rho C_p}\nabla^2\theta \end{cases} \quad (3.11)$$

where  $\theta$  is temperature,  $\kappa$  is rock thermal conductivity,  $\rho$  is the rock bulk density,  $C_p$  is the rock heat capacity,  $\lambda$  and  $G$  are Lamé's first parameter and rock shear

modulus, respectively, and  $\delta_{ij}$  is the identity tensor or Kronecker delta. We use this system of equations as a simplification of reactive fluid flow. Since transient effects of mineral dissolution are out of the scope of this study, the value of thermal diffusivity  $D = \frac{\kappa}{\rho C_p}$  is selected arbitrarily in order to achieve faster numerical simulation. To solve this system, we use FreeFem++ Finite Element Method software [84]. Note that the proposed thermo-elastic model can only be utilized to describe the behavior of the material inside the yield surface.

A validation of the presented model is provided in Fig. 3.6. A thermoelastic domain with initial minimum effective horizontal stress of  $\sigma_h^0 = 1900$  psi was subjected a slow uniform decrease in temperature of 10 K. Upon cooling, minimum horizontal stress decreases depending on the imposed value of the horizontal component of heat expansion tensor  $\eta_h$ . Analytical and numerical solution of three cases were obtained for rocks with  $\eta_h = 1 \times 10^{-5} \text{ K}^{-1}$ ,  $2 \times 10^{-5} \text{ K}^{-1}$ , and  $5 \times 10^{-5} \text{ K}^{-1}$ . Numerical solution matches the analytical one for all values of  $\eta_h$ . We obtain volume fractions of mineralized veins equivalent to the aforementioned values of horizontal thermal dilation facilitating the analogy between thermoelastic cooling and mineralized-vein dissolution and assuming that a decrease in temperature of 10 K corresponds to dissolution of all mineralized veins in the domain based on Eq. 3.10. Therefore, as shown in Fig. 3.6, cooling down rocks by 10 K with horizontal thermal expansion  $\eta_h = 0.5 \times 10^{-5} \text{ K}^{-1}$ ,  $1.0 \times 10^{-5} \text{ K}^{-1}$ , and  $2.0 \times 10^{-5} \text{ K}^{-1}$  is equivalent to completely dissolving volume fractions of carbonates  $f = 1 \times 10^{-4}$ ,  $2 \times 10^{-4}$ , and  $4 \times 10^{-4}$ .

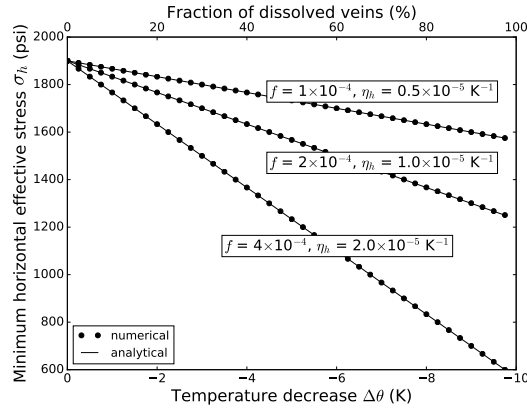


Figure 3.6: Minimum horizontal effective stress as a function of decrease in reservoir temperature and volume fraction of carbonates in veins. Anisotropic thermal cooling and mineral dissolution have similar effects on horizontal stress. Thermal expansion coefficient can be used to estimate an equivalent volume fraction of carbonates.

### 3.4.2 Case problem

Let us consider a typical case of a multi-stage hydraulic fracturing in the Barnett shale. The simulation parameters are taken from [158] and listed in the Table 3.1.

#### 3.4.2.1 State of stresses during consecutive fracturing

First we analyze the effect of acidizing and mineral dissolution in a domain with a single hydraulic fracture on the left side of the domain (Fig. 3.7) assuming three different configurations of mineralized veins: (a) two sets of mineralized veins with strikes  $0^\circ$  and  $90^\circ$  and volumetric fraction of veins  $f = 4 \times 10^{-4}$ , (b) one set of mineralized veins parallel to the direction of  $S_h$  (strike =  $0^\circ$ ) and volumetric fraction of veins  $f = 2 \times 10^{-4}$ , (c) one set of mineralized veins with perpendicular to the

Table 3.1: Typical in-situ stresses, shale properties and multi-stage hydraulic fracturing geometry for the Barnett Shale

Property	Value
Pay zone Young's Modulus $E$ (psi)	$7.3 \times 10^6$
Pay zone Poisson's Ratio $\nu$	0.2
$S_V$ (psi)	7000
$S_H$ (psi)	6400
$S_h$ (psi)	6300
Pore pressure $p$ (psi)	4000
Fracture half-height (ft)	150
Fracture half-length (ft)	500
Fracture maximum width (mm)	4

direction of  $S_h$  (strike =  $90^\circ$ ) and volumetric fraction of veins  $f = 2 \times 10^{-4}$ . According to Eq. 3.10, this amount of veins corresponds to isotropic thermal expansion coefficient  $\eta_h = 1 \times 10^{-5} \text{ K}^{-1}$  (with  $\Delta\theta = -10 \text{ K}$ ). The fracture is initially propped and preserves maximum aperture  $w = 4 \text{ mm}$  throughout the simulation. The actual domain size is 2000 feet  $\times$  2000 feet and its boundaries are set with displacement boundary conditions to replicate in-situ stresses and the opening of the hydraulic fracture. Fig. 3.7 shows total stresses 10 feet from the fracture (near-fracture) and 400 feet from the fracture (far-field) as functions of the distance traveled by the dissolution front. This distance is the distance from the center of the hydraulic fracture measured in x-direction to the most distant point where the amount of dissolution is equal to or more than 90%.

Fig. 3.7a shows total stresses as functions of the distance traveled by the dissolution front for a case (a) with two systems of orthogonal mineralized veins. Horizontal stresses  $S_{xx}$  near the fracture and in the far field decrease simultaneously

(due to stress continuity) to a maximum change of approximately 500 psi when the dissolution front reaches 400 ft. Horizontal stresses  $S_{yy}$  changes rapidly near the fracture as dissolution front reaches this region faster than the far-field region. At later times horizontal stress  $S_{yy}$  decreases in the far field as well.

Fig. 3.7b shows total stresses as functions of the distance traveled by the dissolution front in the case (b) one set of mineralized veins parallel to the minimum horizontal stress  $S_h$  (strike =  $0^\circ$ ). The initial stress state is the same as in case (a). As expected, horizontal stress  $S_{xx}$  does not significantly vary due to mineral dissolution because it does induce strains in the x-direction. Horizontal stress  $S_{yy}$  drops in a manner similar to the case (a) and reaches a maximum change of approximately 500 psi when the dissolution reaches the far-field zone.

Fig. 3.7c shows total stresses as functions of the distance traveled by the dissolution front in the case (c) mineralized veins perpendicular to maximum horizontal stress  $S_H$  (strike =  $90^\circ$ ). A far reaching dissolution front is not realistic in this case unless mineralized veins have a dip far from  $90^\circ$  or other conductive fractures can transport the acid. The initial stress state is the same as in cases (a) and (b). Mineral dissolution lowers horizontal stresses  $S_{xx}$  near the hydraulic fracture and in the far-field region with the stress near the fracture being slightly higher than that in the far-field due to proppant placement.

### 3.4.2.2 State of stresses during alternate fracturing and stress reorientation

We now consider the effect of dissolution for an alternate fracturing scenario. The domain size is 400 ft  $\times$  2000 ft. Two initially-propped fractures spaced

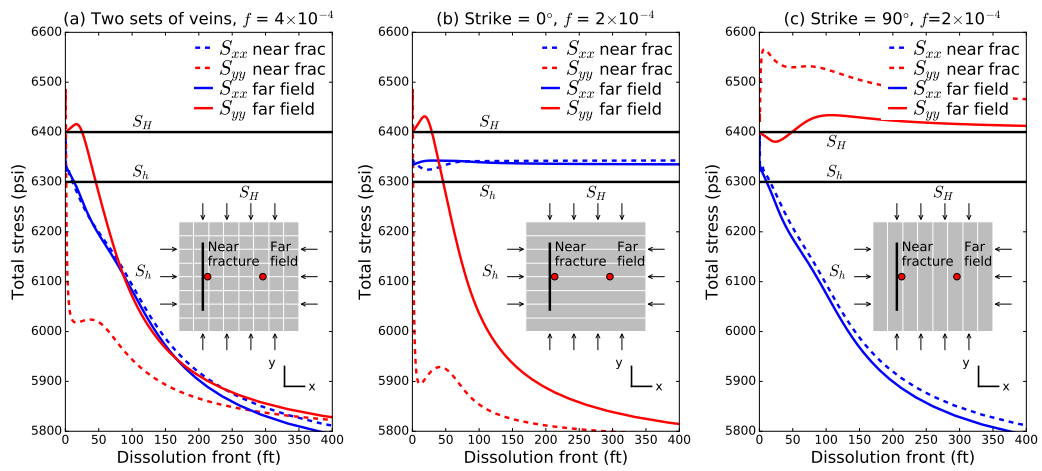


Figure 3.7: Effect of dissolution in a consecutive fracturing application. Total horizontal stresses in the near-fracture and far-field (at 400 ft) regions as functions of a distance traveled by a dissolution front. (a) Isotropic case - 2 sets of veins oriented perpendicular and parallel to  $S_h$ . One can see both reduction in  $S_{xx}$  and  $S_{yy}$ . (b) Veins are oriented parallel to  $S_h$ . Only  $S_{yy}$  decreases. (c) Veins are oriented perpendicular to  $S_h$ . Only  $S_{xx}$  decreases.

by 400 ft are imposed on the right and left sides of the domain. Assuming multiple parallel and uniformly-spaced hydraulic fractures outside of the domain, we impose constant-displacement boundary conditions in the simulation due to the symmetry of the problem. A volumetric fraction of veins  $f = 4 \times 10^{-4}$  is assumed to be homogeneously distributed in the domain (Fig. 3.8). Alternate fracturing scenario implies the placement of the third hydraulic fracture between those previously propped in the middle of the domain [157].

Fig. 3.8 shows horizontal compressive stresses in the middle of the domain as functions of the overall amounts of carbonates dissolved in the domain for two cases of mineralized veins orientation: perpendicular and parallel to the direction of minimum horizontal stress  $S_h$ . Initially, horizontal stress  $S_{xx}$  is about 150 psi higher than in-situ minimum horizontal stress  $S_h$  because of stress shadow effects. Therefore, the local minimum principal stress is not aligned with the far-field minimum in-situ stress, which makes the third fracture propagate in the x-direction, thus rendering the alternate fracturing scenario unfavorable with the current fracture spacing.

Fig. 3.8a shows how compressive horizontal stresses  $S_{xx}$  and  $S_{yy}$  alter during mineral dissolution in the case of vein strike perpendicular to  $S_h$ . Similar to the case of consecutive fracturing,  $S_{xx}$  reduces with vein dissolution while  $S_{yy}$  stays relatively constant. When about 20% of all veins in the domain are dissolved,  $S_{xx}$  reaches the value of minimum in-situ stress  $S_h$ . At this moment the local minimum principal stress is aligned with the direction of far-field minimum in-situ stress  $S_h$ . During subsequent dissolution horizontal stress  $S_{xx}$  keeps decreasing reaching a

minimum value of approximately 5820 psi. This case favors alternate fracturing scenario implying that shale acidizing can be applied to reorient principal stresses hence reducing hydraulic fracturing spacing. Either a dip  $\alpha \neq 90^\circ$  or strike  $\beta \neq 0^\circ$  may favor the dissolution front extent in real settings.

Fig. 3.8b shows how compressive horizontal stresses  $S_{xx}$  and  $S_{yy}$  change during mineral dissolution in the case of mineralized fractures parallel to the direction of minimum horizontal stress  $S_h$  (strike = 0). Horizontal stress  $S_{xx}$  does not significantly change due to dissolution and stays about 200 psi above the minimum horizontal in-situ stress  $S_h$ . Horizontal stress  $S_{yy}$  reduced significantly to the value of approximately 5700 psi, which is lower than the minimum horizontal in-situ stress  $S_h$ . Hence, mineral dissolution of veins with zero strike exacerbates the alternate fracturing scenario increasing the minimum allowed hydraulic fracture spacing.

### 3.4.2.3 Reactivation of natural fractures due to acidizing

Let us consider another effect of mineral dissolution: reactivation of critically-oriented natural fractures. The simulation domain is the same as in Section 3.4.2.2. Assuming volume fraction of carbonate veins  $f = 2 \times 10^{-3}$ , vertical veins (dip  $\alpha = 90^\circ$ ) with strike  $\beta = 45^\circ$  (so that dissolution front may propagate in the direction perpendicular to the hydraulic fractures), constant total vertical stress  $S_V$  and pore pressure  $p = 4000$  psi, we calculate the decrease of horizontal stress  $S_{xx}$  due to mineral dissolution as shown in Fig. 3.9a. We assume the presence of critically-oriented natural fractures and reservoir-scale cohesive strength of the shale  $C = 0$

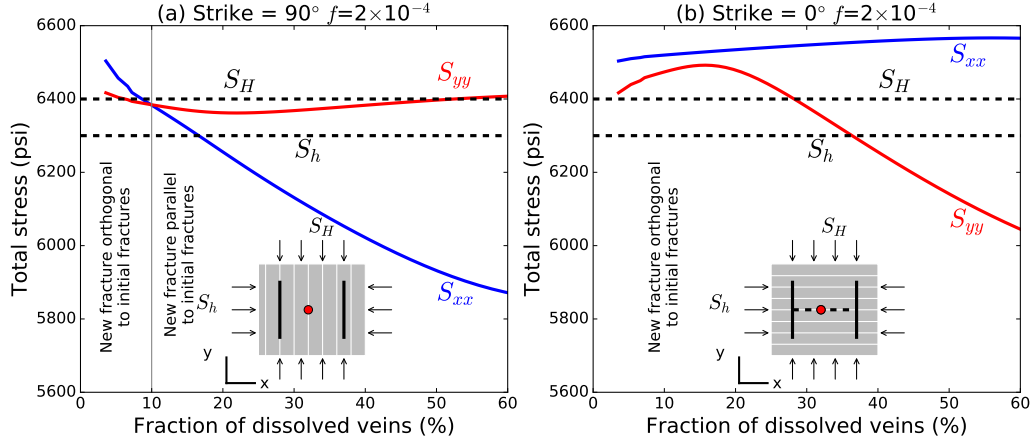


Figure 3.8: Alternate fracturing. (a) Veins are oriented perpendicular to  $S_h$ . Initially higher  $S_{xx}$  (because of stress shadows) drops below  $S_{yy}$  due to acidizing. Without acidizing a new fracture placed in the middle would propagate in x-direction instead of y-direction. (b) Veins are oriented parallel to  $S_{hmin}$ . Initially low  $S_{yy}$  reduces below  $S_h$ . A new fracture always propagates in x-direction.

and friction angle  $\phi = 31^\circ$ . With these parameters, shear failure prescribed by Mohr-Coulomb failure criterion occurs at minimum horizontal stress  $S_h = 4980$  psi. At approximately 20% of dissolution horizontal stress  $S_{xx}$  decreases to the yield stress and cannot decrease any more (our elastic model is not able to capture this effect). The Mohr's circles corresponding to the initial and failure stress states are shown in Fig. 3.9b. Similarly to the analytical solution presented in Fig. 3.3, Mohr's circle grows in diameter due to increase stress anisotropy until it meets the shear failure criterion.

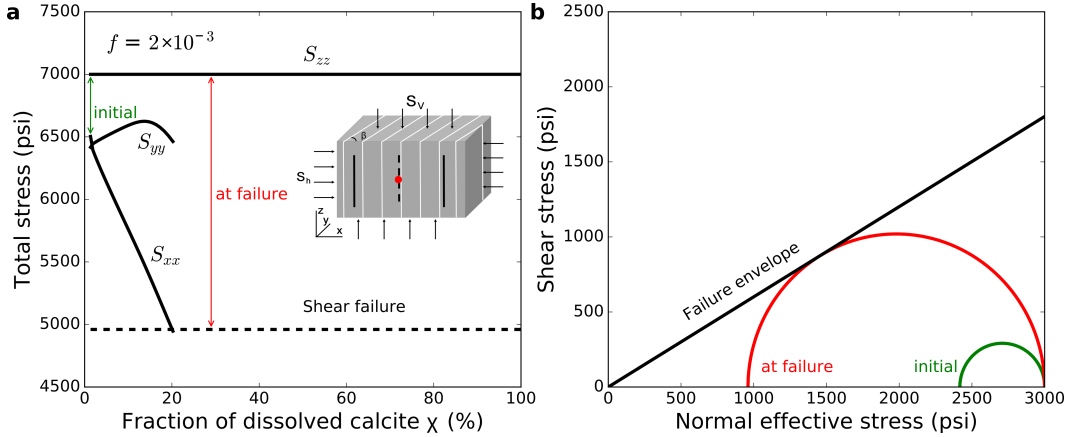


Figure 3.9: Alternate fracturing: effect of mineral dissolution on critically-oriented natural fracture reactivation. Vertical mineralized veins with strike  $\beta = 45^\circ$  and dip  $\alpha = 90^\circ$ . (a) Total vertical and horizontal stresses as functions of the overall amount of dissolution. (b) Mohr's circle corresponding to the stress state before dissolution and the shear failure point.

## 3.5 Discussion

In this study, we provide evidence that effective dissolution of mineralized veins may significantly alter the state of stresses in carbonate-rich shale reservoirs. The results of the study highlight that dissolution of a fairly small amount of minerals may decrease horizontal stress several hundreds of psi in typical shale reservoirs. Experimental observations support these findings. The conceptual idea, however, needs to address several issues in order to be implemented in the field, some of these are discussed in the following subsections.

### 3.5.1 Uniform dissolution versus etching

Core-scale laboratory experiments show that the assumption of uniform dissolution may not be realistic [208]. Non-uniform etching, instead, results in lower

amount of “vein ” shrinkage compared to uniform dissolution. This issue can be circumvented by introducing a non-uniform etching coefficient  $\zeta$  ( $0 < \zeta < 1$ ) and modifying Eq. 3.5 as follows:

$$\Delta\sigma_h = \frac{E}{1 - \nu^2} f \zeta \chi, \quad (3.12)$$

Non-uniform etching can also result in early acid breakthrough leaving veins behind not dissolved. Strong and fast-reaching acids would favor a short dissolution front with more effective vein dissolution. A weak and slow-reaching acid would favor long-reach of the dissolution front with patchy distribution of dissolved channels and minor effect on rock strain. In fact, some practices recommend the use of acid retarders to take advantage of these far-reaching dissolution channels [94, 96]. Rigorously, dissolution patterns will depend on reactive transport properties mentioned in the next section.

### 3.5.2 Reactive fluid flow modeling

Although thermoelasticity can mimic dissolution-induced stress reduction, it does not allow realistic simulation of mass and species transport. For example, mineral dissolution maximizes stress relaxation in the case of mineralized veins perpendicular to the direction of minimum in-situ stress. However, this vein configuration obstructs the reactive fluid flow perpendicular to the main hydraulic fracture, thus impairing the effect of acidizing. Hence, a reservoir-scale reactive-flow model is required to predict the propagation of acid front and the interaction of the acidic fluid with the reactive minerals [171, 62, 124]. Additionally, the model should be capable of modeling fluid flow in heterogeneous layered and fractured rocks

[66, 201]. The advection-reaction-diffusion model should consider several stages of reactive fluid flow: (1) transient acid leak-off into induced unpropped fractures, (2) leak-off into the rock matrix, and (3) a flowback stage.

Additional issues to consider are production of CO<sub>2</sub> and reprecipitation of the dissolved minerals [63, 191, 206]. Carbon dioxide CO<sub>2</sub> is one of the reaction products of carbonate acidizing. In tight low-permeability reservoirs the formation of CO<sub>2</sub> may potentially cause a pore-pressure increase in the formation. Pressure increase due to CO<sub>2</sub> formation may contribute to the fracture propagation during the shut-in stage. The minerals dissolved from the mineralized veins can potentially reprecipitate in fractures farther during shut-in and flowback impairing fracture permeability and preventing stress relaxation. This effect, however, may not be of significant importance since sometimes about a half of the injected fluid flows back within several hours of the injection [70].

### 3.5.3 Impact of stress relaxation on permeability

As discussed in Section 3.4.2, decreasing horizontal stress can be used to reduce hydraulic-fracture spacing or reactivation of critically-oriented natural fractures. Permeability of fractured media is often characterized with an exponential relationship with respect to effective stress:  $k = k_0 \exp^{\gamma\Delta\langle\sigma\rangle}$ , where  $\gamma$  is fracture compressibility and  $\Delta\langle\sigma\rangle$  is the difference between the current mean effective stress and the initial mean effective stress [161]. Therefore, horizontal stress relaxation caused by dissolution of mineralized veins may reduce the closure of natural or induced-unpropped fractures, which associated with pore pressure depletion, thus

causing permeability enhancement in the proximity of hydraulic fractures. Additionally, an increase in vertical-to-horizontal stress anisotropy may increase permeability via dilation of critically-oriented natural and induced unpropped fractures [128, 160]. These permeability-enhancement mechanisms are also common in coal reservoirs where gas desorption-induced rock matrix shrinkage results in stress relaxation [130, 122].

More complex numerical models were also proposed to quantify changes fracture aperture and permeability changes due to stress state alterations [113, 112]. In contrast to fracture opening and dilation, proppant embedment can aggravate permeability of propped fractures [49]. Proppant embedment can be exacerbated by matrix acidizing that may reduce shale hardness [195, 208].

We expect the overall impact of shale acidizing on fracture permeability to be positive given a reasonable amount of favorably-distributed mineralized veins. This increase in permeability may improve short-term recovery factors when the effect of dissolution on stresses is comparable to that of pore pressure depletion. Pore pressure depletion effects in shales are discussed [18].

### 3.6 Conclusion

Localization of carbonates in mineralized veins in shales suggests an opportunity for utilizing acidizing and mineral dissolution to manipulate stresses in the subsurface in order to enhance hydrocarbon production. Reduction of mean effective stress and increase of deviatoric stresses are advantageous in shale reservoirs because they increase fracture permeability.

A closed-form solution has been derived to quantify decreases in horizontal stresses due to dissolution of mineralized veins assuming uniform re-distribution of minerals, constant vertical stress, and no change in pore pressure. This model can be utilized to characterize shale reservoirs as potential candidates to acidizing. We applied the derived model to estimate the critical amount of mineralized veins in various hydrocarbon-bearing shale reservoirs and showed that dissolution of a reasonable fraction of mineralized veins is enough to cause appreciable changes of stress that may conduct the reactivation of critically-oriented natural fractures.

Triaxial experiments on a fractured shale confirm the analytical results. During those experiments, horizontal stress applied to the sample reduced due to the dissolution of a salt-filled vein. The derived analytical solution was utilized to obtain the total and dissolved volumetric fractions of salt confirming the applicability of the model.

We have shown that dissolution of mineralized veins has a similar effect on the stress state as thermal-induced anisotropic shrinkage and derived an conversion equation between a decrease in temperature of a thermoelastic domain and a dissolved fraction of mineralized veins. FEM-based reservoir-scale numerical simulations that use an analogy with thermoelasticity showed that mineral dissolution can be used to mitigate local principal stress reorientation and reduce spacing between hydraulic fractures in conventional and alternate fracturing scenarios. Additionally, numerical simulation confirmed that mineral dissolution can result in increases of vertical-to-horizontal stress anisotropy that can potentially lead to reactivation of critically-oriented natural fractures in shale reservoirs. Changes in reservoir stresses

caused by mineral dissolution are expected to increase reservoir permeability and improve recovery factors due to the opening and dilation of natural and unpropped fractures.

Although the experiments, analytical, and numerical solutions support stress alteration induced by localized mineral dissolution, other factors need to be taken into account in order to extend applications to field conditions. Some of these factors include: (1) actual flow in fractured media, (2) acid leak-off in shale matrix, (3) acid consumption with mineral dissolution, (4) mineral precipitation/scaling and effects on permeability, and (5) reactive transport instabilities such as wormhole-like dissolution patterns that could bypass mineralized veins.

## **Chapter 4**

# **Fracture propagation in heterogeneous porous media: pore-scale implications of mineral dissolution**

### **4.1 Introduction**

Open-mode fractures in the subsurface are associated with the movement of pressurized fluids [166], although other phenomena, such as stress concentration around cavities, elastic mismatch induced cracking, and thermal stresses, among others, may result in propagation of open-mode fractures as well [15, 104]. Open-mode fractures in homogeneous media, such as metals, polymers, and some ceramics, tend to be planar because tensile stresses concentrate near the fracture tips and do not deviate due to homogeneity in material properties [12]. In the case of an anisotropic stress state, open-mode fractures tend to align perpendicularly to the minimum principal stress [90].

Fracture propagation depends on the flaw size, and, therefore, simple material strength criteria are not sufficient to characterize fracture propagation. Linear Elastic Fracture Mechanics (LEFM) introduced the concept of the energy release rate [76, 92]. J-integrals help account for non-linear material behavior at the tips of ductile fractures [151]. Materials subjected to long-term loads may exhibit fracture propagation with velocity proportional to stress-intensity, a regime known as

subcritical fracture propagation [11]. These types of non-linear behavior cannot be fully characterized by LEFM [8].

Fractures in heterogeneous media may deviate from the original plane of propagation resulting in “tilt and twist” fracture configurations [106]. Tilt and twist occurs when a shear stress component at the fracture tip is not zero [12]. In addition to non-planar fracture propagation, the presence of heterogeneities, particularly mechanical barriers and planes of weakness, may result in fracture bifurcation or branching [188]. Additionally to heterogeneities, crack branching may be a result of crack propagation at their terminal velocities [212]. Hoagland et al. investigated the impact of rock microstructure on fracture propagation in sandstone; they found evidence of microcrack arrays near the tip of a propagating crack (process zone) [87]. Kranz investigated the interaction of propagating fractures with crystal grains in granite and other fractures [103]. He discovered that fracture propagation path in granite is highly influenced by the presence of heterogeneities and other fractures while the impact of the stresses applied to the sample was of lesser importance. Another experimental study reported that fractures in regions with relatively large pores propagate by linkage of nearest pores [149].

Propagation of open-mode fractures is highly affected by the presence of natural fractures. The interaction of an open-mode fracture with a natural fracture may result in an arrest, slippage, or branching of the former depending on the attack angle, fracture toughness, stress anisotropy, and mineral filling properties [77, 107]. Microseismic mapping also provides evidence for the geometry of field-scale hydraulic fractures [57, 202]. According to these findings in the Barnett shale, micro-

seismic events occur hundreds of feet apart from the expected planes of hydraulic fractures, which in turn suggests fracture reactivation in shear and complex patterns of hydraulic fracture propagation at the reservoir scale ( $> 100$  m).

The advancement of computational sciences has allowed to model complex fracture geometries. Many of recently developed methods for fracture propagation are based on the displacement discontinuity method [39, 205]. Although capable of modeling the interaction of a growing open-mode fracture with a network of natural fractures, this method does not allow for heterogeneous distribution of material properties [133, 170, 123]. Modeling complex open-mode fractures within heterogeneous formations is possible with the most recent numerical methods, such as the Finite Element and Finite Volume methods coupled with the Cohesive Zone Model, the Extended/Generalized Finite Element methods, and Phase-Field methods [47, 211, 42, 176, 80, 110]. Peridynamics uses non-local formulations and has been specifically developed to accurately model discontinuities [135]. The Discrete Element Method (DEM) uses independent elements and bonds that follow the Newton's laws; this method is able to replicate fracturing patterns in granular media [215, 187].

Most simulation studies place emphasis on fracture propagation in naturally fractured media, but pore-scale controls can also affect fracture propagation. Yang et al. used numerical simulation to investigate the propagation of hydraulic fractures in heterogeneous cylindrical rock samples [210]. Their findings indicate that inhomogeneities significantly reduce borehole breakdown pressure and that fracture initiation occurs considerably earlier than the instant of breakdown in homogeneous

rocks. Kim et al. used DEM formulation coupled with cohesive softening model to simulate fracture propagation [99, 98]. The heterogeneity in their simulations was achieved by assigning variable bond strength, stiffness, and separation displacements on the particle contacts. The authors concluded that the maximum aggregate size in asphalt mixtures affects the hardening/softening material behavior. Ouchi et al. used numerical simulations based on peridynamics to study microscale fracture propagation in multi-mineral shale samples [135]. The results show that the fracture propagation path is highly influenced by the mineral distribution with distinct elastic mechanical properties.

In this study we investigate open-mode fracture propagation in heterogeneous porous media at the pore-scale. First, the paper presents the results of semicircular-bending experiments on carbonate rock samples subjected to acidizing with hydrochloric acid solutions. We use X-ray microtomography and image processing to illustrate how mineral dissolution, and therefore presence of highly-porous regions affects fracture initiation and propagation. Then, we use a numerical model based on phase-field approach in order to elucidate and match the influence of pore scale mechanical properties on fracture propagation. Finally, we propose a coupling procedure to connect reactive transport in porous media and fracture propagation based on changes in porosity.

## 4.2 Experimental determination of fracturing behavior

In this section we present the experimental results of semicircular bending (SCB) experiments conducted on limestone rock samples subjected to hydrochloric

acid (HCl) injection. In addition we provide pore structure characterization and evidence of fracture geometry through X-ray microtomography and image analysis.

#### 4.2.1 Methods

##### 4.2.1.1 Rock samples

We conducted acidizing and mechanical experiments using Indiana limestone samples from outcrops. Two samples were cored to 3.81 cm in diameter and 7.62 cm in length. The average (total) porosity of both samples was 18% as calculated from the sample mass and assuming the matrix density of calcite 2.71 g/cm<sup>3</sup>. The average permeability of the samples before acidizing was 150 mD.

##### 4.2.1.2 Acidizing procedure

The rocks cores were subjected to injection of 220 cm<sup>3</sup> and 440 cm<sup>3</sup> of 0.3M HCl acid solution within a Hassler core-holder to achieve porosity alterations. We performed acid floods in stages: approximately 100 cm<sup>3</sup> of acid solution was injected per stage. During each acid flood, the differential fluid pressure across the sample was equal to 0.35 MPa and the confining pressure was 1.38 MPa. The samples lost 1.5 % and 3 % of their mass during acidizing, respectively.

This experimental variables resulted in reactive fluid flow with Péclet number  $Pe \approx 4.6 \times 10^5$  and Damköler number  $Da \approx 77$ . This combination of dimensionless parameters is associated with dominant wormhole regime [72]. These dimensionless numbers were estimated from sample dimensions, flow rate, and assuming mass diffusion coefficient  $1 \times 10^{-5}$  cm<sup>2</sup>/s and constant reaction rate equal to 0.2 cm/s

[116, 3].

#### 4.2.1.3 Semicircular bending experiments

Semicircular bending (SCB) testing is one of the standard procedures to measure fracture toughness [10]. Similarly to three-point bending testing recommended for measuring fracture toughness in metals and alloys, SCB testing consists in loading a notched specimen until achieving tensile yield [134] Furthermore, the SCB testing procedure neglects the small-scale yielding effects measured with three-point-bending tests due to the brittle nature of the rocks. SCB differs, however, from three-point-bending by requiring semicircular specimen geometry and, thus, is more preferable in terms of sample preparation. After acidizing, the plugs were cut to semi-cylindrical shape with thickness 1.52 cm for the semicircular bending tests (total of 10 specimens per core). A notch of approximately 3.8 mm long was cut in each of the samples so that the ratio of the notch length  $a$  to the sample radius  $r$  approximated  $a/r = 0.2$ . We performed the SCB tests using a Humboldt MasterLoader HM-3000 load frame. The support rollers spacing was 17.75 mm. We measured the load  $P$  with a load cell located above the top roller and measured displacement between the moving bottom plate and top roller. Additional details on the SCB procedure can be found elsewhere [107].

The values of fracture toughness  $K_{IC}$  were obtained from the experimental loading curves using the following equation:

$$K_{IC} = \frac{P_{max} \sqrt{\pi a}}{2rt} Y_I \quad (4.1)$$

where  $P_{max}$  is the maximum load,  $r$  is the radius of the sample,  $a$  is the notch length,

$t$  is the sample thickness, and  $Y_I$  is a geometric constant which depends on the ratio of the notch length to the sample radius [14, 105].

#### 4.2.1.4 X-ray microtomography and image processing

X-ray micro-computed tomography ( $\mu$ CT) helps to identify the fracture geometry and to map the rock pore structure before and after mechanical testing. We scanned all rock samples before and after acid exposure with an X-ray microtomograph Nikon XTH 225. We used approximately 135 kV voltage and 288  $\mu$ A current at the tube with 250 ms exposure time and a 0.27 mm thick copper filter. The resulting voxel size of the images was approximately 30  $\mu$ m, which is sufficiently small to resolve large pores (diameter  $d > 60\mu\text{m}$ ) and estimate macro-porosity in the Indiana limestone samples (Fig. 4.1d).

We used reconstructed images to estimate local macro-porosity around the notch in order to correlate them with fracture toughness obtained from SCB tests. The procedure consists in: (1) binarizing the reconstructed  $\mu$ CT images to segment the rock matrix and pore space (1 for solid and 0 for voids) and (2) computing the average pixel value across an area near the tip notch to estimate local macro-porosity. We fixed the area to calculate local macro-porosity as a square with a side equal to the notch length ( $\approx 3.8$  mm). This choice is confirmed by the numerical simulations described later. In these simulations the tensile stress reduced 10 times across the area with the radius 80% of the notch length and 100 times within the area with the radius 125% of the notch length. The reconstructed  $\mu$ CT images are also inputs for numerical simulation as described in Section 4.3.1.

#### 4.2.2 Experimental results

Fig. 4.1 shows examples of  $\mu$ CT images of Indiana limestone samples after acidizing and fracturing. Fig. 4.1a shows a 3D projection of the porous wormhole due to acid injection in one of the Indiana limestone cores before cutting for SCB testing. In this image the cylindrical core is oriented vertically. The top part of the sample contains a higher volume of voids than the bottom part (acid injected from the top). The wormhole occupies only the top half of the sample indicating that acid breakthrough did not occur during the acid flood. This dissolution pattern allowed to obtain sample slices with a range of degree of acidizing and local macro-porosity values in the vicinity of the notch, which is the fracture initiation point.

Fig. 4.1b-d show  $\mu$ CT images of the semi-cylindrical slices cut from the full core and subjected to SCB testing (left) and processed images highlighting the fracture geometry (right). Fig. 4.1b shows a slice with a high amount of dissolved mineral. This slice was cut from the part of the core close to the injection point. The fracture in the image deviates from the vertical direction of propagation to pass through a lower-toughness region with dissolution-induced voids. Fig. 4.1c shows a  $\mu$ CT image of a fractured sample with a moderate amount of local dissolution. This slice belongs to the middle of the cylindrical plug in Fig. 4.1a. The fracture in the image turns right and connects large voids formed due to dissolution. Fig. 4.1d shows an  $\mu$ CT image of a sample slice with no significant evidence of mineral dissolution. This slice was taken from the bottom part of the sample in Fig. 4.1a. The fracture that formed during the test propagated by connecting large pores, i.e., weak regions of the rock. The presented images represent typical examples of observed

fracturing behavior in all tested samples (twenty).

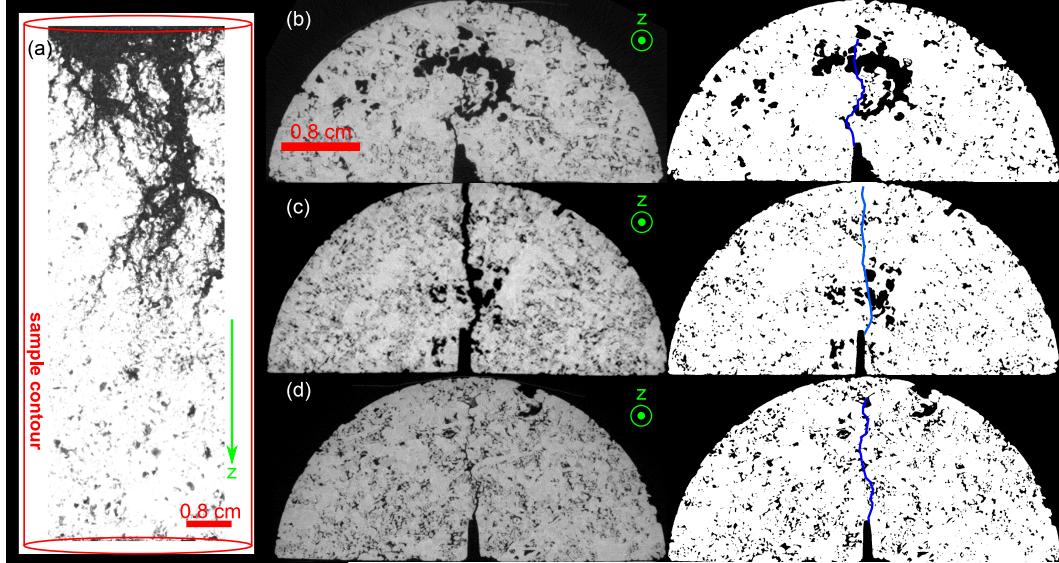


Figure 4.1:  $\mu$ CT images of Indiana Limestone sample subjected to acidizing and SCB testing. (a) Full core oriented vertically before cutting. Black color indicates the voids (wormhole), the rock matrix is transparent, the red rectangle shows the outer contour of the cylindrical sample. (b-d)  $\mu$ CT images of the horizontal slices after SCB testing (left) and processed images with fractures highlighted in blue: (b) high amount of dissolution end-member, (c) moderate amount of dissolution case, and (d) negligible amount of dissolution end-member.

Fig. 4.2 summarizes the results of all the experimental tests. Fig. 4.2a shows the load on the samples as a function of the displacement of the top rollers in the SCB experiments. The experimental results indicate variable rock stiffness and toughness in the tested samples. Lines shown with blue circles correspond to rock samples with high amounts of dissolution and have lower peak values than lines shown with red and green labels (samples with low-to-medium dissolution). Fig. 4.2b presents fracture toughness calculated from the SCB tests as a function of local macro-porosity obtained from  $\mu$ CT-image processing. Samples with high

local macro-porosity (20-40%) at the tip of the notch have low values of fracture toughness. Samples with low macro-porosity (4-10%) had higher values of fracture toughness than those with high porosity. The high variability of fracture toughness for the samples with low macro-porosity is due to rock heterogeneity and differing pore-solid structure near the fracture tip. Overall, Fig. 4.2 indicates a clear trend of decreasing fracture toughness with increasing porosity.

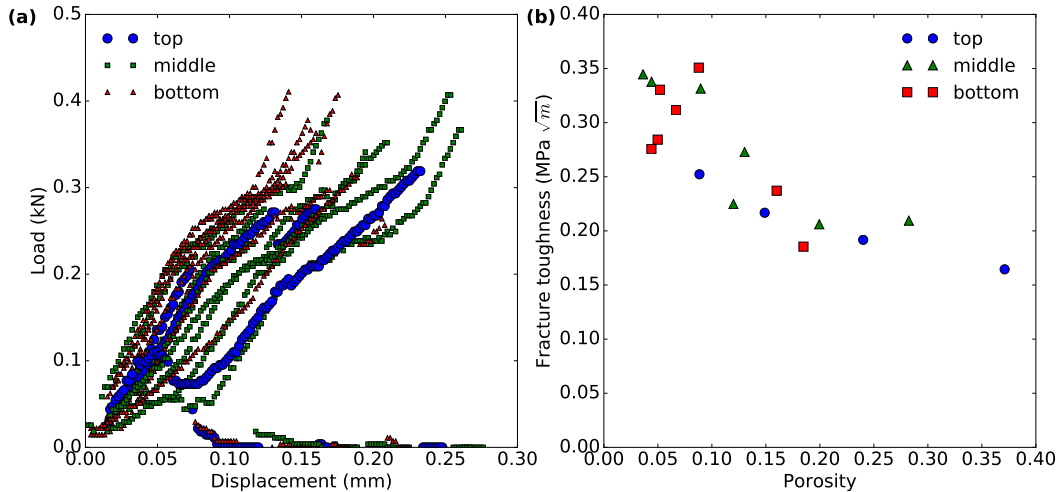


Figure 4.2: (a) SCB Experimental loading results: the load on the sample as a function of the top-roller displacement. (b) Fracture toughness obtained from SCB experiments as a function of rock macro-porosity from X-ray  $\mu$ CT image processing. The relationship indicates a clear trend of toughness reduction with an increase in porosity. Blue circles indicate slices taken from the “top” of the sample, which corresponds to the acid injection point. These samples feature high amounts of mineral dissolution (similar to the sample in Fig. 4.1b). Green squares indicate slices taken from the “middle” of the sample: they still contain the wormhole but are farther from the injection point than the samples shown with blue circles. Red squares indicate the slices taken from the “bottom” of the sample: they have negligible amounts of mineral dissolution.

## 4.3 Numerical modeling of fracture initiation and propagation

### 4.3.1 Phase-field method

The phase-field approach to fracture propagation modeling assumes a fracture as a diffusive region as opposed to a marked discontinuity [19, 126]. This assumption results in a subdivision of the porous medium domain into porous rock, fracture, and transition zones. The phase-field variable  $\varphi$  permits defining those regions as follows [19]:

$$\varphi = \begin{cases} 1 & \text{in intact rock} \\ 0 & \text{in fractures} \\ (0, 1) & \text{in transition zone} \end{cases} \quad (4.2)$$

The phase-field model treats fracture propagation in an elastic medium as an energy minimization problem. The overall energy of the system that contains an elastic material and a fracture can be written as:

$$E(\mathbf{u}, C) = \int_{\Omega_R} \frac{1}{2} \sigma(\mathbf{u}) : \varepsilon(\mathbf{u}) dV + \int_{\Omega} \left[ \frac{1}{2e} (1 - \varphi)^2 + \frac{e}{2} (\nabla \varphi)^2 \right] dV \quad (4.3)$$

where the first term to the right of the equal sign corresponds to the elastic energy of the rock and the second term is the surface energy of the fracture [20]. The parameters in Eq. 5.2 are: the problem domain  $\Omega$ , the porous rock subdomain  $\Omega_R$ , the stress tensor  $\sigma$ , the displacement vector  $\mathbf{u}$ , the rock strain tensor  $\varepsilon$ , and the fracture surface area  $H^{d-1}$ . The parameter  $G_c$  is the energy release rate and is related to fracture toughness as  $G_c = \frac{K_{IC}^2}{E'}$ , where  $E' = \frac{E}{1-\nu^2}$ ,  $E$  is the rock Young's modulus and  $\nu$  is the rock Poisson's ratio. The parameter  $e$  defines the width of the transition

zone  $\varphi = (0, 1)$ . We solve fracture propagation by minimizing the right-hand-side of Eq. 5.2 [85]. The problem is solved in two dimensions (plane-strain mechanics problem) but is readily applicable to three-dimensions. More details about solving this problem with the finite element methods and phase-field are available elsewhere [85].

#### 4.3.2 Material properties: Toughness mapping

We now present the workflow utilized to obtain material properties (fracture toughness) distribution for the numerical model. The objective of this workflow is to create average material properties of a porous medium -instead of identifying pore structure- so that the material properties can be used in reactive fluid flow equations for porous media. The workflow consists in the following steps:

1. Apply a binarization procedure to a raw 2D reconstructed tomographic image in order to obtain a segmented image that is later used to calculate porosity (Fig 4.3a). This procedure consists in separating the solid and large voids based on a gray-scale threshold value.
2. Apply a Gaussian blur filter (moving centered kernel) with a predetermined radius (10 pixels  $\sim 300 \mu\text{m}$  in this work) to the binary image to obtain a continuous macro-porosity map (Fig 4.3b). For this procedure we utilize Fiji software [165].
3. Select a toughness-porosity function applicable to the porous medium under study (Fig 4.3c).

4. Obtain the toughness distribution map for the simulation domain by calculating toughness with a toughness-porosity function and the porosity map. (Fig 4.3d).

We fit the experimental data described in Section 4.2.2 with a logarithmic curve (Fig 4.3c) to obtain a unique and continuous toughness map for Indiana limestone samples utilized in this study.

$$K_{IC} = -0.07432 \text{ [MPa } \sqrt{\text{m}}] \ln(\phi) + 0.0959 \text{ [MPa } \sqrt{\text{m}}] \quad (4.4)$$

where  $K_{IC}$  is fracture toughness measured in MPa  $\sqrt{\text{m}}$  and  $\phi$  is porosity ranging from 0 to 1. This logarithmic fit results in  $R^2 = 0.724$ . Eq. 4.4 results in non-zero toughness values at porosity  $\phi = 1$ , which, although not realistic, ensures stability of numerical simulations whenever the fracture encounters a pore. Additionally, we limit the toughness values obtained from Eq. 4.4 to the maximum value  $K_{IC \ max} = 0.45 \text{ MPa } \sqrt{\text{m}}$  in order to obtain a physically bounded toughness result.

A similar procedure can be used to obtain the distribution of other material properties, such as Young's modulus or Poisson's ratio, with suitable Young's modulus-porosity and Poisson's ratio relationships, e.g., [17, 38].

### 4.3.3 Phase-field fracture simulation results

#### 4.3.3.1 Homogeneous samples: fracture toughness from peak load in SCB experiments

We first show example simulations of a SCB experiments with homogeneous properties to demonstrate the impact of various simulation parameters on the

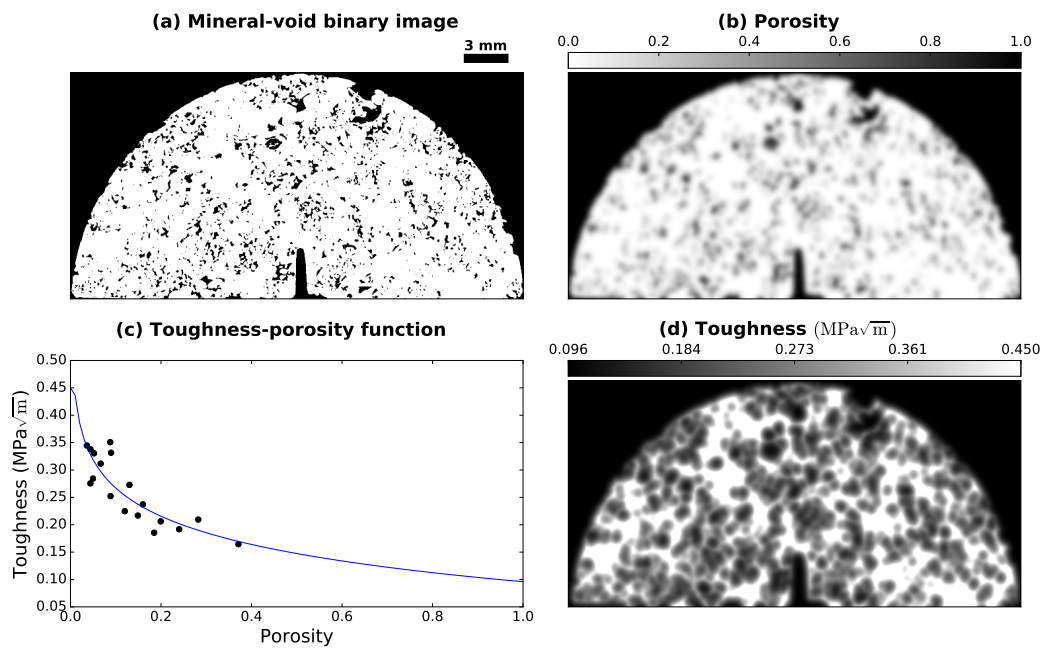


Figure 4.3: Image processing workflow for setting material property distribution for numerical simulation. (a) Mineral/void binary image obtained from  $\mu$ CT scan with a threshold value. (b) Porosity map obtained with a Gaussian blur filter. (c) Fitted toughness-porosity experimental data. (d) Toughness map.

SCB results. We fix the Poisson ratio in the following simulations to 0.14 [152] and vary all other parameters.

The simulation domain replicates the geometry of the rock samples used for SBC testing (Fig. 4.4): a semi-circle with radius 19 mm and a center notch on the bottom face. We use an ellipse with the major axis 2.54 mm and minor axis 1.52 mm to model the notch boundary. We specify point-displacement boundary conditions in the simulation with fixed vertical  $y$ -displacement components in two points equidistant from the circle center at the bottom of the sample. In one of these points we also fix  $x$ -displacement to assure stiffness matrix invertability. The top of the sample moves down at the rate of  $\dot{u}_y = -0.8 \mu\text{m/s}$ . The rest of the boundaries are free boundaries. Additional variables for these simulations are: the minimum element size of the original coarse mesh 2.23 mm, the number of adaptive refinement steps 5 resulting in the minimum mesh size  $h_{min} = 0.07 \text{ mm}$ , and the width of the diffusive zone  $e = 4h_{min}$ .

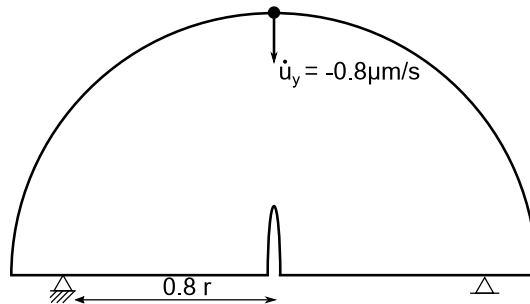


Figure 4.4: Schematics for the SCB numerical simulation. The point at the top of the sample moves down at a fixed displacement rate. The two points at the bottom equidistant from the notch have fixed  $y$ -displacement. Additionally, the left point at the bottom has fixed  $x$ -displacement.

Fig. 4.5 shows the results of a sensitivity study on an ideal sample with thickness 12.7 mm. Fig. 4.5a shows sensitivity of the loading curve to the fracture toughness  $K_{IC}$ . High values of fracture toughness cause higher values of the maximum load than those with low fracture toughness. Fig. 4.5b shows sensitivity of the loading curve to the rock Young's modulus  $E$ . High values of Young's modulus result in a steeper slope of the loading curve than lower values of Young's modulus. Therefore, stiff rocks feature steep slopes of the SCB loading curves, as expected. All simulated fractures in homogeneous media are straight and propagate vertically from the notch.

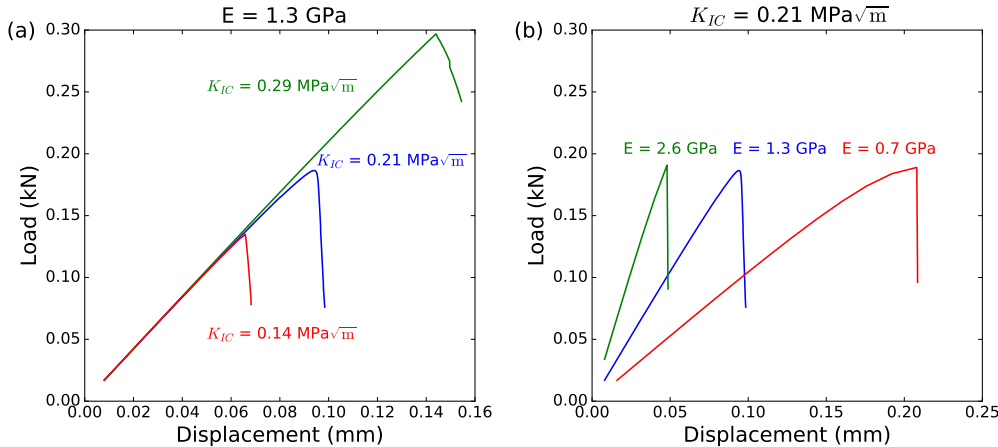


Figure 4.5: Sensitivity study SCB simulation. (a) Sensitivity to fracture toughness  $K_{IC}$ . High fracture toughness results in high values of the peak load. (b) Sensitivity to Young's modulus  $E$ . High Young's modulus values result in steep slope of the loading curve.

We now present the comparison of the loading curves obtained with numerical simulation with two SBC experiments described in Section 4.2 (Fig. 4.6). The domain geometry is chosen to represent a real rock sample in each simulation. For

the first sample (blue curve) we set a domain with radius 18.5 mm with and notch length 3.81 mm. The mesh size prior to refinement at the sample edge is 5.59 mm and it is 0.927 mm at the notch. We use two steps of adaptive refinement that result in the minimum mesh size  $23 \mu\text{m}$ . The value of Poisson's ratio  $\nu = 0.14$  was used in all simulations. Finally, since our numerical model is two-dimensional, we multiplied the sample load values by sample thickness 12.5 mm. We varied fracture toughness  $K_{IC}$  and Young's modulus  $E$  to fit the peak the load value and the slope of the loading curve observed in the experiment. The fitting resulted in the toughness values  $K_{IC} = 0.36 \text{ MPa} \sqrt{\text{m}}$ , which is within 6% of the experimental result  $K_{IC}^* = 0.34 \text{ MPa} \sqrt{\text{m}}$ , and the Young's modulus  $E = 1.3 \text{ GPa}$ . Notice that the matched bulk modulus lumps plastic deformation at the contact between rock and steel rollers and other compliances that it is not accounted for in elastic simulations.

The simulation parameters for the second sample (green curve) are as follows: sample radius = 18.7 mm, notch length = 5.1 mm and Poisson's ratio  $\nu = 0.14$ . The matched effective Young's modulus is  $E = 1.1 \text{ GPa}$  and fracture toughness  $K_{IC} = 0.25 \text{ MPa} \sqrt{\text{m}}$ , which is within 8% from the experimental value  $K_{IC}^* = 0.23 \text{ MPa} \sqrt{\text{m}}$ , sample thickness = 11.4 mm. Overall, the simulation results show good agreement with the experiments.

#### 4.3.3.2 Heterogeneous samples: fracture propagation

We now present a comparison of fracture propagation modeling in heterogeneous porous media with SCB experiments in limestone described in Section 4.2. In the following simulations we utilize  $\mu\text{CT}$  images processed according to the method

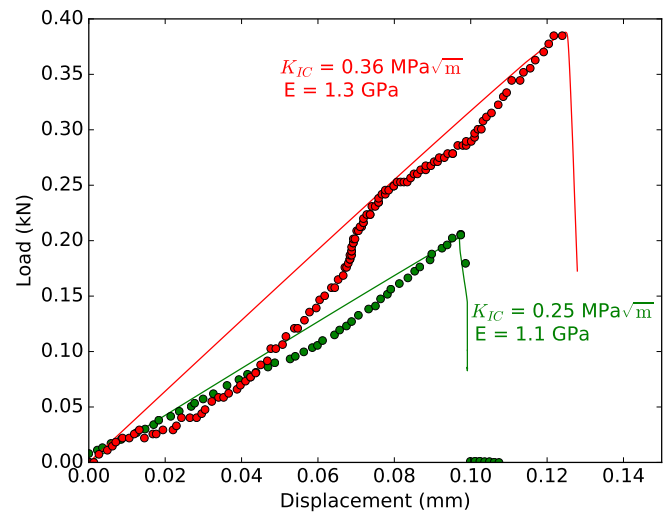


Figure 4.6: Comparison of two experimental SCB loading curves with numerical simulation. The fracture toughness values obtained from the experimental loading curves are  $K_{IC}^* = 0.34 \text{ MPa} \sqrt{\text{m}}$  and  $0.23 \text{ MPa} \sqrt{\text{m}}$  for the red and green lines, respectively.

described in Section 4.3.2 to generate toughness distribution in the domain. We assign other mechanical properties to be uniform in the domain: Young's modulus  $E = 1.1$  GPa and Poisson's ratio  $\nu = 0.14$ . We use the aforementioned value of Young's modulus as one that matches the loading curves. The domain is a semi-circle with the radius 19 mm and a notch at the bottom (Fig. 4.4) for each simulation. We varied notch length, width, and x-location to best represent the notch in the images. The mesh size in the domain ranged from  $63.5 \mu\text{m}$  to 3.8 mm with approximately 2,000 cells at the first time step to approximately 4,000 cells at the end of computation.

The comparison of fracture geometries obtained from numerical simulations with real fracture geometries observed by  $\mu\text{CT}$  scanning is shown in Fig. 4.7. Fig. 4.7a-c shows pairs of images with  $\mu\text{CT}$  scans on the left and simulation results on the right. The images corresponding to numerical simulations show fracture toughness distribution in the simulation domain with superimposed fracture geometries at the last time step (red zones). These fracture geometry curves are the regions with small values of the phase-field variable  $\varphi < 0.15$ .

Fig. 4.7a presents the comparison for a sample with a high amount of dissolution. The fracture initiated at a point located about 1 mm to the east from the top of the notch. The fracture propagated in the north-north-west direction from the tip and encountered the closest etched region. Then the fracture twisted and propagated until hitting the large interconnected etched area. These fracture segments are accurately represented by the numerical simulation for about 5.5 mm from the tip. Beyond this point within the interconnected etched area the fracture manifested

rather complex behavior propagating by connecting closest etched regions within the etched area preserving the propagation trend in the north direction. The fracture geometry in the numerical simulation replicates the direction trend while ignoring microscopic twists, for they are smeared by the image processing method.

Fig. 4.7b compares fracture geometry obtained from numerical simulation with a fracture in the  $\mu$ CT image of a sample with a moderate amount of dissolution. The fracture initiated approximately 1 mm to the east from the tip of the notch. The fracture then propagated in the north-east direction to the two nearest small etched regions and turns to the north encountering a large dissolved area (3 mm north-east from the tip of the notch). This fracture segment is well-replicated by the numerical model. Within the significantly etched area, the fracture propagates in the north-north-east direction, whereas the numerical simulation yields the fracture segment propagating in the north. This deviation is likely to be caused by 3D pore structure of the rock, which our 2D model cannot capture. After passing through the area, the fracture propagates to the north in both the experiment and simulation.

Fig. 4.7c shows the comparison for the rock sample with a negligible amount of dissolution. The fracture initiated at approximately 0.5 mm to the east from the notch tip. The fracture first propagated in the north-north-east direction, then smoothly diverted in the north-north-west direction, then retreated into propagation in the north-north-eastern direction, and finally propagated vertically. The entire fracture geometry in this case is well-replicated by the numerical simulation.

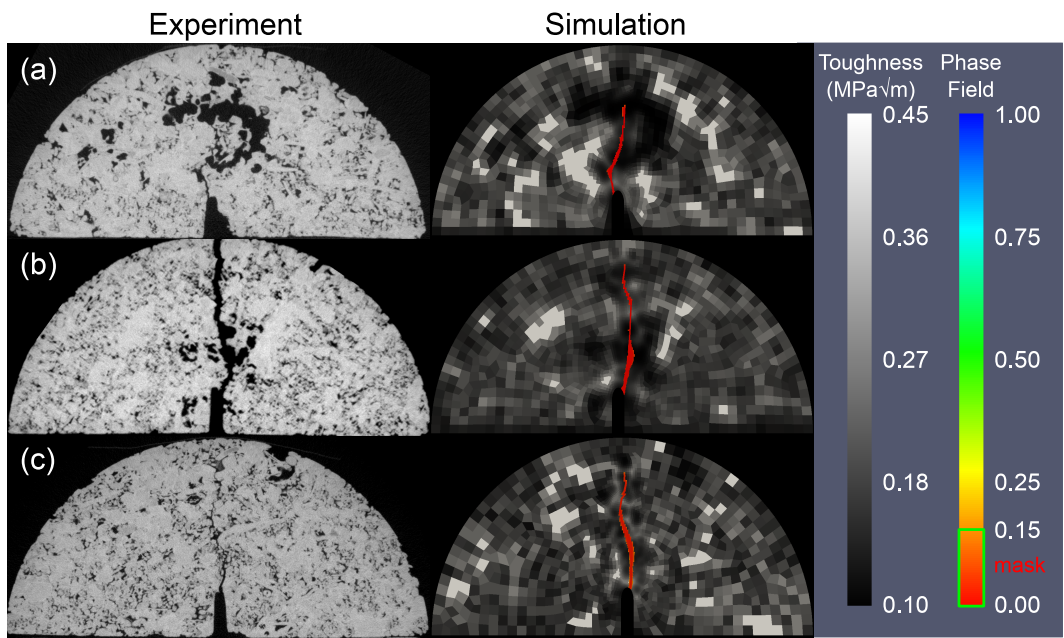


Figure 4.7: Comparison of fracture propagation in a SCB experiments with numerical simulations in heterogeneous media:  $\mu$ CT image of the fracture in the laboratory experiment (left) and fracture path ( $\varphi < 0.15$  shown in red) obtained from numerical simulation superimposed on the numerical model based on the  $\mu$ CT image (right). (a) Sample with a high amount of dissolution. (c) Sample with a moderate amount of dissolution. (d) Sample with a negligible amount of dissolution.

## 4.4 Discussion

### 4.4.1 The impact of the toughness-porosity relation on fracture propagation

In this section we explore the sensitivity of fracture geometry after SCB-testing to the fracture toughness-porosity relation. We primarily focus on the shape of the function  $K_{IC} = K_{IC}(\phi)$ , in order to ascertain the validity of the relationship obtained from the experiment. We computed four simulation cases, which are summarized in Fig. 4.8b:

- **Case I.** A case with fracture toughness distributed according to Eq. 4.4 (green line Fig. 4.8b). This case is the same as shown in Fig. 4.7c.
- **Case II.** A case with fracture toughness  $K_{IC}$  obtained from porosity with a linear function (red line in Fig. 4.8b):

$$K_{IC} = 0.45 \left[ \text{MPa} \sqrt{\text{m}} \right] - 0.35\phi \left[ \text{MPa} \sqrt{\text{m}} \right] \quad (4.5)$$

- **Case III.** A case with fracture toughness  $K_{IC}$  obtained from porosity with a convex-down fourth-order function (shown in red in Fig. 4.8b):

$$K_{IC} = 0.45 \left[ \text{MPa} \sqrt{\text{m}} \right] - 0.35\phi^4 \left[ \text{MPa} \sqrt{\text{m}} \right] \quad (4.6)$$

- **Case IV.** A case with fracture toughness  $K_{IC} = 0.45 \text{ MPa} \sqrt{\text{m}}$  distributed uniformly (shown with the black line in (b)).

All other simulation parameters and the computational domain are the same as listed in Section 4.3.3.2.

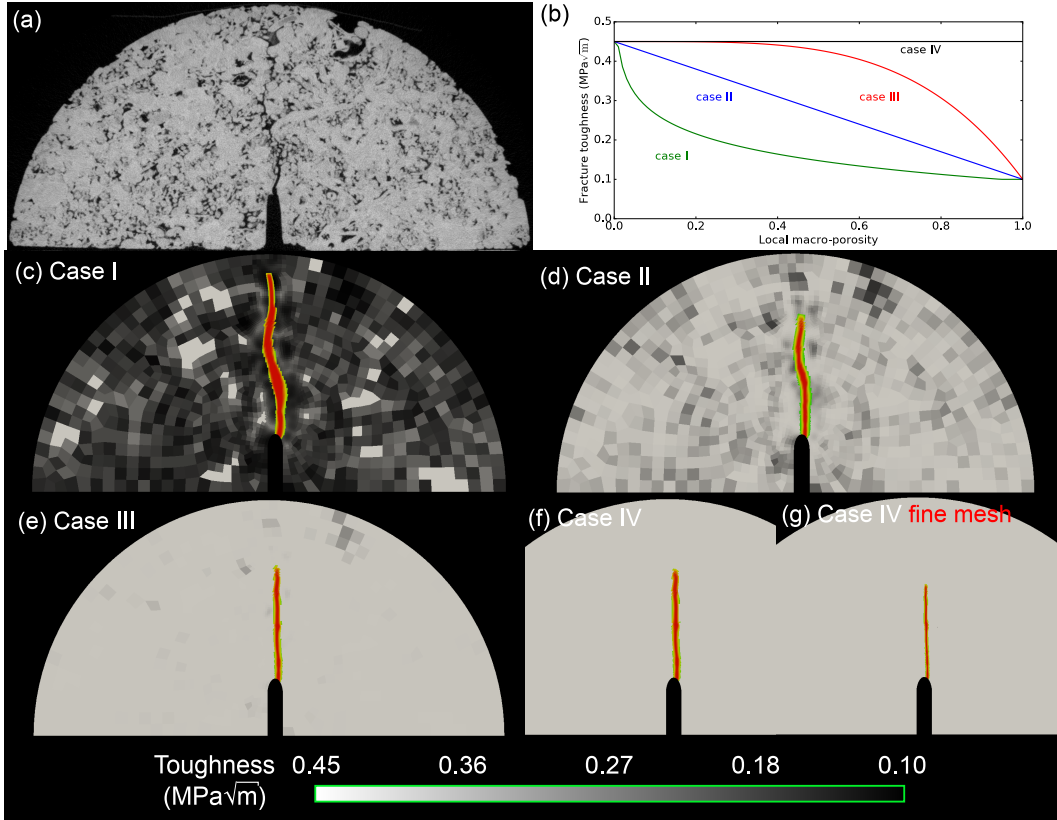


Figure 4.8: The impact of the toughness-porosity relation on fracture propagation. (a) A  $\mu$ CT image of a fractured rock sample with low amount of dissolution. (b) Toughness-porosity functions used to obtain the distribution of fracture toughness  $K_{JC}$  for numerical simulations. (c-g) The results of numerical simulations with various toughness distributions as input. (c) Case I. Fracture toughness is obtained with a concave-up relation that fits the experimental data. Numerical simulation matches well the experimental data. (d) Case II. Fracture toughness depends linearly on local macro-porosity. The fracture geometry is similar to that in case I but deviates more from the experimentally-observed fracture. (e) Case III. Fracture toughness is a concave-down function of porosity. The fracture geometry is nearly-planar due to nearly-homogeneous toughness distribution in the domain. (f-g) Case IV. Fracture toughness is distributed uniformly within the sample. The fracture is nearly-planar in (f) and is planar in (g) computed on a twice-finer mesh.

The comparison of the fracture geometries observed in numerical simulations and an experiment is shown in Fig. 4.8. The fracture in case II (Fig. 4.8d) is similar to that in case I (Fig. 4.8c) and the experiment (Fig. 4.8a). The deviation from the propagation in the upward direction, however, occurs farther from the notch in case II than in case I and the experiment. The fracture in case III propagates vertically due to the nearly-uniform distribution of fracture toughness in the domain(Fig. 4.8e). Case IV with uniform fracture toughness, similarly to case III, results in a planar vertical fracture.

#### 4.4.2 Fracture propagation with heterogeneous maps of Young's modulus and fracture toughness

In the previous section we presented the numerical results obtained assuming a heterogeneity in only the fracture toughness  $K_{IC}$ . In fact, stress intensification can also result from the presence of voids (pores and fractures) and heterogeneity of elastic properties. At the porous media scale, porosity also affects other mechanical parameters, such as Young's modulus and Poisson's ratio [81, 17, 22]. We now present the results of numerical simulations that illustrate the impact of heterogeneities at the porous medium scale in Young's modulus  $E$  and fracture toughness  $K_{IC}$ .

In order to obtain the map Young's modulus, we utilized the experimental data of elastic properties of limestone as a function of porosity [38] (Fig. 4.9). We fit these data with the following equation:

$$E = \frac{20.69}{\sqrt{\phi}} \text{ [GPa]} - 25.36 \text{ [GPa]} \quad (4.7)$$

which results in the  $R^2 = 0.78$ . Furthermore, we limited the minimum and maximum values of Young's modulus to 1 and 65 GPa, respectively, in order to stabilize the numerical model.

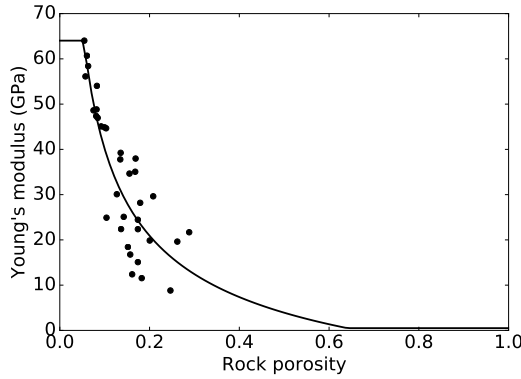


Figure 4.9: Correlation of Young's modulus with limestone porosity used in the numerical simulations (after [38]).

In order to determine the impact of stiffness heterogeneity and toughness heterogeneity separately, we computed three simulation cases: (1) a case with constant Young's modulus  $E = 1.1$  GPa and fracture toughness distributed according to Eq. 4.4 (same case as shown in Fig. 4.7b); (2) a case with constant fracture toughness  $K_{IC} = 0.45$  MPa  $\sqrt{m}$  and heterogeneous Young's modulus distributed according to Eq. 4.7; (3) a case with heterogeneous Young's modulus  $E$  and fracture toughness  $K_{IC}$ . The comparison of fracture paths obtained from the numerical simulations with an experimental CT image is shown in Fig. 4.10.

- In the first simulation (case 1) the fracture propagates through the centers of the high-porosity regions (Fig 4.10b). As discussed in Section 4.3.3.2, the numerical simulation replicates well the experimental fracture path from the

1 mm to the east from the notch tip to the north-east toward the large dissolved area located 3 mm north-east from the notch tip. The fracture in the numerical simulation then deviates from the fracture in the experiment propagating to the north due to the 3D rock pore structure.

- In the case (2) of homogeneous fracture toughness  $K_{IC}$  and heterogeneous Young's modulus  $E$ , the fracture in the numerical simulation does not propagate through the middle of the high-porosity regions (Fig 4.10c). This behavior is due to the fact that the Young's modulus is low in the high-porosity region, which results in high stress intensities around them (similar to cavities). Moreover, the fracture in the case (2) propagates almost vertically and does not follow the fracture path observed experimentally.
- The case (3) with homogeneous distributions of both Young's modulus  $E$  and fracture toughness  $K_{IC}$  results in the fracture geometry very similar to that obtained in case (1) and the experimental fracture geometry. The notable difference between the cases (1) and (3), however, is that the fracture in the latter (Fig 4.10d) case does not propagate though the centers of high-porosity regions, which is observed in some experiments. Overall, cases (1) and (3) result in fracture propagation patterns that compare well with experimental observations. Rigorously, case (3) should be the option to choose for fully-coupled geomechanical modeling in heterogeneous porous media, yet case (2) yields results that still match well experimental data.

The fracture paths in cases (2) and (3) are very sensitive to the Young's

modulus values at high porosities  $\phi > 0.5$ . We suggest that more experimental data need to be collected for rock samples with high porosities in order to accurately model fracture propagation in heterogeneous media significantly altered by mineral dissolution.

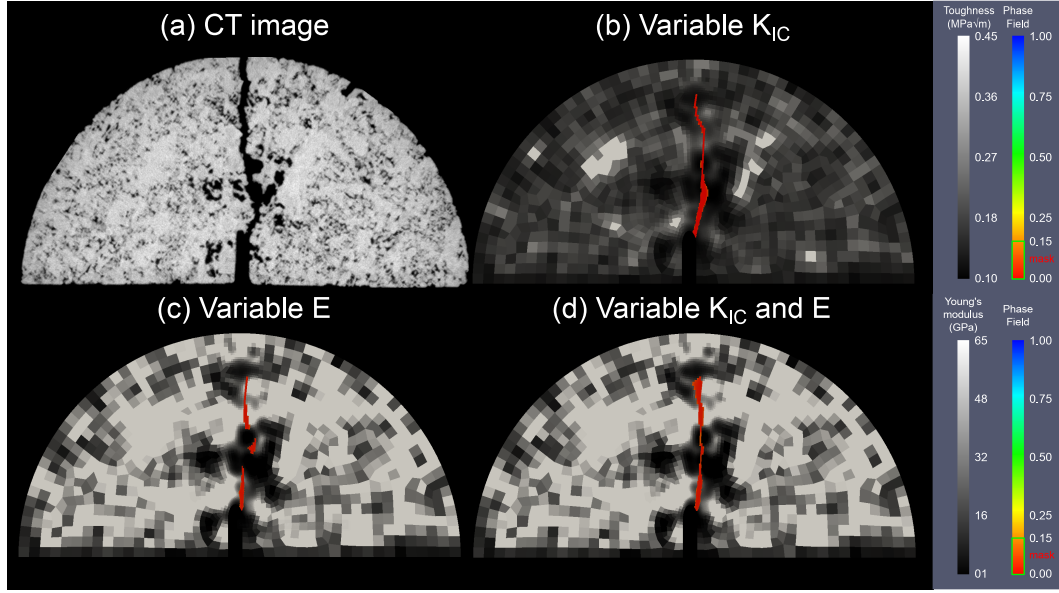


Figure 4.10: Comparison of fracture propagation in a SCB experiments with numerical simulations in heterogeneous media: the effect of heterogeneous distribution of fracture toughness  $K_{IC}$  and Young's modulus  $E$ . (a)  $\mu$ CT image of a SCB sample with a moderate amount of dissolution. (b-d) The results of numerical simulations with heterogeneous material properties. Fracture path ( $\varphi < 0.15$ ) obtained from numerical simulation is superimposed on the distribution of (b) fracture toughness and (c-d) Young's modulus in the domain. (b) Variable fracture toughness  $K_{IC}$  only: the simulation repeats the experimental fracture path. (c) Variable Young's modulus  $E$  only: the fracture avoids high-porosity regions. (d) Variable fracture toughness  $K_{IC}$  and Young's modulus  $E$ : the simulation repeats the experimental fracture path.

#### 4.4.3 Extension to reactive fluid flow models coupled with geomechanics

The objective of this study is to validate a coupling strategy for fluid flow in reactive porous media and geomechanics with particular emphasis on modeling of fluid-driven open-mode fracture propagation. We propose porosity as the coupling variable that is updated by the reactive fluid flow model and used iteratively in a geomechanics solver. The main assumption is that there is a unique relationship between porosity and mechanical properties, such as, Young's modulus and fracture toughness. Such assumption is inherently limited to simple cases and matrix supported porous structures, but nonetheless, useful to establish a connection between mineral dissolution and precipitation and mechanical property changes.

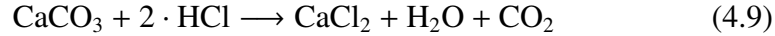
The following equations summarize the problem to be solved:

1. **Fluid flow in porous media.** Let us assume Darcy fluid flow of slightly compressible fluid (single phase) in a poroelastic solid [34])

$$\frac{1}{M} \frac{\partial p}{\partial t} + \alpha \frac{\partial(\nabla \cdot \mathbf{u})}{\partial t} - \nabla \cdot \frac{k}{\mu} (\nabla p - \rho \mathbf{g}) = q \quad (4.8)$$

where the unknowns to be solved are fluid pressure  $p$  and displacement  $\mathbf{u}$  as functions of time  $t$  and coordinate  $\mathbf{x}$ , with Biot modulus  $M = [(\alpha - \phi)/K_s + \phi/K_f]^{-1}$  ( $K_s$ : Unjacketed bulk modulus,  $K_f$ : Bulk modulus of the fluid), Biot coefficient  $\alpha$ , permeability  $k$ , viscosity  $\mu$  and fluid mass density  $\rho$ . Gravity  $\mathbf{g}$  and source term  $q$  complete the equation. Porous medium material properties  $M$ ,  $\alpha$ , and  $k$  are related to porosity  $\phi$  and pore structure.

**2. Reactive fluid flow.** Let us assume the calcium carbonate system with hydrochloric acid such that the reaction involved is



The transport of HCl concentration (single component) in the fluid phase  $C_f$  is dictated by the advection-dispersion equation [141, 2]:

$$\phi \frac{\partial C_f}{\partial t} + \nabla \cdot (\mathbf{v} C_f - D \nabla C_f) = q C_f^{inj} - k_c a_v (C_f - C_s) \quad (4.10)$$

where  $C_s$  is the HCl concentration at the fluid-solid interface,  $C_f^{inj}$  is the injected HCl concentration,  $D$  is the effective dispersion coefficient in the porous medium,  $k_c$  is the local mass transfer coefficient,  $a_v$  is the area of the reaction interface per unit volume, and  $q$  is the source terms that correspond fluid injection or production. The change in porosity caused by mineral dissolution or precipitation is

$$\frac{\partial \phi}{\partial t} = \frac{R(C_s) a_v \alpha}{\rho_s} \quad (4.11)$$

where the kinetics equation for the first order reaction may be simplified to  $R(C) = k_s C_s$  with  $k_s$  being the dissolution rate constant. This simplification results in the expression for the concentration at fluid-solid interface  $C_s = \frac{C_f}{1+k_s/k_c}$ .

**3. Geomechanics** Let us assume a linear poroelastic solid subjected to total stress tensor  $\mathbf{S}$  and pore pressure  $p$ , then the resulting strain tensor  $\boldsymbol{\varepsilon}$  is

$$\boldsymbol{\varepsilon} = \mathbf{D}(\mathbf{S} - \alpha p \mathbf{I}) \quad (4.12)$$

where  $\mathbf{D}$  is the compliance matrix and  $\alpha$  is the Biot coefficient, both a function of porosity  $\phi$ . Stresses are in equilibrium according to Cauchy's equation  $\nabla \cdot \mathbf{S} + \rho_b \mathbf{g} = 0$ . We assume fracture propagation happens when the stress intensity factor surpasses fracture toughness  $K_I \geq K_{IC}(\phi)$  (Eq. 4.4).

In all these equations porosity  $\phi$  plays a key role in defining material properties. Additional pore-structure functions to be determined as a function of porosity are (1) absolute permeability as a function of porosity, and (2) elastic properties and Biot coefficient as a function of porosity. There are several options for solving this system of equations and many models to couple the porous media equations to an evolving fluid-driven open-mode fracture. This solution is outside the scope of this communication and will be addressed in Chapter 5.

#### 4.4.4 Comparison with previous work, other methods and fluid-driven modeling approaches

**Previous work and alternative methods.** Previous work has already explored the role of heterogeneity in fracture propagation. Yang et al. used a numerical model to investigate the role of fracture toughness heterogeneity on fracture propagation from circular cavities [210]. Their study, however, did not contain any

comparison of the numerical simulation with laboratory experiments. Additionally, they used a linear elastic formulation with low values of Young's modulus to model fractures. Our work for first time links heterogeneity of mechanical properties due to mineral dissolution with open-mode fracture propagation.

Discrete element methods can also model open mode fractures in heterogeneous media. Kim et al. assumed variable bond forces, stiffness, and separation displacements on the particle contacts to model grain-scale heterogeneities in asphalt concrete with a DEM model [99, 98]. This is a fundamentally different approach, however, and applies to granular cemented media rather than matrix supported rock. Ouchi assigned various elastic parameters and fracture toughness to model pore-scale fracture propagation in multi-material media (clay, calcite, and quartz) [135]. Fracture branching and non-planar propagation ensues from mismatch of elastic properties in the heterogeneous medium. None of the aforementioned studies accounted for the effect of porosity and mineral dissolution on fracture propagation.

**Porous media vs. pore scale model.** We chose to obtain averaged properties that lump pores and solids into an effective medium. This option follows the premise of solving porous media physics and corresponding equations. However, in that assumption we ignore the fundamental phenomena that affect stress intensity distribution around pores and microcracks. The concentration of stresses around pores is what really causes fracture tilt, twist, and linkage between pores [103, 149]. Peridynamics simulations are able to perform this task [135]. On the other hand, Lattice Boltzmann methods may better capture reactive fluid flow in 3D porous structures [46, 193].

**Viscosity- vs. toughness-dominated fracture propagation.** Our study does not address phenomena derived from fluid-driven fractures and stress anisotropy. These are key phenomena that affect open-mode fracture propagation regimes and geometry in the subsurface. For example long and thin hydraulic fractures propagate with energy spent mostly in fluid flow in the fracture rather than in creating new rock surface, a regime known as “viscosity-dominated” fracture propagation [44, 24]. Hence, the actual value of fracture toughness is often irrelevant to propagation of long and planar fluid-driven fractures. The role of fracture toughness increases as the fracture tip length increases (e.g., penny-shaped fracture), fracture geometry becomes more complex (fracture branches with multiple propagating tips), and as fractures become shorter and fluid viscosity decreases. The regime in which the work spent in rock splitting is much larger than the work spent in fluid movement is known as “toughness dominated” fracture propagation and is the regime at which mineral dissolution can play a role in facilitating fracture propagation.

#### 4.4.5 Implications to natural and engineering geosystems

Reactive fluid flow in porous media coupled with geomechanics has important implications in subsurface natural and engineering processes. For example, advective flow through highly soluble rocks can enhance the creation of underground caverns. Evaporite and carbonate rocks react relatively fast when exposed to unsaturated or acid solutions compared to other mineral phases. If soluble formations are shallow, mechanically unstable caverns may collapse creating a sinkhole on the surface [200]. Sinkholes can also form as a result of brine leaks around wellbore

casing through evaporite formations [121]. Hydraulic fracturing technologies also employ acids in carbonate formations [171]. The objective in most of these applications is to etch fracture surfaces to improve fracture transmissivity. Acid fracturing may be also used for stimulating tight formations. In addition to improvements in fracture transmissivity [208], acid injection could also cause changes of local stress [179]. Furthermore, based on the findings of this study we hypothesize that stalled fractures may propagate aided by reductions of toughness at the tip - induced by mineral dissolution. Such phenomenon could increase fracture branching and complexity because short fracture branches tend to be toughness-dominated. The injection of CO<sub>2</sub> into geological formations can also trigger reactive fluid flow processes. Dissolution of carbonate mineral phases and alteration of clay fabric are among the most rapid alterations induced by CO<sub>2</sub>-acidified brine [29, 156, 153, 7]. Dissolution of minerals and weakening of the rock matrix by CO<sub>2</sub> can assist the propagation of microfractures and subcritical fractures [118].

## 4.5 Conclusions

This study validates the use of a “toughness-porosity” function with the objective of coupling reactive fluid flow and geomechanics in porous media. The experimental and modeling results permit arriving to the following conclusions:

- Open-mode fractures from semicircular bending experiments in acidized limestone samples exhibit non-planar geometry and follow high porosity regions and large pores.

- Fracture toughness correlates well with local macro-porosity. Our results in limestone suggest a rapid toughness decrease at low porosities and a more gradual decrease at larger porosities.
- Phase-field numerical simulations using heterogeneous maps of fracture toughness and Young's modulus validate a direct relationship between fracture toughness and porosity that permits replicating fracture stress intensity at initiation and non-planar propagation patterns observed in experiments.
- A link between reactive fluid flow, poro-elasticity, and fracture propagation is possible through the variable porosity and associated constitutive relations: toughness vs. porosity, elastic properties vs. porosity, and permeability vs. porosity.
- The proposed coupling solution is a first order approximation for reactive fluid flow applications in sinkhole development, hydraulic fracturing, and carbon geological storage.

# **Chapter 5**

## **Propagation of toughness-dominated fluid-driven fractures in reactive porous media**

### **5.1 Introduction**

Hydraulic fracturing completion consists in propagating fluid-driven fractures in hydrocarbon-bearing rocks. It is used to improve the productivity of oil and gas reservoirs and has played a decisive role in increasing oil and gas production in the USA, principally from organic-rich shale reservoirs [147]. Due to extremely low permeability, shale reservoirs require special treatments such as slick-water hydraulic fracturing [222]. Many shale reservoirs accommodate a significant amount of carbonates, minerals that can be easily dissolved in acid solutions [65, 208]. The solubility of carbonates suggests acid hydraulic fracturing as an enhanced stimulation technology.

Fluid-driven fractures propagate when the pressure of fracture-filling fluids overcomes the confining stress, viscosity losses, and fracture surface creation work. The first attempts to characterize propagation of fluid-driven fractures assumed the fractured media to be a linear elastic non-porous isotropic solid [216, 143, 69]. Fluid-driven fracture propagation in non-porous solids is a fluid transport-mechanical coupled process. Fracture propagation is controlled by friction losses

characterized by fluid viscosity and work spent on creation of new solid surfaces characterized by fracture toughness [44]. Canonical models for fluid-driven fracture assume various fracture geometries: (1) radial (or penny-shaped) fractures have elliptical vertical cross-section and their tips lie on circles (Fig. 5.1); (2) PKN fractures also have elliptical vertical cross-section but their height is constant limited by the bounding layers; and (3) KGD fractures, have constant height but feature rectangular vertical cross-sections (Fig. 5.1). Additionally to the geometrical characteristics, fluid-driven fractures can be classified by the ratio of work spent on splitting the rock to the fluid friction losses in the fracture [44]. Fracture propagation that manifests the dominance of friction losses over work spent on rock splitting is called viscosity-dominated. Viscosity-dominated propagation occurs in long fractures with medium-high viscosity fluids. Fracture propagation in which the work required to fail the rock in tension is higher than the work to move the fluids is called toughness-dominated. Relatively short fractures and low-viscosity fluids in high-toughness rocks favor toughness-dominated fracture propagation.

Fluid-driven fractures in porous media are affected by fluid leak-off, that is, fluid flow from fractures to the fractured porous medium. Leak-off results in additional viscous losses and fluid storage in the rock pore space. The earliest attempts to describe propagation of fluid-driven fractures with leak-off apply Carter equation to the PKN and KGD solutions [89]. The resulting fracture propagation models are known as PKN-C and KGD-C models [199, 198]. Fractures with the most of injected fluid contained within the fracture are called storage-dominated fractures and occur in low-permeability rocks [24].. In contrast, in the case of leak-

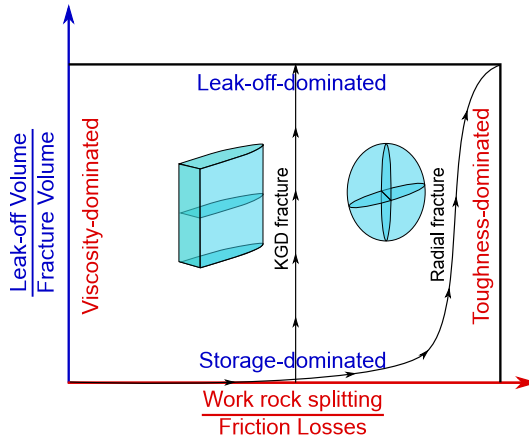


Figure 5.1: Regimes of fluid-driven fracture propagation. (after [24]).

off-dominated fractures, most of the injected fluid goes into the rock pore space. High-permeability reservoirs favor leak-off-dominated fractures. Although widely used, these models consider fluid leak-off only in the mass balance for the fluid in fracture but neglect the poromechanical effects of porous media deformation around the fracture and reduced effective stress near the fracture face.

Finite difference solutions for fracture propagation in poroelastic are available for simple geometries like PKN [45]. Under these conditions and assumptions, poroelastic effects result in an increased treatment pressure with negligible effects on fracture length and width. Simulating coupled poroelastic fracture propagation in more arbitrary geometries requires advanced numerical models. Various local (the extended finite element method, phase-field) and non-local (peridynamics) numerical methods were proposed to model fractures with non-prescribed geometries [218, 28, 119, 60, 136, 19, 127]. Poroelastic effects cause various phenomena that can significantly affect fracture propagation. Tensile stresses at the tips of fluid-

driven fractures result in reduced pore pressure [111]. Poroelastic effects also cause reduced effective stresses around fracture faces: accounting for these phenomena is important when calculating fracture width [26]. Additionally, poroelastic effects significantly influence on the interaction between fluid-driven and natural fractures at high values of leak-off [136].

Rock alterations imparted by chemical reactions can affect rock mechanical response. Likewise, mineral dissolution can affect fracture propagation in rocks. Acids flowing in porous media can dissolve minerals and enlarge pore throats causing localized increments of porosity and permeability. In the absence of large effective stresses, patterns of porosity variations induced by dissolution depend on competing advective and reactive processes captured in two dimensionless numbers [72, 124]: (a) the Damköler number  $\text{Da} = \frac{\kappa l}{v}$  which represents the ratio between advection and reaction times ( $\kappa$  is the reaction rate,  $l$  is a characteristic length, and  $v$  is fluid), and (b) the Péclet number  $\text{Pe} = \frac{vl}{D}$  which is the ratio between advection and diffusion time ( $D$  is the diffusion coefficient). A pioneering work by Atkinson shows the influence of chemical environment on subcritical fracture propagation (propagation with stress intensity lower than fracture toughness) [11]. Recent work shows that chemical alteration and mineral dissolution can impact directly into fracture toughness and subcritical fracture propagation characteristics [118, 178]. These studies, however, do not address reactive fluid flow explicitly in a propagating fracture and just account for the impact of chemical reactions phenomenologically.

The objective of this study is to investigate the propagation of fluid-driven fractures in reactive porous media. We use numerical simulation in order to explore

this coupled problem. The paper starts with a description of the equations involved, their numerical solution, and a validation of a phase-field formulation to model propagation of fluid-driven fractures in reactive porous media. Next, we show the results of numerical simulation for acid-induced propagation of stalled fractures and acid-driven propagation of toughness dominated fractures. The paper finishes with a discussion of the new physics observed, suggestions for experimental validation, and potential engineering and geoscience applications.

## 5.2 A coupled phase-field model for fluid-driven fractures in reactive poroelastic media

In this section, we outline the main equations of the phase-field formulation used to model fracture propagation. The phase-field method is based on the finite element method and handles sharp discontinuities in the solution domain by introducing a smooth diffusive zone [19, 127]. In the context of fracture propagation problems, the phase-field variable  $\varphi$  permits defining the reservoir domain (intact rock), fracture domain, and the transition zone [126]. The phase-field variable takes values between zero and one and indicates whether a point is inside a fracture, in the intact rock, or in a transition zone as follows:

$$\varphi = \begin{cases} 1 & \text{in intact rock} \\ 0 & \text{in fractures} \\ (0, 1) & \text{in transition zone} \end{cases} \quad (5.1)$$

### 5.2.1 Mechanics formulation

The energy of a poroelastic medium  $\Omega_R$  with a fracture  $C$  is described with the Francfort-Marigo functional [61]:

$$E(\mathbf{u}, C) = \int_{\Omega_R} \frac{1}{2} \sigma(\mathbf{u}) : \varepsilon(\mathbf{u}) dV - \int_{\Omega_R} \alpha p \nabla \cdot \mathbf{u} dV + G_c H^{d-1}(C) \quad (5.2)$$

where  $\sigma$  is the effective stress tensor,  $\varepsilon$  is the strain tensor,  $\alpha$  is the Biot coefficient,  $p$  is pore pressure, and  $\mathbf{u}$  is a displacement vector. The first term of Eq. 5.2 is the energy from elastic strain  $\varepsilon(\mathbf{u})$ , and the second term corresponds to creation of new surfaces at the Griffith energy release limit. The parameter  $G_c$  represents the energy release rate and relates to fracture toughness  $K_{IC}$  through  $G_c = \frac{K_{IC}^2}{E} (1 - \nu^2)$  ( $E$ : Young's modulus,  $\nu$ : Poisson's ratio). The term  $H^{d-1}(C)$  is the surface area of the fracture and can be approximated as

$$H^{d-1}(C) = \int_{\Omega} \left[ \frac{1}{2e} (1 - \varphi)^2 + \frac{e}{2} (\nabla \varphi)^2 \right] dV \quad (5.3)$$

where  $e$  is the width of the transition zone  $\varphi = (0, 1)$ . Following [107], we use the phase-field variable to extend Eq. 5.2 to the global domain  $\Omega = \Omega_R \cup C$ . We further apply the divergence theorem to the surface force integral and assume pressure continuity at  $C$ . The resulting energy functional reads

$$\begin{aligned} E_\varepsilon(\mathbf{u}, p, \varphi) &= \int_{\Omega} \frac{1}{2} [(1 - k)\varphi^2 + k] \sigma^+(\mathbf{u}) : \varepsilon(\mathbf{u}) dV + \int_{\Omega} \frac{1}{2} \sigma^-(\mathbf{u}) : \varepsilon(\mathbf{u}) dV \\ &\quad - \int_{\Omega} (\alpha - 1) \varphi^2 p \nabla \cdot \mathbf{u} dV + \int_{\Omega} (\varphi^2 \nabla p) \cdot \mathbf{u} dV \\ &\quad + G_c \int_{\Omega} \left[ \frac{1}{2e} (1 - \varphi)^2 + \frac{e}{2} (\nabla \varphi)^2 \right] dV \end{aligned} \quad (5.4)$$

We decompose the stress tensor  $\sigma(\mathbf{u})$  into compressive  $\sigma^-(\mathbf{u})$  and tensile  $\sigma^+(\mathbf{u})$  parts in order to enforce fracture propagation only under tension (open-mode). The details of stress decomposition can be found elsewhere [85].

### 5.2.2 Fluid mass balance and flow

**Flow in porous media.** Our formulation assumes Darcy flow of a slightly compressible fluid in a poroelastic solid in order to describe flow in porous media. Under these assumptions, the following equation is valid [34]:

$$\frac{1}{M} \frac{\partial p_R}{\partial t} + \alpha \frac{\partial(\nabla \cdot \mathbf{u})}{\partial t} - \nabla \cdot \frac{k_R}{\mu} (\nabla p_R - \rho_f \mathbf{g}) = q_R \quad (5.5)$$

where  $p_R$  is the reservoir pressure,  $\alpha$  is the Biot coefficient,  $\mathbf{u}$  is the rock deformation,  $k_R$  is the reservoir permeability,  $\mu$  is the fluid viscosity,  $\rho_f$  is the reservoir fluid density,  $\mathbf{g}$  is the gravity acceleration,  $M = \phi c_f + \frac{1}{K} (1 - \phi) (\alpha - \phi)$  is the Biot modulus or storativity,  $K$  is the rock drained bulk modulus,  $c_f$  is fluid compressibility, and  $\phi$  is rock porosity.

**Fracture flow.** We use the Darcy's law combined with the lubrication equation to approximate the fluid velocity in a fracture  $\mathbf{v}_F$ :

$$\mathbf{v}_F = -\frac{w(\mathbf{u})^2}{12\mu} (\nabla p_F - \rho_f \mathbf{g}) \quad (5.6)$$

where  $w(\mathbf{u})$  is the fracture width and  $p_F$  is the local fluid pressure in the fracture. We determine fracture width using the level-set method introduced in [111]. We assume a slightly compressible fluid similarly to the porous medium formulation.

The resulting pressure diffusivity equation in a fracture reads

$$c_f \frac{\partial p_F}{\partial t} - \nabla \cdot \frac{k_F}{\mu} (\nabla p - \rho_f \mathbf{g}) = q_F - q_L \quad (5.7)$$

where  $k_F = \frac{w(\mathbf{u})^2}{12\mu}$  is the local fracture permeability, and  $q_L$  is a term associated with the change of fracture width, commonly referred to as the “leak-off term” in the phase-field-modeling literature [127].

### 5.2.3 Reactive flow modeling

We limit our analysis to a simple carbonate-acid system. The chemical reaction between calcium carbonate  $\text{CaCO}_3$  and hydrochloric acid  $\text{HCl}$  can be described as follows:



The single-component transport of  $\text{HCl}$  concentration in the fluid phase  $C_f$  is dictated by the advection-dispersion equation [141, 2]:

$$\begin{cases} \frac{\partial C_f}{\partial t} + \nabla \cdot (\mathbf{v}C_f - D_F \nabla C_f) = q_F C_f^{inj} \\ \phi \frac{\partial C_f}{\partial t} + \nabla \cdot (\mathbf{v}C_f - D_R \nabla C_f) = q_R C_f^{inj} - k_c a_v (C_f - C_s) \end{cases} \quad (5.9)$$

where  $C_f$  is the  $\text{HCl}$  concentration in the fluid phase,  $C_s$  is the  $\text{HCl}$  concentration at the fluid-solid interface,  $C_f^{inj}$  is the injected  $\text{HCl}$  concentration,  $D_F$  is the effective dispersion in a fracture,  $D_R$  is the effective dispersion in the reservoir,  $k_c$  is the local mass transfer coefficient,  $a_v$  is the area of the reaction interface per unit volume, and  $q_R$  and  $q_F$  are the source terms that correspond fluid injection or production in the reservoir and fracture, respectively. The porosity evolution caused by mineral dissolution is

$$\frac{\partial \phi}{\partial t} = \frac{R(C_s) a_v \alpha_s}{\rho_s} \quad (5.10)$$

The kinetics equation for the first order reaction is simplified to  $R(C) = k_s C_s$ , which results in the expression for the concentration at fluid-solid interface

$$C_s = \frac{C_f}{1 + k_s/k_c} \quad (5.11)$$

Eq. 5.11 features two important limits of the reactive transport behavior

- when the reaction rate is high  $k_s \rightarrow \infty$ , the HCl concentration at the solid-fluid interface is equal to zero  $C_s = 0$ , and the reactive species consumption is controlled the local mass transfer only.
- when the reaction rate is low  $k_s \rightarrow 0$ , the HCl concentration at the solid-fluid interface is equal to the HCl concentration in the fluid phase  $C_s = C_f$ , and the reaction term in Eq. 5.9 approaches zero.

#### 5.2.4 Toughness-porosity model

In order to enable a direct coupling between the reactive flow model and the poromechanical model, we choose a unique toughness-porosity function. This function is unique for each porous medium. In this study we use a fit to the experimental data on fracture toughness as a function of local porosity for Indiana limestone provided in Chapter 4.

$$K_{IC} = -0.07432 \text{ MPa} \sqrt{\text{m}} \ln(\phi) + 0.0959 \text{ MPa} \sqrt{\text{m}} \quad (5.12)$$

where  $K_{IC}$  is fracture toughness measured in  $\text{MPa} \sqrt{\text{m}}$  and  $\phi$  is porosity ranging from 0 to  $\alpha$  within the poroelastic medium. We neglected changes in Young's modulus caused by changes in porosity. The effects of heterogeneity in fracture toughness  $K_{IC}$  are available in Chapter 4.

### 5.2.5 Numerical solution method

We use first-order continuous Galerkin FEM to approximate pressure, width, displacement, and phase-field variables. The phase field-displacement non-linear system is solved with Newton's method that facilitates the primal-dual active set algorithm [85]. The fluid-solid system is solved using the iterative fixed-stress split method [127]. We adaptively refine mesh locally in the fracture region using the predictor-corrector scheme in order to reduce the computational cost [85] .

The reactive transport is solved explicitly with a mix of finite volume and finite element methods. We use piecewise constant functions to represent concentration. The diffusion term between cells  $i$  and  $j$  is computed as in the finite volume method:

$$(D \nabla C_f)_{ij} = \frac{D_{ij}}{dx_{ij}} (C_{fi} - C_{fj}) dS_{ij} \quad (5.13)$$

where  $dx_{ij}$  is the distance between cell centers,  $p_i$  and  $p_j$  are the pressure values in cells  $i$  and  $j$ , respectively,  $D_{ij}$  is the diffusion coefficient on the cell face, and  $S_{ij}$  is the face area.

The advection term, on the other hand, is computed similarly to the Discontinuous Galerkin FEM as a quadrature integral:

$$(\mathbf{v} C_f)_{ij} = - \sum_q \frac{k_q}{\mu} \nabla p_q C_f^u dS_q \quad (5.14)$$

where  $q$  are indices of Gauss integration points on the face between cells  $i$  and  $j$ ,  $k_q$  and  $\nabla p_q$  are permeability and pressure gradient in the integration points, respectively,  $S_q$  is the face segment area, and  $C_f^u$  is the upwind concentration. This

approximation allows to solve the transport equation more accurately than with the standard finite volume methods since pressure and permeability values are computed with linear shape functions.

When computing the flux between two cells, a special case arises on the interface between a fine and a coarse cells. In this situation, we use the pressure gradients computed on the fine cell as implemented in deal.II [13].

### 5.2.6 Validation

The first validation case compares a numerical simulation with the analytical solution for the fracture aperture (referred to as crack opening displacement COD). The fracture aperture in a static (neither fluid flow nor crack propagation) fracture with half-length  $x_f$  and pressurized with constant (net) pressure  $p_F$  is given by the following equation as a function of x-coordinate (direction of fracture orientation) [181]:

$$\text{COD}(x) = \frac{2p_F x_f}{E'} \left(1 - \frac{x^2}{x_f^2}\right) \quad (5.15)$$

The simulation domain in our validation example is a square  $100 \text{ m} \times 100 \text{ m}$  with the maximum mesh size  $12.8 \text{ m}$  and minimum mesh size around a fracture  $h_{min} = 5 \text{ cm}$ . Other modeling parameters are as follows: fracture toughness  $K_{IC} = 0.45 \text{ MPa} \sqrt{\text{m}}$ , Young's modulus  $E = 3 \text{ GPa}$ , Poisson's ratio  $\nu = 0.2$ , Initial fracture half-length  $x_f^0 = 1 \text{ m}$ . In this simulation we set the fracture pressure to  $0.3 \text{ MPa}$ . The Biot coefficient is set to  $\alpha = 0$  to mimic a pressurized fracture in an elastic domain with no porosity. In the numerical model, fracture width is calculated with

a level-set algorithm described in [111]. The comparison of the CODs obtained by the numerical solution and Eq. 5.15 are shown in Fig. 5.2a.

We next compare steady-state pressure profile around the fracture with the radial analytical solution for wellbore flow.

$$p = (p_e - p_w) \frac{\ln(r/r_w)}{\ln(r_e/r_w)} + p_e \quad (5.16)$$

where  $p_w$  and  $p_e$  are the injection and reservoir pressures, respectively, and  $r_w$  and  $r_e$  are the wellbore and drainage radii, respectively. In this simulation we set reservoir pressure  $p_e$  to zero and injection pressure  $p_w$  to a constant value of 0.3 MPa. The fluid flow parameters as follows: fluid compressibility  $c_f = 10^{-3}$  MPa $^{-1}$ , fluid viscosity  $\mu = 10^{-3}$  Pa·s, and reservoir permeability  $k_R = 10^{-14}$  m $^2$ . We additionally set the Biot coefficient to a value  $\alpha = 0.7$ . In order to make the comparison, we assume the wellbore radius to be equal to the fracture half-length  $r_w = x_f^0$ . The simulation domain size and all other simulation parameters are the same as in the previous example. Fig. 5.2b presents the comparison of analytical and numerical results. We plot the numerical solution for a time instant  $t = 2,000$  s as a function of the distance from the fracture tip. The numerical result shows a nearly-constant pressure inside the fracture (distance  $< 1$  m) and then a logarithmic pressure decline to zero at 50 m that matches the analytical solution (distance  $> 1$  m). Hence, the model also accurately describes leak-off in a porous media.

Let us now show the validation of our phase-field model for the onset of propagation when the stress intensity at the fracture tip reaches the values of fracture toughness. Fluid is injected into the fracture with rate  $q_F = 5 \times 10^{-3}$  m $^3$ /s. We choose

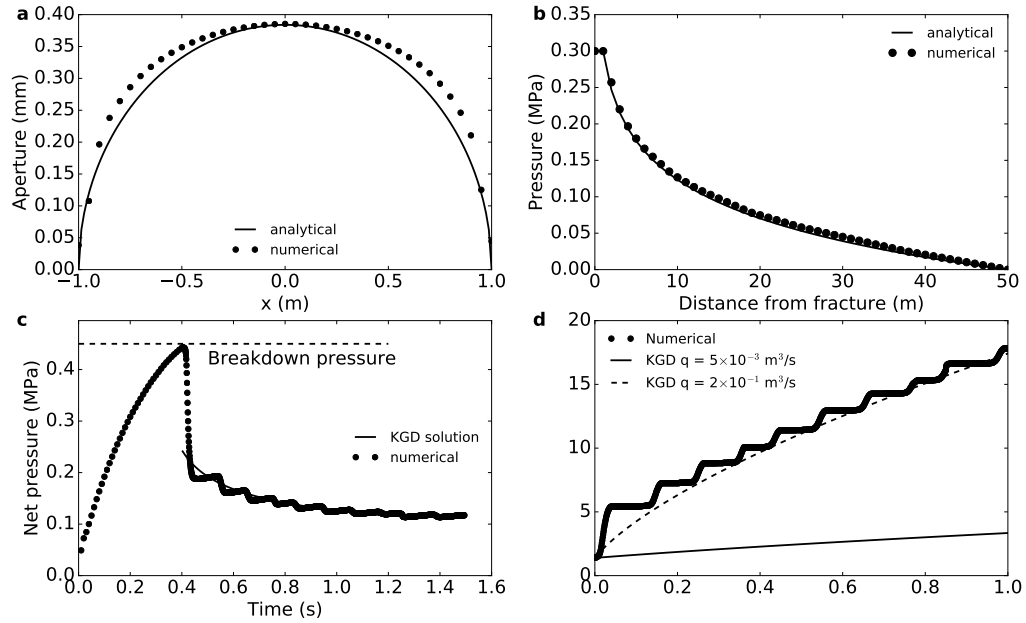


Figure 5.2: Comparison of FEM phase-field numerical simulations with analytical solutions. (a) Aperture of a static pressurized fracture as a function of x-coordinate compared to Sneddon's solution. (b) Pore pressure as a function of distance from the fracture tip and comparison with Darcy flow for steady state solution of wellbore equation. (c) Pressure in the fracture center as a function of time. Comparison of the breakdown pressure with Sneddon's solution. Comparison of the pressure decline after the breakdown with the KGD solution. (d) Comparison of the fracture half-length in the numerical simulation with the KGD model.

the diffusive zone width  $e = 2h$ . The time step in this simulation is  $10^{-3}$  s. Linear Elastic Fracture Mechanics predicts the breakdown pressure  $p_{bd}$  (constant pressure along fracture) at:

$$p_{bd} = \frac{K_{IC}}{\sqrt{x_f^0}} \quad (5.17)$$

which results in  $p_{bd} = 0.5$  MPa with our assumed parameters [198]. Fig. 5.2b shows pressure in the center of the fracture as a function of time. The fracture pressure increases for 0.16 s, time at which the fracture pressure reaches the formation breakdown pressure causing the fracture to start propagating. The simulated breakdown pressure matches the theoretical value (Eq. 5.17c).

We compare fracture pressure and half-length as functions of time with the KGD solution after the onset of propagation (Eq. 5.17c-d). The analytical KGD solutions for the fracture half-length  $x_f$  and pressure in the fracture center  $p$  are given by [97, 217, 69]:

$$p(t) = \left( \frac{21}{16} \frac{E'^2 \mu}{t} \right)^{1/3} \quad (5.18)$$

$$x_f = \left( \frac{16q^3 E'}{21\pi^3 \mu h_f^3} \right)^{1/6} t^{2/3} \quad (5.19)$$

The fracture pressure after the breakdown in the numerical simulation matches the analytical solution relatively well (Eq. 5.17c). Fracture half-length values given by the numerical simulation do not match those predicted by the KGD model with the rate  $q_F = 5 \times 10^{-3}$  m<sup>3</sup>/s but do match the KGD results with  $q_F = 2 \times 10^{-1}$  m<sup>3</sup>/s. This is a result of the simplification that consists in setting the source term  $q_L$  that describes the change of fracture width with time to zero. Accurate calculation of

this quantity is still an ongoing research topic. The presented model, however, matches the trend  $x_f \propto t^{2/3}$  which indicates the correct behavior of the simplified model. Note that KGD solution describes the growth of viscosity-dominated fractures that are not discussed in the paper. Instead, we focus on the slow growth of toughness-dominated fractures, and, therefore, the inaccuracies in fracture growth rates are irrelevant in our following results and discussion.

### 5.3 Results

This section presents the results of numerical simulations utilizing the physical model and equations presented above. For simplicity, we combine the coefficients in the reaction term in Eq. 5.9 and in Eq. 5.10 in order to identify two governing parameters for acid-driven fracture propagation. We introduce an “effective” reaction rate  $\tilde{k}_s = \frac{a_v k_c k_s}{k_c + k_s}$  and “effective” acid dissolving power  $\tilde{\alpha}_s = \frac{\alpha_s}{\rho_s}$ . Using this notation, we can rewrite the porous media flow part in Eq. 5.9 as

$$\phi \frac{\partial C_f}{\partial t} + \nabla \cdot (\mathbf{v} \tilde{C}_f - D_R \nabla C_f) = q_R - \tilde{k}_s C_f \quad (5.20)$$

and Eq. 5.10 as

$$\frac{\partial \phi}{\partial t} = \tilde{k}_s \tilde{\alpha}_s C_f \quad (5.21)$$

The effective reaction rate  $\tilde{k}_s$  affects acid consumption in the system and dissolution-induced porosity evolution. The effective acid dissolving power  $\tilde{\alpha}_s$  affects only the rate of porosity change. We first present a typical case of mineral-dissolution assisted fracture propagation and then a sensitivity analysis to input parameters.

### 5.3.1 Mineral dissolution-assisted fracture propagation

This subsection provides evidence from numerical simulation of how mineral dissolution can promote the growth of stalled fractures and evolution into toughness-dominated propagation. The simulations consists in pressurization (below breakdown pressure - Eq. 5.17) of an open fracture of predetermined length. Pressurization results in an increase of stress intensity at the tip and reactive fluid leak-off from the fracture face (Fig. 5.3).

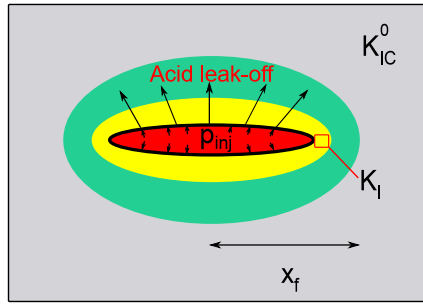


Figure 5.3: Schematics of a domain with a fracture with half-length  $x_f$ . Acid is injected with constant injection pressure  $p^{inj}$  which results in stress intensity  $K_I$  at the fracture tip. The intact rock has fracture toughness  $K_{IC}^0$ .

Fig. 5.4a presents a thought experiment on dissolution-assisted fracture propagation. The initial fracture half-length is  $x_f^0 = 0.1$  m and the injection pressure is  $p^{inj} = 0.4$  MPa. At the instant of injection the toughness in the domain is uniform  $K_{IC}^0 = 0.35$  MPa  $\sqrt{m}$ . The initial stress intensity at the fracture tip  $K_I^0 = p^{inj} \sqrt{x_f^0} = 0.13$  MPa  $\sqrt{m}$  is smaller than the intact rock fracture toughness  $K_{IC}^0$  so that the fracture is stalled. Upon injection, acid leak-off starts decreasing fracture toughness at the tip, until it reaches the value of current stress intensity at the tip  $K_I$ . At that moment, the fracture starts to grow encountering the rock region not subjected to

dissolution with high fracture toughness and stalls. Upon continued acid leak-off, fracture propagation proceeds whenever  $K_I > K_{IC}$ . Acid leak-off causes a reduction in fracture toughness to the current value of stress intensity, and the fracture relapses into propagation. Notice that under the assumption of constant pressure in the fracture, the required stress intensity for fracture propagation decreases with fracture length. As acidizing progresses, the fracture gradually grows until it reaches the critical length  $x_f^*$  ( $= 0.77$  m in this case), at which the stress intensity at the tip is equal to the intact rock toughness  $K_I = K_{IC}^0$ . When this occurs, fracture pressure is high enough to propagate the fracture without the assistance of mineral dissolution, which causes the fracture to evolve into viscosity-dominated (uncontrolled) fracture propagation.

We now present the results of two example simulations that aim to repeat the thought experiment. In these simulations the domain size is  $10\text{ m} \times 10\text{ m}$  and the fluid pressure is set constant and equal to zero at the boundaries. Other parameters are as follows: Young's modulus  $E = 3\text{ GPa}$ , Poisson's ratio  $\nu = 0.14$ , Biot coefficient  $\alpha = 0.7$ , rock permeability  $k = 1000\text{ mD}$ , fluid compressibility  $c_f = 10^{-3}\text{ MPa}^{-1}$ , fluid viscosity  $\mu = 10^{-3}\text{ Pa}\cdot\text{s}$ , and initial porosity is  $\phi^0 = 0.05$ . The reaction rate in both simulations is  $\tilde{k}_s = 10^{-4}\text{ s}^{-1}$ . The simulations differ only by the acid effective dissolving power  $\tilde{\alpha}_s$ .

- In the first simulation the dissolving acid power is relatively high  $\tilde{\alpha}_s = 10^2\text{ m}^3/\text{mol}$  (termed as “near-reach” case). The simulation parameters result in  $0.5\text{ m}^3$  of rock being dissolved (mostly near the fracture face) by  $0.2\text{ m}^3$  of the reactive fluid injected over approximately 30 seconds. Fig. 5.4b shows

the stress intensities and fracture toughness at the fracture tip as functions of time obtained from the numerical simulations. The behavior of the fracture toughness in the near-reach case resembles that in the thought experiment. The toughness at the fracture tip first reduces to the value of the stress intensity and then grows simultaneously with the stress tip intensity. The fracture lapses into uncontrolled propagation at the approximate half-length  $x_f = 0.77$  m.

- The second simulation has lower acid power than the first:  $\tilde{\alpha}_s = 10 \text{ m}^3/\text{mol}$  (far-reach case), which results in longer time for fracture propagation, and, therefore, a larger size of the leak-off zone. The simulation parameters in the second simulation result in  $0.4 \text{ m}^3$  of rock being consumed by  $1.9 \text{ m}^3$  of the reactive fluid injected over approximately 300 seconds. The behavior of fracture toughness as a function of time is different in the far-reach case. The size of the dissolved region around the fracture at the propagation onset time is higher than that in the near-reach case due to the lower dissolving power and later onset time. Therefore, when the tip fracture toughness reaches the tip stress intensity, the fracture lapses into uncontrolled propagation immediately.

Fig. 5.5 shows the distribution of phase-field variable, pressure, HCl dimensionless concentration, and toughness in the domain at three time steps for the simulations described in Fig. 5.4. The time instants are chosen as follows: (a) early time corresponds to the onset of propagation; (b) medium time corresponds to the

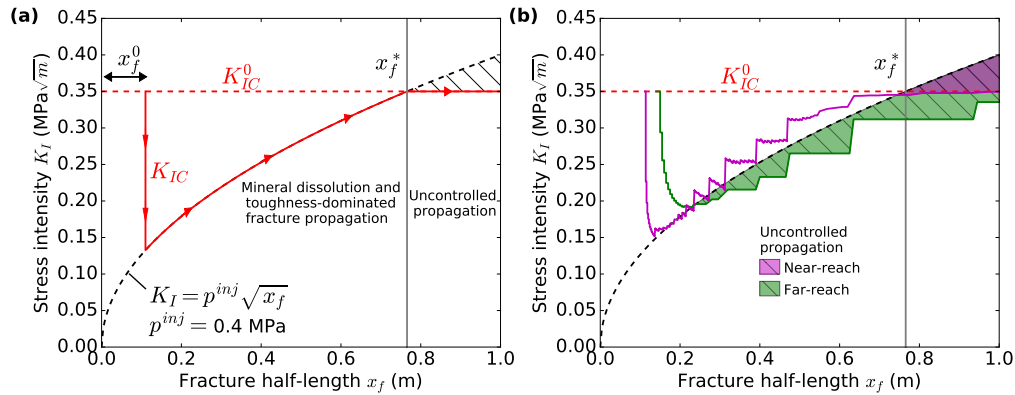


Figure 5.4: (a) An ideal case of mineral-dissolution-assisted fracture propagation with an infinite reaction rate and infinitely slow fracture growth. Fracture toughness and stress intensity at the fracture tip as functions of fracture half-length. Initially high fracture toughness at the tip of the fracture reduces due to mineral dissolution caused by acid leak-off until it reaches the value of tip stress intensity. Fracture starts propagating with the help of dissolution in a toughness-dominated regime with fracture toughness at the tip being approximately equal to stress intensity. At the critical length  $x_f^* = 0.77$  m stress intensity equals the intact rock toughness, and the fracture engages in uncontrolled propagation. (b) The results of “near-reach” (high acid power) and “far-reach” (low acid power) numerical simulations of the poroelastic model coupled with phase-field and single-component reactive fluid flow. Reaction rates are the same in both cases.

onset of uncontrolled fracture propagation for the far-reach case ( $x_f \approx 1$  in both cases); and (c) late time is a point when  $x_f = 2$  m and occurs during uncontrolled fracture propagation for both cases. The distributions of the phase-field variable and pressure are almost the same for both simulation cases at the chosen times. At the onset of propagation the pressure distribution around the fracture is nearly radial as the fracture is small compared to the domain size. At the medium and late times the equipotential pressure contours elongate due to the fracture growth. The concentration distribution in the figure indicates a larger size (about 10 times) of the leak-off area for the far-reach case than for the near-reach case. After the onset of fracture propagation, the leak-off area changes its shape slightly for near-reach case and stays nearly the same for the far-reach case as the fracture propagates more quickly than the leak-off front. The evolution of the dissolved areas (with reduced toughness) resembles that of the areas with high acid concentration. The dissolved area changes slightly in the near-reach cases and stays nearly unchanged in the far-reach case. A notable difference between the dissolved areas and high acid concentration areas is that the toughness beyond the dissolved lags behind the fracture tip.

### 5.3.2 Sensitivity analysis

Fig. 5.6 presents a sensitivity study of fracture half-length  $x_f$  as a function of time for varying reaction rate and dissolving power. The base case has an effective reaction rate  $\tilde{k}_s = 10^{-4} \text{ s}^{-1}$  and effective acid dissolving power  $\tilde{\alpha}_s = 10^2 \text{ m}^3/\text{mol}$ . All other parameters are the same as in the simulations described in Section 5.3.1.

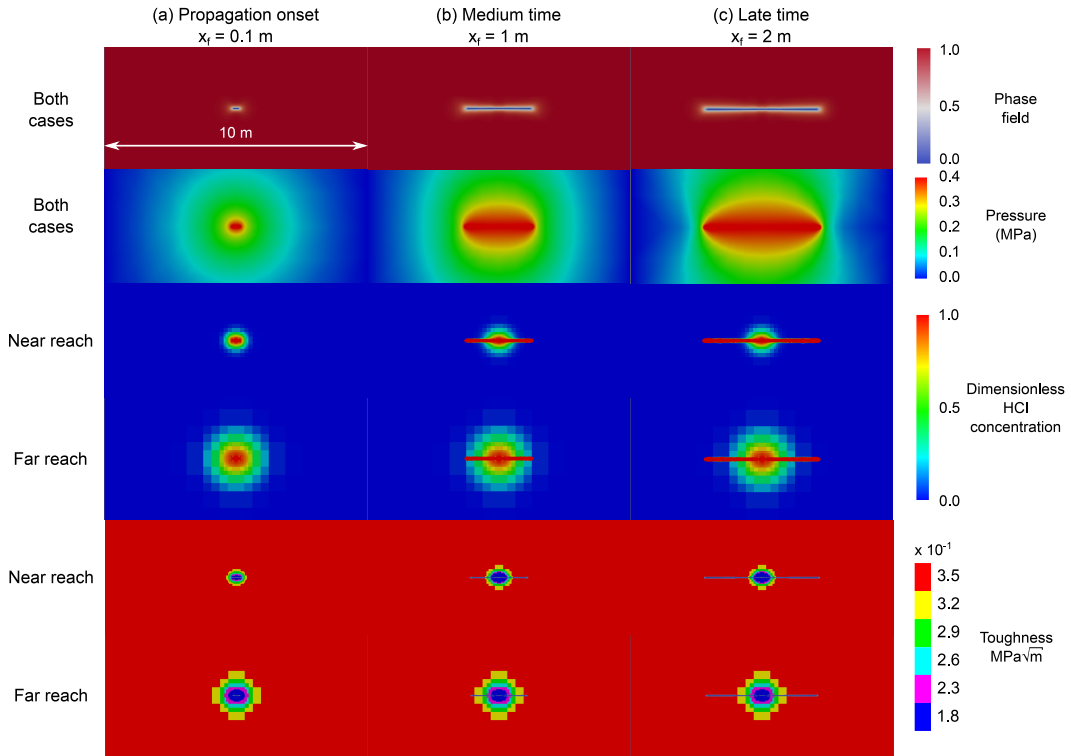


Figure 5.5: Phase-field, pressure, dimensionless HCl concentration, and toughness at various time instants for two simulation cases: the onset of propagation, time when  $x_f = 1$  m, time when  $x_f = 2$  m. The phase-field and pressure distributions are approximately the same at the chosen times for each simulation case. The toughness images show superimposed phase-field maps with  $\varphi < 0.2$  for visual aid of fracture length.

Fig. 5.6a shows the sensitivity to the effective reaction rate  $\tilde{k}_s$ . We computed acid-assisted fracture propagation cases for the effective reaction rate values  $\tilde{k}_s = 10^{-6} \text{ s}^{-1}$ ,  $10^{-5} \text{ s}^{-1}$ ,  $10^{-4} \text{ s}^{-1}$ , and  $10^{-3} \text{ s}^{-1}$ . In each case fracture half-length remains constant for a period of time while acid leaks off and reduces fracture toughness around the fracture. At the time when the toughness near the fracture tips becomes equal to the stress intensity at the tip, the fracture starts to propagate slowly. Afterwards, the propagation velocity increases gradually with time until stress intensity at the fracture tip exceeds the toughness of intact rock and the fracture snaps off into uncontrolled fracture propagation. According to the numerical simulations, high reaction rates result in an early onset of propagation and gradual change of fracture velocity towards uncontrolled propagation.

Fig. 5.6b shows the sensitivity to the effective dissolving power  $\tilde{\alpha}_s$ . In these simulations we varied the effective dissolving power  $\tilde{\alpha}_s = 10^0 \text{ m}^3/\text{mol}$ ,  $10^1 \text{ m}^3/\text{mol}$ ,  $10^2 \text{ m}^3/\text{mol}$ , and  $10^3 \text{ m}^3/\text{mol}$ . High values of dissolving power result in early uncontrolled propagation times. Fig. 5.6b shows similar trends to 5.6a. This is due to porosity evolution governed by the product of the effective reaction rate and the effective dissolving power  $\Delta\phi \propto \tilde{\alpha}_s \tilde{k}_s$ .

Fig. 5.7a shows the HCl dimensionless concentration as a function of distance from the fracture face in the direction perpendicular to the fracture at the instant of fracture propagation for various effective reaction rates  $\tilde{k}_s$ . Since the reaction rate controls the rate of acid consumption, high reaction rates result in narrow leak-off and acidized zones. Fig. 5.7b shows the leak-off zone calculated as the double of the distance from the fracture at which concentration still exceeds the

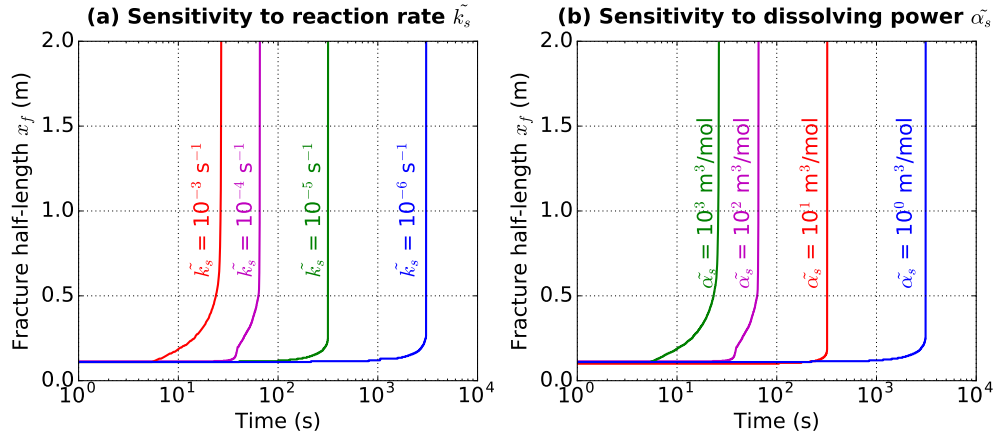


Figure 5.6: Fracture half-length as a function of time. Base case:  $\tilde{\alpha}_s = 10^2 \text{ m}^3/\text{mol}$  and  $\tilde{k}_s = 10^{-4} \text{ s}^{-1}$ . (a) Sensitivity to effective reaction rate  $\tilde{k}_s$ . (b) Sensitivity to effective dissolving power  $\tilde{\alpha}_s$ .

value  $\tilde{C}_f = 0.5$ . Since the x-axis in Fig. 5.7b has a logarithmic scale and the shown points align on a straight line, this behavior indicates that the leak-off zone size is proportional to the logarithm of reaction rate.

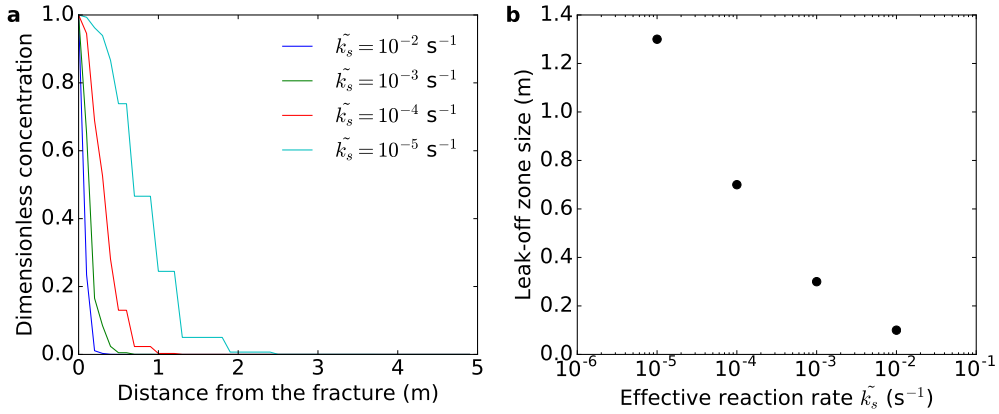


Figure 5.7: The width of the high-concentration region as a function of the effective reaction rate  $\tilde{k}_s$ .

## 5.4 Discussion

### 5.4.1 Extension to fully-coupled reactive flow including modeling of wormholes

The results shown in Sections 5.3.1 and 5.3.2 do not include changes in permeability due to mineral dissolution. It is well-known that reactive transport can lead to fluid flow instabilities and development of localized mineral dissolution, a phenomenon known as wormhole development [72].

Carman-Kozeny equation can be used to model dissolution-induced the alteration of the absolute permeability of the porous medium:

$$\frac{k_R}{k_R^0} = \frac{\phi}{\phi^0} \left[ \frac{\phi(1 - \phi^0)}{\phi^0(1 - \phi)} \right]^{2\beta} \quad (5.22)$$

where  $k_R$  is the rock permeability increased by mineral dissolution,  $k_R^0$  is the permeability of the intact media,  $\phi$  is the damaged rock porosity,  $\phi^0$  is the porosity of the intact rock, and  $\beta$  is a dimensionless pore structure constant [102, 27]. When using Eq. 5.22, it is essential to modify other reactive flow coefficients, such as the reactive fluid-rock interface area  $a_v$ , accordingly:

$$\frac{a_v}{a_v^0} = \frac{\phi}{\phi^0} \left[ \frac{\phi(1 - \phi^0)}{\phi^0(1 - \phi)} \right]^{-\beta} \quad (5.23)$$

where  $a_v^0$  is the interface area per unit volume in the intact rock [2]. Reaction rate parameter  $k_s$  and mechanical dispersion can be estimated using correlations:

$$Sh = \frac{2k_c r}{D_m} = Sh_\infty + 0.7 \sqrt{Re} \sqrt[3]{Sc} \quad (5.24)$$

$$D_{eX} = \alpha_{os} D_m + \frac{2\lambda_X |\mathbf{v}| r}{\epsilon} \quad (5.25)$$

$$D_{eT} = \alpha_{os} D_m + \frac{2\lambda_T |\mathbf{v}| r}{\epsilon}$$

where  $\text{Sh}$  is the dimensionless mass-transfer coefficient (Sherwood number) and  $\text{Sh}_\infty$  is its asymptotic value,  $\text{Re} = \frac{2|\nu|r}{\nu}$  is the Reynold's number,  $\text{Sc}$  is the Schmidt number  $\text{Sc} = \frac{\nu}{D_m}$ ,  $\nu$  is the fluid kinematic viscosity.  $\alpha_{os}$  is a pore connectivity constant,  $D_{eX}$  and  $D_{eT}$  are the longitudinal and transverse dispersion coefficients, respectively,  $\lambda_X$  and  $\lambda_T$  are constants that depend on the geometrical medium structure, and  $r$  is the pore radius modified according to the Carman-Kozeny formula:

$$\frac{r_p}{r_p^0} = \frac{\phi}{\phi^0} \left[ \frac{\phi(1-\phi^0)}{\phi^0(1-\phi)} \right]^\beta \quad (5.26)$$

where  $r_p^0$  is the pore radius of the intact rock [95, 117, 2].

In the presented simulations we limited the maximum porosity to be lower than the Biot coefficient so that the theory of poroelasticity is still valid. In reality, the leak-off of strong highly-concentrated acids can lead to high dissolution amounts within the proximity of the hydraulic fracture faces so that the Biot coefficient needs to be recomputed accordingly. The simulation of fluid flow in such highly-dissolved regions needs to be handled appropriately in order to produce physical results. We suggest that in phase-field simulations, the phase-field  $\varphi$  value may be modified to represent a void upon reaching a critical porosity value  $\phi_c$ , e.g.

$$\varphi = 1 - \chi(\phi - \phi_c) \quad (5.27)$$

where  $\chi$  is a fitting coefficient.

### 5.4.2 Experimental validation

In this section we suggest a laboratory experimental setup to verify the influence of reactive fluid flow on fracture propagation from numerical simulation. In essence, we propose to perform a laboratory step rate test (Fig. 5.8). The first experiment should measure formation parting pressure by increasing the injection rate in an unconfined block with free drainage boundaries. Subsequent experiments on similar blocks utilize an HCl solution of variable molarity and the same injection schedule. The reduction of breakdown pressure will be directly related to reactive transport processes induced by acid injection. The variability of reaction rate can be controlled using retarded acid systems [180].

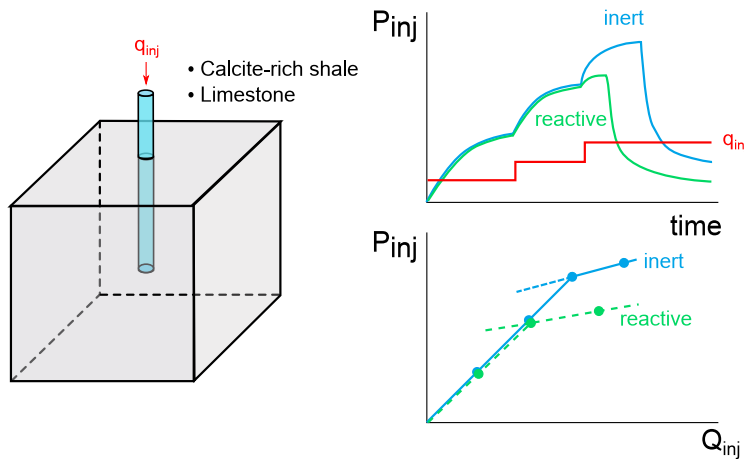


Figure 5.8: An example of an experimental setup to explore the effects of acid injection on break-down pressure.

### 5.4.3 Applications for acid fracturing in tight formations

The conventional understanding of hydraulic fracturing envisioned single long planar hydraulic fractures. In such cases acid injection may be utilized to only lower the formation breakdown pressure (while toughness-dominated) but has no effect of further propagation in the viscosity-dominated regime other than fracture face etching. However, the contemporary understanding of hydraulic fracturing gained from the detection microseismic events indicates complex ramification of hydraulic fractures [59, 202]. In this case fracture branches are likely to be toughness-dominated. We propose the following mechanism to illustrate the potential benefits of using acid fracturing in a case of complex fracture networks in a reservoir. Fig. 5.9a shows a long viscosity-dominated propagating fracture and its short toughness-dominated branch. We assume that the injection pressure is sufficient for the long fracture to propagate, whereas the branch is stalled. Since pressure in the stalled fracture is higher than the formation pressure, reactive-fluid leaks from the stalled fracture (Fig. 5.9b). Mineral dissolution that occurs due to leak-off, decreases fracture toughness at the tip of the stalled fracture, which starts propagating (Fig. 5.9c). If the fracture grows sufficiently long, it can evolve from a toughness-dominated to a viscosity-dominated regime, and thus increase the complexity and surface area of the fracture network. Another alternative consists in injection acid slugs and waiting for leak-off in each cycle.

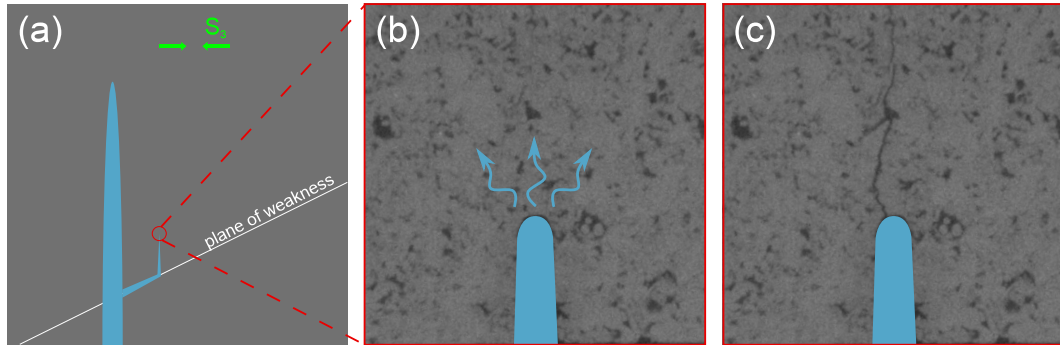


Figure 5.9: Acid-assisted fracture propagation.

## 5.5 Conclusions

- Direct coupling of a numerical fracture-propagation model based on the phase-field approach with reactive fluid flow is possible by relating rock porosity and toughness.
- Numerical simulation results indicate that mineral dissolution may stimulate the growth of stalled fluid-driven toughness-dominated fractures and short fractures to transition into the viscosity-dominated regime.
- Rapidly-reacting acids that result in near-reaching leak-off fronts cause gradual fracture growth in the toughness-dominated regime followed by a transition into the viscosity-dominated regime.
- Far-reaching acid leak-off fronts (e.g., achieved with retardation agents) may cause fractures to propagate abruptly in the viscosity-dominated regime upon the onset of propagation (slowly-reacting acids can be used to increase the size of the stimulated area).

- An extension to the current model is possible in order to capture wormhole development simultaneously with fracture propagation.
- Acid fracturing could help propagate short fracture branches and thus increase fracture complexity.

# **Chapter 6**

## **Conclusions**

This dissertation presents a study of the mechanical effects of two chemical processes: gas-desorption from organic-rich rocks and mineral dissolution in carbonate-rich formations. Conclusions drawn from this work are as follows:

- A coupled poromechanical model capable of accounting for changes in sorption stresses and permeability in stress-sensitive dry gas reservoirs that allows for simulation of non-trivial production rate evolution as a function of time has been developed and used to model field cases of reservoirs with strong and weak sorption-mechanical coupling.
- Rock permeability alterations in stress-sensitive reservoirs vary significantly within reservoirs due to stress heterogeneity, stress shadowing, drainage of pore pressure, and gas desorption.
- Dissolution of mineralized veins can lead to a significant permanent relaxation of horizontal stresses that can potentially reactivate critically-oriented fractures.
- Numerical simulation confirmed that desorption-induced strains in shales may induce changes of horizontal stresses of several MPa. These changes of stress

may have a minor effect on permeability but can significantly affect horizontal stress anisotropy and should be considered while planning refracturing.

- Permeability in some reservoirs is highly sensitive to the rock mass Young's modulus, maximum swelling strain of the rock, and the formation fracture compressibility.
- Relaxation of horizontal stress due to dissolution in mineralized veins in carbonate-rich shale reservoirs is supported by both numerical simulation and laboratory experiments.
- Closed-form analytical solution has been derived to quantify decreases in horizontal stresses due to dissolution of mineralized veins assuming uniform redistribution of minerals, constant vertical stress, and no change in pore pressure. This model can be utilized to characterize shale reservoirs as potential candidates to acidizing.
- Dissolution of mineralized veins has a similar effect on the stress state as thermal-induced anisotropic shrinkage.
- A conversion equation between a decrease in temperature of a thermoelastic domain and a dissolved fraction of mineralized veins has been derived.
- FEM-based reservoir-scale numerical simulations that use an analogy with thermoelasticity showed that mineral dissolution can be used to mitigate proppant-placement-induced local principal stress reorientation and reduce spacing between hydraulic fractures in carbonate-rich reservoirs.

- Numerical simulations confirmed that mineral dissolution can potentially lead to reactivation of critically-oriented natural fractures in carbonate-rich shale reservoirs.
- Open-mode fractures from semicircular bending experiments in acidized limestone samples exhibit non-planar geometry and follow high porosity regions and large pores.
- Fracture toughness correlates well with local macro-porosity. Our results of semicircular bending and  $\mu$ CT image processing in limestone rock samples suggest a rapid toughness decrease at low porosities and a more gradual decrease at larger porosities.
- Phase-field numerical simulations using a heterogeneous toughness map validate a direct relationship between fracture toughness and porosity that permits replicating fracture stress intensity at initiation and non-planar propagation patterns observed in experiments.
- A link between reactive fluid flow, poro-elasticity, and fracture propagation is possible through the variable porosity and associated constitutive relations: toughness vs. porosity, elastic properties vs. porosity, and permeability vs. porosity.
- The proposed coupling solution is a first order approximation for reactive fluid flow applications in sinkhole development, hydraulic fracturing, and carbon geological storage.

- Direct coupling of a numerical fracture-propagation model based on the phase-field approach with reactive fluid flow is possible by relating rock porosity and toughness.
- Numerical simulation results indicate that mineral dissolution may stimulate the growth of stalled fluid-driven toughness-dominated fractures and short fractures to transition into the viscosity-dominated regime.
- Rapidly-reacting acids that result in near-reaching leak-off fronts cause gradual fracture growth in the toughness-dominated regime followed by a transition into the viscosity-dominated regime.
- Far-reaching acid leak-off fronts (e.g., achieved with retardation agents) may cause fractures to propagate abruptly in the viscosity-dominated regime upon the onset of propagation (slowly-reacting acids can be used to increase the size of the stimulated area).
- An extension to the numerical model developed in Chapter 4 is proposed in order to capture wormhole development simultaneously with fracture propagation.
- Acid fracturing could help propagate short fracture branches and thus increase fracture complexity.

## Bibliography

- [1] Kalld Mohammed Abdalkadeer, E Senturk, S Dunn-Norman, HE Goodman, Martin Prada, and N Rivera. Changes in near wellbore stress and fracture gradient due to cold water injection in a sirte basin field, libya. In SPE/EAGE Reservoir Characterization & Simulation Conference, 2009.
- [2] Olatokunbo O Akanni. Mathematical Modeling of Wormhole Propagation during Matrix Acidizing of Carbonate Reservoirs. PhD thesis, 2015.
- [3] Olatokunbo O Akanni, Hisham A Nasr-El-Din, et al. Modeling of wormhole propagation during matrix acidizing of carbonate reservoirs by organic acids and chelating agents. In SPE Annual Technical Conference and Exhibition. Society of Petroleum Engineers, 2016.
- [4] Hasan A Al-Ahmadi, Robert A Wattenbarger, et al. Triple-porosity models: one further step towards capturing fractured reservoirs heterogeneity. In SPE/DGS Saudi Arabia Section Technical Symposium and Exhibition. Society of Petroleum Engineers, 2011.
- [5] Mohammed A Al Duhalan, Stephen A Sonnenberg, and Mark Longman. Analyzing beef fractures: Genesis and relationship with organic-rich shale facies. In Unconventional Resources Technology Conference, San Antonio,

Texas, 20-22 July 2015, pages 1176–1191. Society of Exploration Geophysicists, American Association of Petroleum Geologists, Society of Petroleum Engineers, 2015.

- [6] Mohammed Badri Al-Otaibi, Hisham A Nasr-El-Din, Abdullah Mohammad Al Moajil, et al. In-situ acid system to clean up drill-in fluid damage in high temperature gas wells. In IADC/SPE Asia Pacific Drilling Technology Conference and Exhibition. Society of Petroleum Engineers, 2006.
- [7] Michael Aman, D Nicolas Espinoza, Anastasia G Ilgen, Jonathan R Major, Peter Eichhubl, and Thomas A Dewers. Co<sub>2</sub>-induced chemo-mechanical alteration in reservoir rocks assessed via batch reaction experiments and scratch testing. Greenhouse Gases: Science and Technology, 8(1):133–149, 2018.
- [8] Ted L Anderson. Fracture mechanics: fundamentals and applications. CRC press, 2017.
- [9] Ted Apotria, Charles J Kaiser, Bruce A Cain, et al. Fracturing and stress history of the devonian antrim shale, michigan basin. In 1st North American Rock Mechanics Symposium. American Rock Mechanics Association, 1994.
- [10] Standard test method for evaluation of asphalt mixture cracking resistance using the semi-circular bend test (scb) at intermediate temperatures. Standard, ASTM International, West Conshohocken, PA, 2016.

- [11] Barry Kean Atkinson. Subcritical crack growth in geological materials. Journal of Geophysical Research: Solid Earth, 89(B6):4077–4114, 1984.
- [12] Barry Kean Atkinson. Fracture mechanics of rock. Elsevier, 2015.
- [13] W. Bangerth, D. Davydov, T. Heister, L. Heltai, G. Kanschat, M. Kronbichler, M. Maier, B. Turcksin, and D. Wells. The deal.II library, version 8.4. Journal of Numerical Mathematics, 24, 2016.
- [14] Kim D Basham. Nonlinear fracture mechanics using semicircular specimens and tension-softening behavior. 1990.
- [15] SJ Bauer, Brann Johnson, et al. Effects of slow uniform heating on the physical properties of the westerly and charcoal granites. In 20th US Symposium on Rock Mechanics (USRMS). American Rock Mechanics Association, 1979.
- [16] SP Becker, P Eichhubl, SE Laubach, RM Reed, RH Lander, and RJ Bodnar. A 48 my history of fracture opening, temperature, and fluid pressure: Cretaceous travis peak formation, east texas basin. Geological Society of America Bulletin, 122(7-8):1081–1093, 2010.
- [17] James G Berryman. Mixture theories for rock properties. Rock physics & phase relations: A handbook of physical constants, pages 205–228, 1995.
- [18] Prateek Bhardwaj, Jongsoo Hwang, Ripudaman Manchanda, Mukul M Sharma, et al. Injection induced fracture propagation and stress reorientation in waterflooded reservoirs. In SPE Annual Technical Conference and Exhibition. Society of Petroleum Engineers, 2016.

- [19] Michael J Borden, Clemens V Verhoosel, Michael A Scott, Thomas JR Hughes, and Chad M Landis. A phase-field description of dynamic brittle fracture. *Computer Methods in Applied Mechanics and Engineering*, 217:77–95, 2012.
- [20] Blaise Bourdin, Gilles A Francfort, and Jean-Jacques Marigo. Numerical experiments in revisited brittle fracture. *Journal of the Mechanics and Physics of Solids*, 48(4):797–826, 2000.
- [21] Laurent Brochard, Matthieu Vandamme, Roland J-M Pellenq, and Teddy Fen-Chong. Adsorption-induced deformation of microporous materials: coal swelling induced by co<sub>2</sub>–ch<sub>4</sub> competitive adsorption. *Langmuir*, 28(5):2659–2670, 2012.
- [22] Vicente Brotons, Roberto Tomás, Salvador Ivorra, Angel Grediaga, Javier Martínez-Martínez, David Benavente, and Miguel Gómez-Heras. Improved correlation between the static and dynamic elastic modulus of different types of rocks. *Materials and structures*, 49(8):3021–3037, 2016.
- [23] Kevin M Brown, Barbara Bekins, B Clennell, D Dewhurst, and G Westbrook. Heterogeneous hydrofracture development and accretionary fault dynamics. *Geology*, 22(3):259–262, 1994.
- [24] Andrew P Bunger, Emmanuel Detournay, and Dmitry I Garagash. Toughness-dominated hydraulic fracture with leak-off. *International journal of fracture*, 134(2):175–190, 2005.

- [25] A Busch, P Bertier, Y Gensterblum, G Rother, CJ Spiers, M Zhang, and HM Wentinck. On sorption and swelling of co<sub>2</sub> in clays. *Geomechanics and Geophysics for Geo-Energy and Geo-Resources*, 2(2):111–130, 2016.
- [26] Philip Cardiff, Ripudaman Manchanda, Eric C Bryant, Dongkeun Lee, Alojz Ivankovic, and Mukul M Sharma. Simulation of fractures in openfoam: from adhesive joints to hydraulic fractures. In 10th OpenFOAM Workshop, 2015.
- [27] Philip Crosbie Carman. Fluid flow through granular beds. *Trans. Inst. Chem. Eng.*, 15:150–166, 1937.
- [28] Declan Carolan, Željko Tuković, Neal Murphy, and Alojz Ivanković. Arbitrary crack propagation in multi-phase materials using the finite volume method. *Computational materials science*, 69:153–159, 2013.
- [29] Susan Carroll, Yue Hao, Megan Smith, and Yelena Sholokhova. Development of scaling parameters to describe co<sub>2</sub>–rock interactions within weyburn-midale carbonate flow units. *International Journal of Greenhouse Gas Control*, 16:S185–S193, 2013.
- [30] AW Chan, MD Zoback, et al. Deformation analysis in reservoir space (dars): a simple formalism for prediction of reservoir deformation with depletion. In SPE/ISRM Rock Mechanics Conference. Society of Petroleum Engineers, 2002.

- [31] Tianyu Chen, Xia-Ting Feng, and Zhejun Pan. Experimental study of swelling of organic rich shale in methane. International Journal of Coal Geology, 150:64–73, 2015.
- [32] L Chiaramonte, S Johnson, JA White, et al. Preliminary geomechanical analysis of co2 injection at snøhvit, norway. In 45th US Rock Mechanics/Geomechanics Symposium. American Rock Mechanics Association, 2011.
- [33] Jay C Close and Matthew J Mavor. Influence of coal composition and rank on fracture development in fruitland coal gas reservoirs of. 1991.
- [34] O. Coussy. Mechanics and Physics of Porous Solids. Wiley, 2010.
- [35] Olivier Coussy. Mechanics and physics of porous solids. John Wiley & Sons, 2011.
- [36] Melanie M Coyan, J Ramón Arrowsmith, Paul Umhoefer, Joshua Coyan, Graham Kent, Neal Driscoll, and Genaro Martínez Gutierrez. Geometry and quaternary slip behavior of the san juan de los planes and saltito fault zones, baja california sur, mexico: Characterization of rift-margin normal faults. Geosphere, 9(3):426–443, 2013.
- [37] BR Crawford. Experimental fault sealing: shear band permeability dependency on cataclastic fault gouge characteristics. Geological Society, London, Special Publications, 127(1):27–47, 1998.
- [38] Delphine Croizé. Mechanical and chemical compaction of carbonates: an experimental study. 2010.

- [39] SL Crouch. Solution of plane elasticity problems by the displacement discontinuity method. i. infinite body solution. International Journal for Numerical Methods in Engineering, 10(2):301–343, 1976.
- [40] Q Cui, HH Abass, et al. Experimental study of permeability decline in tight formations during long-term depletion. In SPE Low Perm Symposium. Society of Petroleum Engineers, 2016.
- [41] F Cusack, DR Brown, JW Costerton, and DM Clementz. Field and laboratory studies of microbial/fines plugging of water injection wells: Mechanism, diagnosis and removal. Journal of Petroleum Science and Engineering, 1(1):39–50, 1987.
- [42] Arash Dahi Taleghani, Jon E Olson, et al. How natural fractures could affect hydraulic-fracture geometry. SPE journal, 19(01):161–171, 2013.
- [43] SM De Jong, CJ Spiers, and A Busch. Development of swelling strain in smectite clays through exposure to carbon dioxide. International Journal of Greenhouse Gas Control, 24:149–161, 2014.
- [44] E Detournay. Propagation regimes of fluid-driven fractures in impermeable rocks. International Journal of Geomechanics, 4(1):35–45, 2004.
- [45] E Detournay, AH-D Cheng, and JD McLennan. A poroelastic pkn hydraulic fracture model based on an explicit moving mesh algorithm. Journal of energy resources technology, 112(4):224–230, 1990.

- [46] Antonio Fabio Di Rienzo, Pietro Asinari, Eliodoro Chiavazzo, NI Prasianakis, and J Mantzaras. Lattice boltzmann model for reactive flow simulations. *EPL (Europhysics Letters)*, 98(3):34001, 2012.
- [47] C Armando Duarte, Ivo Babuška, and J Tinsley Oden. Generalized finite element methods for three-dimensional structural mechanics problems. *Computers & Structures*, 77(2):215–232, 2000.
- [48] Marcus Ebner, Daniel Koehn, Renaud Toussaint, François Renard, and Jean Schmittbuhl. Stress sensitivity of stylolite morphology. *Earth and Planetary Science Letters*, 277(3):394–398, 2009.
- [49] Michael J Economides, Tony Martin, et al. *Modern fracturing: Enhancing natural gas production*. ET Publishing Houston, Texas, 2007.
- [50] Thushan Chandrasiri Ekneligoda and Ki-Bok Min. Determination of optimum parameters of doublet system in a horizontally fractured geothermal reservoir. *Renewable Energy*, 65:152–160, 2014.
- [51] S Enayatpour, E Van Oort, T Patzek, et al. Freezefrac improves the productivity of gas shales. In *SPE Annual Technical Conference and Exhibition*. Society of Petroleum Engineers, 2013.
- [52] D Nicolas Espinoza, Igor Shovkun, Omar Makni, and Nicolas Lenoir. Natural and induced fractures in coal cores imaged through x-ray computed microtomographyimpact on desorption time. *International Journal of Coal Geology*, 154:165–175, 2016.

- [53] D. Nicolas Espinoza, Matthieu Vandamme, J. M. Pereira, Patrick Dangla, and Sandrine Vidal-Gilbert. Measurement and modeling of adsorptive-poromechanical properties of bituminous coal cores exposed to CO<sub>2</sub>: adsorption, swelling strains, swelling stresses and impact on fracture permeability. *International Journal of Coal Geology*, 134-135:80–95, 2014.
- [54] DN Espinoza, J-M Pereira, Matthieu Vandamme, Patrick Dangla, and S Vidal-Gilbert. Desorption-induced shear failure of coal bed seams during gas depletion. *International Journal of Coal Geology*, 137:142–151, 2015.
- [55] DN Espinoza, M Vandamme, J-M Pereira, P Dangla, and S Vidal-Gilbert. Measurement and modeling of adsorptive–poromechanical properties of bituminous coal cores exposed to co 2: Adsorption, swelling strains, swelling stresses and impact on fracture permeability. *International Journal of Coal Geology*, 134:80–95, 2014.
- [56] DN Espinoza, Matthieu Vandamme, Patrick Dangla, J-M Pereira, and S Vidal-Gilbert. A transverse isotropic model for microporous solids: Application to coal matrix adsorption and swelling. *Journal of Geophysical Research: Solid Earth*, 118(12):6113–6123, 2013.
- [57] Marc Kevin Fisher, Christopher A Wright, Brian Michael Davidson, AK Goodwin, EO Fielder, WS Buckler, NP Steinsberger, et al. Integrating fracture mapping technologies to optimize stimulations in the barnett shale. In *SPE Annual Technical Conference and Exhibition*. Society of Petroleum Engineers, 2002.

- [58] Marc Kevin Fisher, Christopher A Wright, Brian Michael Davidson, Nicholas P Steinsberger, William Stanley Buckler, Alan Goodwin, Eugene O Fielder, et al. Integrating fracture mapping technologies to improve stimulations in the barnett shale. SPE Production & Facilities, 20(02):85–93, 2005.
- [59] MK Fisher, CA Wright, BM Davidson, AK Goodwin, EO Fielder, WS Buckler, and NP Steinsberger. Integrating fracture-mapping technologies to improve stimulations in the barnett shale, spe 77441. SPE Journal Production and Facilities, 20(2), 2005.
- [60] John T Foster. Dynamic crack initiation toughness: Experiments and peridynamic modeling. DOI, 10:1001000, 2009.
- [61] Gilles A Francfort and J-J Marigo. Revisiting brittle fracture as an energy minimization problem. Journal of the Mechanics and Physics of Solids, 46(8):1319–1342, 1998.
- [62] Christopher N Fredd and H Scott Fogler. Influence of transport and reaction on wormhole formation in porous media. AIChE journal, 44(9):1933–1949, 1998.
- [63] TP Frick, Behdokht Mostofizadeh, MJ Economides, et al. Analysis of radial core experiments for hydrochloric acid interaction with limestones. In SPE Formation Damage Control Symposium. Society of Petroleum Engineers, 1994.

- [64] Julia FW Gale and Jon Holder. Natural fractures in some us shales and their importance for gas production. In Geological Society, London, Petroleum Geology Conference Series, volume 7, pages 1131–1140. Geological Society of London, 2010.
- [65] Julia FW Gale, Robert M Reed, and Jon Holder. Natural fractures in the barnett shale and their importance for hydraulic fracture treatments. AAPG bulletin, 91(4):603–622, 2007.
- [66] TT Garipov, M Karimi-Fard, and HA Tchelepi. Discrete fracture model for coupled flow and geomechanics. Computational Geosciences, 20(1):149, 2016.
- [67] M Gasparik, A Ghanizadeh, P Bertier, Y Gensterblum, S Bouw, and Bernhard M Krooss. High-pressure methane sorption isotherms of black shales from the netherlands. Energy & fuels, 26(8):4995–5004, 2012.
- [68] Rick Gdanski. A fundamentally new model of acid wormholing in carbonates. In European formation damage conference, pages 107–116, 1999.
- [69] J Geertsma, F De Klerk, et al. A rapid method of predicting width and extent of hydraulically induced fractures. Journal of Petroleum Technology, 21(12):1–571, 1969.
- [70] Ebrahim Ghanbari, Majid Ali Abbasi, Hassan Dehghanpour, Doug Bearinger, et al. Flowback volumetric and chemical analysis for evaluating load re-

covery and its impact on early-time production. In SPE Unconventional Resources Conference Canada. Society of Petroleum Engineers, 2013.

- [71] A Ghassemi and X Zhou. A three-dimensional thermo-poroelastic model for fracture response to injection/extraction in enhanced geothermal systems. Geothermics, 40(1):39–49, 2011.
- [72] F Golfier, Cesar ZARCONE, B Bazin, R Lenormand, D Lasseux, and Michel QUINTARD. On the ability of a darcy-scale model to capture wormhole formation during the dissolution of a porous medium. Journal of fluid Mechanics, 457:213–254, 2002.
- [73] Manuel Eduardo Gonzalez, James Benjamin Bloys, John E Lofton, Gregory Paul Pepin, Joseph H Schmidt, Carey John Naquin, Scot Thomas Ellis, Patrick E Laursen, et al. Increasing effective fracture gradients by managing wellbore temperatures. In IADC/SPE Drilling Conference. Society of Petroleum Engineers, 2004.
- [74] NR Goult. Reservoir stress path during depletion of norwegian chalk oil-fields. Petroleum Geoscience, 9(3):233–241, 2003.
- [75] J-R Grasso. Mechanics of seismic instabilities induced by the recovery of hydrocarbons. Pure and Applied Geophysics, 139(3-4):507–534, 1992.
- [76] Alan A Griffith. The phenomena of rupture and flow in solids. Philosophical transactions of the royal society of london. Series A, containing papers of a mathematical or physical character, 221:163–198, 1921.

- [77] Hongren Gu, Xiaowei Weng, Jeffrey B Lund, Mark G Mack, Utpal Ganguly, Roberto Suarez-Rivera, et al. Hydraulic fracture crossing natural fracture at nonorthogonal angles: a criterion and its validation. SPE Production & Operations, 27(01):20–26, 2012.
- [78] Yves Guéguen and Victor Palciauskas. Introduction to the physics of rocks. Princeton University Press, 1994.
- [79] Zhenghuai Guo, Furqan Hussain, Yildiray Cinar, et al. Experimental study of the permeability damage associated with fines production from a bituminous coal during water injection. In SPE European Formation Damage Conference and Exhibition. Society of Petroleum Engineers, 2015.
- [80] Mahdi Haddad and Kamy Sepehrnoori. Integration of xfem and czm to model 3d multiple-stage hydraulic fracturing in quasi-brittle shale formations: Solution-dependent propagation direction. In Proceedings of the AADE National Technical Conference and Exhibition, AADE2015, San Antonio, Texas, 8-9 April 2015, 2015.
- [81] Edwiwn L Hamilton. Low sound velocities in high-porosity sediments. The Journal of the Acoustical Society of America, 28(1):16–19, 1956.
- [82] S Harpalani and A Schraufnagel. Measurement of parameters impacting methane recovery from coal seams. International Journal of Mining and Geological Engineering, 8(4):369–384, 1990.

- [83] Bruce Hart\*. The calcites of shale plays: Why moving beyond quantitative mineralogy will improve project economics. In Unconventional Resources Technology Conference, Denver, Colorado, 25-27 August 2014, pages 878–886. Society of Exploration Geophysicists, American Association of Petroleum Geologists, Society of Petroleum Engineers, 2014.
- [84] F. Hecht. New development in freefem++. J. Numer. Math., 20(3-4):251–265, 2012.
- [85] Timo Heister, Mary F Wheeler, and Thomas Wick. A primal-dual active set method and predictor-corrector mesh adaptivity for computing fracture propagation using a phase-field approach. Computer Methods in Applied Mechanics and Engineering, 290:466–495, 2015.
- [86] Robert Heller and Mark Zoback. Adsorption of methane and carbon dioxide on gas shale and pure mineral samples. Journal of Unconventional Oil and Gas Resources, 8:14–24, 2014.
- [87] Richard G Hoagland, George T Hahn, and Alan R Rosenfield. Influence of microstructure on fracture propagation in rock. Rock Mechanics and Rock Engineering, 5(2):77–106, 1973.
- [88] ML Hoefner and H Scott Fogler. Pore evolution and channel formation during flow and reaction in porous media. AIChE Journal, 34(1):45–54, 1988.

- [89] George C Howard, CR Fast, et al. Optimum fluid characteristics for fracture extension. In Drilling and Production Practice. American Petroleum Institute, 1957.
- [90] King Hubbert, M and David G. Willis. Mechanics of hydraulic fracturing. 1957.
- [91] Jongsoo Hwang, Eric C Bryant, Mukul M Sharma, et al. Stress reorientation in waterflooded reservoirs. In SPE Reservoir Simulation Symposium. Society of Petroleum Engineers, 2015.
- [92] George R Irwin. Analysis of stresses and strains near the end of a crack traversing a plate. Journal of applied mechanics, 24(3):361–364, 1957.
- [93] John Conrad Jaeger, Neville GW Cook, and Robert Zimmerman. Fundamentals of rock mechanics. John Wiley & Sons, 2009.
- [94] Alfred R Jennings Jr, Lloyd G Jones, and Paul Shu. Method to improve matrix acidizing in carbonates, April 17 1990. US Patent 4,917,185.
- [95] Nitika Kalia and Vemuri Balakotaiah. Modeling and analysis of wormhole formation in reactive dissolution of carbonate rocks. Chemical Engineering Science, 62(4):919–928, 2007.
- [96] Piotr Kasza, Mariusz Dziadkiewicz, Marek Czupski, et al. From laboratory research to successful practice: a case study of carbonate formation emulsified acid treatments. In SPE International Symposium and Exhibition on Formation Damage Control. Society of Petroleum Engineers, 2006.

- [97] S Khristianovic and Y Zheltov. Formation of vertical fractures by means of highly viscous fluids. In Proc. 4th world petroleum congress, Rome, volume 2, pages 579–586, 1955.
- [98] Hyunwook Kim and William G Buttlar. Discrete fracture modeling of asphalt concrete. International Journal of Solids and Structures, 46(13):2593–2604, 2009.
- [99] Hyunwook Kim, Michael P Wagoner, and William G Buttlar. Simulation of fracture behavior in asphalt concrete using a heterogeneous cohesive zone discrete element model. Journal of Materials in Civil Engineering, 20(8):552–563, 2008.
- [100] Seunghee Kim and Seyyed Abolfazl Hosseini. Geological co 2 storage: Incorporation of pore-pressure/stress coupling and thermal effects to determine maximum sustainable pressure limit. Energy Procedia, 63:3339–3346, 2014.
- [101] Seunghee Kim and J Carlos Santamarina. Co2 geological storage: hydro-chemo-mechanical analyses and implications. Greenhouse Gases: Science and Technology, 4(4):528–543, 2014.
- [102] J. Kozeny. Ueber kapillare leitung des wassers im boden. Sitzungsber Akad. Wiss., 136(2a):271–306, 1927.
- [103] Robert L Kranz. Crack-crack and crack-pore interactions in stressed granite. In International Journal of Rock Mechanics and Mining Sciences &

Geomechanics Abstracts, volume 16, pages 37–47. Elsevier, 1979.

- [104] Robert L Kranz. Microcracks in rocks: a review. Tectonophysics, 100(1-3):449–480, 1983.
- [105] Stephen E Laubach. Practical approaches to identifying sealed and open fractures. AAPG bulletin, 87(4):561–579, 2003.
- [106] Brian Lawn and Rodney Wilshaw. Indentation fracture: principles and applications. Journal of materials science, 10(6):1049–1081, 1975.
- [107] Hunjoo P. Lee, Jon E. Olson, Jon Holder, Julia F. W. Gale, and Rodrick D. Myers. The interaction of propagating opening mode fractures with pre-existing discontinuities in shale. Journal of Geophysical Research: Solid Earth, 120(1):169–181, January 2015.
- [108] Hunjoo P Lee, Jon E Olson, Jon Holder, Julia FW Gale, and Rodrick D Myers. The interaction of propagating opening mode fractures with pre-existing discontinuities in shale. Journal of Geophysical Research: Solid Earth, 120(1):169–181, 2015.
- [109] Sang H Lee and Ahmad Ghassemi. Themo-poroelastic analysis of injection-induced rock deformation and damage evolution. In Proceedings Thirty-Fifth Workshop on Geothermal Reservoir Engineering, 2010.
- [110] Sanghyun Lee, Mary F Wheeler, and Thomas Wick. Pressure and fluid-driven fracture propagation in porous media using an adaptive finite ele-

- ment phase field model. *Computer Methods in Applied Mechanics and Engineering*, 305:111–132, 2016.
- [111] Sanghyun Lee, Mary F Wheeler, and Thomas Wick. Iterative coupling of flow, geomechanics and adaptive phase-field fracture including level-set crack width approaches. *Journal of Computational and Applied Mathematics*, 314:40–60, 2017.
- [112] Qinghua Lei, John-Paul Latham, and Chin-Fu Tsang. The use of discrete fracture networks for modelling coupled geomechanical and hydrological behaviour of fractured rocks. *Computers and Geotechnics*, 85:151–176, 2017.
- [113] Qinghua Lei, John-Paul Latham, Jiansheng Xiang, and Chin-Fu Tsang. Polyaxial stress-induced variable aperture model for persistent 3d fracture networks. *Geomechanics for Energy and the Environment*, 1:34–47, 2015.
- [114] Peter J Linstrom and William G Mallard. The nist chemistry webbook: A chemical data resource on the internet. *Journal of Chemical & Engineering Data*, 46(5):1059–1063, 2001.
- [115] Robert G Loucks and Stephen C Ruppel. Mississippian barnett shale: Lithofacies and depositional setting of a deep-water shale-gas succession in the fort worth basin, texas. *AAPG bulletin*, 91(4):579–601, 2007.
- [116] Kasper Lund, H Scott Fogler, CC McCune, and JW Ault. Acidizationii. the dissolution of calcite in hydrochloric acid. *Chemical Engineering Science*,

30(8):825–835, 1975.

- [117] P Maheshwari, RR Ratnakar, N Kalia, and V Balakotaiah. 3-d simulation and analysis of reactive dissolution and wormhole formation in carbonate rocks. Chemical Engineering Science, 90:258–274, 2013.
- [118] JR Major, P Eichhubl, TA Dewers, AS Urquhart, JE Olson, J Holder, et al. The effect of co 2-related diagenesis on geomechanical failure parameters: Fracture testing of co 2-altered reservoir and seal rocks from a natural analog at crystal geyser, utah. In 48th US Rock Mechanics/Geomechanics Symposium. American Rock Mechanics Association, 2014.
- [119] Ripudaman Manchanda, Eric C Bryant, Prateek Bhardwaj, Mukul M Sharma, et al. Strategies for effective stimulation of multiple perforation clusters in horizontal wells. In SPE Hydraulic Fracturing Technology Conference. Society of Petroleum Engineers, 2016.
- [120] D Marcial, P Delage, and YJ Cui. A laboratory study of the self sealing behaviour of a compacted sand–bentonite mixture. Geomechanics and Geoengineering: An International Journal, 1(1):73–85, 2006.
- [121] Joseph D Martinez, Kenneth S Johnson, and James T Neal. Sinkholes in evaporite rocks: surface subsidence can develop within a matter of days when highly soluble rocks dissolve because of either natural or human causes. American Scientist, 86(1):38–51, 1998.

- [122] Saikat Mazumder, Michael Scott, and Jessica Jiang. Permeability increase in bowen basin coal as a result of matrix shrinkage during primary depletion. *International Journal of Coal Geology*, 96:109–119, 2012.
- [123] Mark William McClure. Modeling and characterization of hydraulic stimulation and induced seismicity in geothermal and shale gas reservoirs. PhD thesis, Stanford University Stanford, California, 2012.
- [124] Darren McDuff, Chris E Shuchart, Shalawn Jackson, Dieter Postl, James Seay Brown, et al. Understanding wormholes in carbonates: Unprecedented experimental scale and 3-d visualization. In SPE Annual Technical Conference and Exhibition. Society of Petroleum Engineers, 2010.
- [125] Chester R McKee, Amar C Bumb, and Robert A Koenig. Stress-dependent permeability and porosity of coal. In International Coalbed Methane Symposium, University of Alabama, Tuscaloosa, Alabama, pages 183–193, 1987.
- [126] Andro Mikelić, Mary F Wheeler, and Thomas Wick. A phase field approach to the fluid filled fracture surrounded by a poroelastic medium. ICES Report, pages 13–15, 2013.
- [127] Andro Mikelić, Mary F Wheeler, and Thomas Wick. A phase-field method for propagating fluid-filled fractures coupled to a surrounding porous medium. Multiscale Modeling & Simulation, 13(1):367–398, 2015.
- [128] Ki-Bok Min, Jonny Rutqvist, Chin-Fu Tsang, and Lanru Jing. Stress-dependent permeability of fractured rock masses: a numerical study. International

Journal of Rock Mechanics and Mining Sciences, 41(7):1191–1210, 2004.

- [129] DH Mofat and KE Weale. Sorption by coal of methane at high pressure. Fuel, 34:449–462, 1955.
- [130] Robert Lloyd Moore, Debbie Fay Loftin, Ian D Palmer, et al. History matching and permeability increases of mature coalbed methane wells in san juan basin. In SPE Asia Pacific Oil and Gas Conference and Exhibition. Society of Petroleum Engineers, 2011.
- [131] Witold Nowacki. Thermoelasticity. Elsevier, 2013.
- [132] Victoria U Okotie, Robert L Moore, et al. Well-production challenges and solutions in a mature, very-low-pressure coalbed-methane reservoir. SPE Production & Operations, 26(02):149–161, 2011.
- [133] JE Olson et al. Multi-fracture propagation modeling: Applications to hydraulic fracturing in shales and tight gas sands. In The 42nd US rock mechanics symposium (USRMS). American Rock Mechanics Association, 2008.
- [134] ASTM Committee E08 on Fatigue and Fracture. Standard test method for measurement of fracture toughness. ASTM International, 2011.
- [135] Hisanao Ouchi et al. Development of peridynamics-based hydraulic fracturing model for fracture growth in heterogeneous reservoirs. PhD thesis, 2016.

- [136] Hisanao Ouchi, Amit Katiyar, Jason York, John T Foster, and Mukul M Sharma. A fully coupled porous flow and geomechanics model for fluid driven cracks: a peridynamics approach. *Computational Mechanics*, 55(3):561–576, 2015.
- [137] Ian Palmer. Permeability changes in coal: analytical modeling. *International Journal of Coal Geology*, 77(1):119–126, 2009.
- [138] Ian Palmer, John Mansoori, et al. How permeability depends on stress and pore pressure in coalbeds: a new model. In *SPE Annual Technical Conference and Exhibition*. Society of Petroleum Engineers, 1996.
- [139] Ian D Palmer, Zissis Andrew Moschovidis, John Robert Cameron, et al. Modeling shear failure and stimulation of the barnett shale after hydraulic fracturing. In *SPE Hydraulic Fracturing Technology Conference*. Society of Petroleum Engineers, 2007.
- [140] Zhejun Pan and Luke D Connell. Modelling permeability for coal reservoirs: a review of analytical models and testing data. *International Journal of Coal Geology*, 92:1–44, 2012.
- [141] Mohan KR Panga, Murtaza Ziauddin, and Vemuri Balakotaiah. Two-scale continuum model for simulation of wormholes in carbonate acidization. *AIChE journal*, 51(12):3231–3248, 2005.
- [142] Tad W Patzek, Frank Male, and Michael Marder. Gas production in the barnett shale obeys a simple scaling theory. *Proceedings of the National*

Academy of Sciences, 110(49):19731–19736, 2013.

- [143] TK Perkins, LR Kern, et al. Widths of hydraulic fractures. Journal of Petroleum Technology, 13(09):937–949, 1961.
- [144] T. Petrie. Following oil : four decades of cycle-testing experiences and what they foretell about U.S energy independence. 2014.
- [145] Sandrine Portier, Laurent André, and François-D Vuataz. Review on chemical stimulation techniques in oil industry and applications to geothermal systems. Engine, work package, 4:32, 2007.
- [146] R&amp Puri and JP Seidle. Measurement of stress-dependent permeability in coal and its influence on coalbed methane production. In Situ;(United States), 16(3), 1992.
- [147] Dianne Rahm. Regulating hydraulic fracturing in shale gas plays: The case of texas. Energy Policy, 39(5):2974–2981, 2011.
- [148] Muthukumarappan Ramurthy, Rudy E Rogers, and Dana Weida. Analysis of the success of cavity completions in the fairway zone of the san juan basin. In SPE Rocky Mountain regional meeting, pages 215–222, 1999.
- [149] François Renard, Dominique Bernard, Jacques Desrues, and Audrey Ougier-Simonin. 3d imaging of fracture propagation using synchrotron x-ray microtomography. Earth and Planetary Science Letters, 286(1):285–291, 2009.

- [150] PJ Reucroft and AR Sethuraman. Effect of pressure on carbon dioxide induced coal swelling. *Energy & Fuels*, 1(1):72–75, 1987.
- [151] James R Rice et al. A path independent integral and the approximate analysis of strain concentration by notches and cracks. ASME, 1968.
- [152] Alex J Rinehart, Joseph E Bishop, and Thomas Dewers. Fracture propagation in indiana limestone interpreted via linear softening cohesive fracture model. *Journal of Geophysical Research: Solid Earth*, 120(4):2292–2308, 2015.
- [153] Alex J Rinehart, Thomas A Dewers, Scott T Broome, and Peter Eichhubl. Effects of co<sub>2</sub> on mechanical variability and constitutive behavior of the lower tuscaloosa formation, cranfield injection site, usa. *International Journal of Greenhouse Gas Control*, 53:305–318, 2016.
- [154] Ernesto Meneses Rioseco, Jörn Löhken, Rüdiger Schellschmidt, and Torsten Tischner. 3-d geomechanical modeling of the stress field in the north german basin: Case study genesys-borehole gt1 in hanover groß-buchholz. In Proceedings, Thirty-eighth Workshop on Geothermal Reservoir Engineering. Stanford, USA, 2013.
- [155] Nuno Rodrigues, Peter R Cobbold, Helge Loseth, and Gilles Ruffet. Widespread bedding-parallel veins of fibrous calcite (beef') in a mature source rock (vaca muerta fm, neuquén basin, argentina): evidence for overpressure and horizontal compression. *Journal of the Geological Society*, 166(4):695–709, 2009.

- [156] Jeremy Rohmer and Darius M Seyedi. Coupled large scale hydromechanical modelling for caprock failure risk assessment of co2 storage in deep saline aquifers. [Oil & Gas Science and Technology–Revue de lInstitut Français du Pétrole](#), 65(3):503–517, 2010.
- [157] Nicolas P Roussel, Mukul M Sharma, et al. Optimizing fracture spacing and sequencing in horizontal-well fracturing. [SPE Production & Operations](#), 26(02):173–184, 2011.
- [158] Nicolas Patrick Roussel, Mukul M Sharma, et al. Strategies to minimize frac spacing and stimulate natural fractures in horizontal completions. In [SPE Annual Technical Conference and Exhibition](#). Society of Petroleum Engineers, 2011.
- [159] JT Rutledge, WS Phillips, and MJ Mayerhofer. Faulting induced by forced fluid injection and fluid flow forced by faulting: An interpretation of hydraulic-fracture microseismicity, carthage cotton valley gas field, texas. [Bulletin of the Seismological Society of America](#), 94(5):1817–1830, 2004.
- [160] J Rutqvist. Fractured rock stress-permeability relationships from in situ data and effects of temperature and chemical-mechanical couplings. [Geofluids](#), 15(1-2):48–66, 2015.
- [161] Jonny Rutqvist, Lennart Börgesson, Masakazu Chijimatsu, Jan Hernelind, Lanru Jing, Akira Kobayashi, and Son Nguyen. Modeling of damage, permeability changes and pressure responses during excavation of the tsx tunnel

- in granitic rock at url, canada. Environmental Geology, 57(6):1263–1274, 2009.
- [162] EH Rutter. Pressure solution in nature, theory and experiment. Journal of the Geological Society, 140(5):725–740, 1983.
- [163] SPE Samiha Morsy, JJ Sheng, Mohamed Y Soliman, and Roland O Ezewu. Impact of matrix acidizing on shale formations. 2013.
- [164] Rafael Sandrea. Evaluating production potential of mature us oil, gas shale plays. Oil & gas journal, 110(12), 2012.
- [165] Johannes Schindelin, Ignacio Arganda-Carreras, Erwin Frise, Verena Kaynig, Mark Longair, Tobias Pietzsch, Stephan Preibisch, Curtis Rueden, Stephan Saalfeld, Benjamin Schmid, et al. Fiji: an open-source platform for biological-image analysis. Nature methods, 9(7):676–682, 2012.
- [166] Donald T Secor. Role of fluid pressure in jointing. American Journal of Science, 263(8):633–646, 1965.
- [167] Paul Segall and Shaun D Fitzgerald. A note on induced stress changes in hydrocarbon and geothermal reservoirs. Tectonophysics, 289(1):117–128, 1998.
- [168] JM Segura, QJ Fisher, AJL Crook, M Dutko, JG Yu, S Skachkov, DA Angus, JP Verdon, and JM Kendall. Reservoir stress path characterization and its implications for fluid-flow production simulations. Petroleum Geoscience, 17(4):335–344, 2011.

- [169] APS Selvadurai and AP Suvorov. Thermo-poroelasticity and Geomechanics. 2017.
- [170] Varahanaresh Sesetty, A Ghassemi, et al. Simulation of hydraulic fractures and their interactions with natural fractures. In 46th US Rock Mechanics/Geomechanics Symposium. American Rock Mechanics Association, 2012.
- [171] Antonin Settari et al. Modeling of acid-fracturing treatments. SPE Production & Facilities, 8(01):30–38, 1993.
- [172] MM Sharma, R Manchanda, et al. The role of induced un-propped (iu) fractures in unconventional oil and gas wells. In SPE Annual Technical Conference and Exhibition. Society of Petroleum Engineers, 2015.
- [173] Ji-Quan Shi, Sevket Durucan, et al. A model for changes in coalbed permeability during primary and enhanced methane recovery. SPE Reservoir Evaluation & Engineering, 8(04):291–299, 2005.
- [174] Ji-Quan Shi, Sevket Durucan, and Sohei Shimada. How gas adsorption and swelling affects permeability of coal: a new modelling approach for analysing laboratory test data. International Journal of Coal Geology, 128:134–142, 2014.
- [175] JQ Shi and S Durucan. Drawdown induced changes in permeability of coalbeds: a new interpretation of the reservoir response to primary recovery. Transport in porous media, 56(1):1–16, 2004.

- [176] Do H Shin, Mukul M Sharma, et al. Factors controlling the simultaneous propagation of multiple competing fractures in a horizontal well. In SPE Hydraulic Fracturing Technology Conference. Society of Petroleum Engineers, 2014.
- [177] Hosung Shin and J Carlos Santamarina. Mineral dissolution and the evolution of  $k_0$ . Journal of Geotechnical and Geoenvironmental Engineering, 135(8):1141–1147, 2009.
- [178] Igor Shovkun and D. Nicolas Espinoza. Fracture propagation in heterogeneous porous media: pore-scale effects of mineral dissolution. 2018.
- [179] Igor Shovkun and D Nicolas Espinoza. Geomechanical implications of dissolution of mineralized natural fractures in shale formations. Journal of Petroleum Science and Engineering, 160:555–564, 2018.
- [180] Robin Singh, Krishna Panthi, and Kishore K Mohanty. Microencapsulation of acids by nanoparticles for acid treatment of shales. Energy & Fuels, 31(11):11755–11764, 2017.
- [181] Ian Naismith Sneddon and Morton Lowengrub. Crack problems in the classical theory of elasticity. 1969, 221 P, 1969.
- [182] IN Sneddon and HA Elliot. The opening of a griffith crack under internal pressure. Quart. Appl. Math, 4(3):262–267, 1946.

- [183] Hiroki Sone and Mark D Zoback. Mechanical properties of shale-gas reservoir rockspart 1: Static and dynamic elastic properties and anisotropy. *Geophysics*, 78(5):D381–D392, 2013.
- [184] Werner Stumm and James J Morgan. Chemical equilibria and rates in natural waters. *Aquatic chemistry*, page 1022, 1996.
- [185] R Suarez-Rivera, J Burghardt, E Edelman, S Stanchits, A Surdi, et al. Geomechanics considerations for hydraulic fracture productivity. In 47th US Rock Mechanics/Geomechanics Symposium. American Rock Mechanics Association, 2013.
- [186] Yuhao Sun, Michael Aman, and D Nicolas Espinoza. Assessment of mechanical rock alteration caused by co 2-water mixtures using indentation and scratch experiments. *International Journal of Greenhouse Gas Control*, 45:9–17, 2016.
- [187] Zhuang Sun, Matthew T Balhoff, D Nicolas Espinoza, et al. Discrete element modeling of micro-scratch tests on rocks altered by co 2. In 51st US Rock Mechanics/Geomechanics Symposium. American Rock Mechanics Association, 2017.
- [188] Peter L Swanson. Subcritical crack growth and other time-and environment-dependent behavior in crustal rocks. *Journal of Geophysical Research: Solid Earth*, 89(B6):4137–4152, 1984.

- [189] Chee P Tan, Brian G Richards, Sheik S Rahman, Rivano Andika, et al. Effects of swelling and hydralional stress in shales on wellbore stability. In SPE Asia Pacific Oil and Gas Conference and Exhibition. Society of Petroleum Engineers, 1997.
- [190] Cedric Taylor and P Hood. A numerical solution of the navier-stokes equations using the finite element technique. Computers & Fluids, 1(1):73–100, 1973.
- [191] Kevin C Taylor, Hisham A Nasr-El-Din, Sudhir Mehta, et al. Anomalous acid reaction rates in carbonate reservoir rocks. SPE Journal, 11(04):488–496, 2006.
- [192] Lawrence W Teufel, Douglas W Rhett, Helen E Farrell, et al. Effect of reservoir depletion and pore pressure drawdown on in situ stress and deformation in the ekofisk field, north sea. In The 32nd US Symposium on Rock Mechanics (USRMS). American Rock Mechanics Association, 1991.
- [193] Zhiwei Tian, Huilin Xing, Yunliang Tan, and Jinfang Gao. A coupled lattice boltzmann model for simulating reactive transport in co<sub>2</sub> injection. Physica A: Statistical Mechanics and Its Applications, 403:155–164, 2014.
- [194] Alessandro Toscano, Filiberto Bilotti, Francesco Asdrubali, Claudia Guatari, Luca Evangelisti, and Carmine Basilicata. Recent trends in the world gas market: Economical, geopolitical and environmental aspects. Sustainability, 8(2):154, 2016.

- [195] Divyendu Tripathi, Maysam Pournik, et al. Effect of acid on productivity of fractured shale reservoirs. In SPE/AAPG/SEG Unconventional Resources Technology Conference. Society of Petroleum Engineers, 2014.
- [196] Chin-Fu Tsang, Frederic Bernier, and Christophe Davies. Geohydromechanical processes in the excavation damaged zone in crystalline rock, rock salt, and indurated and plastic clays in the context of radioactive waste disposal. International Journal of Rock Mechanics and Mining Sciences, 42(1):109–125, 2005.
- [197] U.S. Department of Energy. International energy outlook 2016. Technical report, May 2016.
- [198] P Valko and MJ Economides. Hydraulic fracture mechanics, 1995.
- [199] Peter Valko, MJ Economides, et al. Fracture height containment with continuum damage mechanics. In SPE Annual Technical Conference and Exhibition. Society of Petroleum Engineers, 1993.
- [200] Tony Waltham, Fred G Bell, and Martin G Culshaw. Sinkholes and subsidence: karst and cavernous rocks in engineering and construction. Springer Science & Business Media, 2007.
- [201] X Wang, Q Lei, L Lonergan, H Jourde, O Gosselin, and J Cosgrove. Heterogeneous fluid flow in fractured layered carbonates and its implication for generation of incipient karst. Advances in Water Resources, 107:502–516, 2017.

- [202] Norman Warpinski, Robert C Kramm, James R Heinze, Charles Kennedy Waltman, et al. Comparison of single-and dual-array microseismic mapping techniques in the barnett shale. In SPE Annual Technical Conference and Exhibition. Society of Petroleum Engineers, 2005.
- [203] MY Wei, JS Liu, et al. Permeability evolution of damaged coal near a wellbore. In ISRM International Symposium-8th Asian Rock Mechanics Symposium. International Society for Rock Mechanics, 2014.
- [204] Alyssa K Wickard\*, R Douglas Elmore, and Gerhard Heij. A diagenetic study of the wolfcamp shale, midland basin, west texas. In Unconventional Resources Technology Conference, San Antonio, Texas, 1-3 August 2016, pages 2421–2435. Society of Exploration Geophysicists, American Association of Petroleum Geologists, Society of Petroleum Engineers, 2016.
- [205] TD Wiles and JH Curran. A general 3-d displacement discontinuity method. In Proceedings of the Fourth International Conference on Numerical Methods in Geomechanics. Z. Eisenstein, ed. Edmonton, Canada. Rotterdam: AA Balkema, pages 103–111, 1982.
- [206] Adam Wilson et al. Scale inhibitor works to prevent reprecipitation of calcium sulfate. Journal of Petroleum Technology, 67(09):154–155, 2015.
- [207] Keliu Wu. Apparent permeability for gas flow in shale reservoirs coupling effects of gas diffusion and desorption. Unconventional Resources Technology Conference (URTEC), 2014.

- [208] Weiwei Wu, Mukul Mani Sharma, et al. Acid fracturing shales: Effect of dilute acid on properties and pore structure of shale. In SPE Hydraulic Fracturing Technology Conference. Society of Petroleum Engineers, 2015.
- [209] Yu-Shu Wu, Karsten Pruess, et al. Gas flow in porous media with klinkenberg effects. Transport in porous Media, 32(1):117–137, 1998.
- [210] TH Yang, LG Tham, CA Tang, ZZ Liang, and Y Tsui. Influence of heterogeneity of mechanical properties on hydraulic fracturing in permeable rocks. Rock mechanics and rock engineering, 37(4):251–275, 2004.
- [211] Yao Yao, Shekhar V Gosavi, Kevin H Searles, Tim K Ellison, et al. Cohesive fracture mechanics based analysis to model ductile rock fracture. In 44th US Rock Mechanics Symposium and 5th US-Canada Rock Mechanics Symposium. American Rock Mechanics Association, 2010.
- [212] Elizabeth H Yoffe. Lxxv. the moving griffith crack. The London, Edinburgh, and Dublin Philosophical Magazine and Journal of Science, 42(330):739–750, 1951.
- [213] Jun Yoneda, Akira Masui, Yoshihiro Konno, Yusuke Jin, Kosuke Egawa, Masato Kida, Takuma Ito, Jiro Nagao, and Norio Tenma. Mechanical properties of hydrate-bearing turbidite reservoir in the first gas production test site of the eastern nankai trough. Marine and Petroleum Geology, 66:471–486, 2015.

- [214] Wei Yu and Kamy Sepehrnoori. Simulation of gas desorption and geomechanics effects for unconventional gas reservoirs. *Fuel*, 116:455–464, 2014.
- [215] XP Zhao, RP Young, et al. Numerical simulation of seismicity induced by hydraulic fracturing in naturally fractured reservoirs. In SPE Annual Technical Conference and Exhibition. Society of Petroleum Engineers, 2009.
- [216] A Khristianovic Zheltov et al. 3. formation of vertical fractures by means of highly viscous liquid. In 4th World Petroleum Congress. World Petroleum Congress, 1955.
- [217] Y Zheltov and S Khristianovic. On the mechanism of hydraulic fractures of an oil-bearing stratum. *Izv. AN SSSR*, 5:3–41, 1955.
- [218] Goangseup Zi and Ted Belytschko. New crack-tip elements for xfem and applications to cohesive cracks. International Journal for Numerical Methods in Engineering, 57(15):2221–2240, 2003.
- [219] R Karl Zipf. Failure mechanics of multiple-seam mining interactions. In Proceedings of the 24th International Conference on Ground Control in Mining, West Virginia University, Morgantown, WV, 2–4 August 2005, pages 93–106, 2005.
- [220] Mark D Zoback. Reservoir geomechanics. Cambridge University Press, 2010.

- [221] Mark D Zoback and Steven M Gorelick. Earthquake triggering and large-scale geologic storage of carbon dioxide. Proceedings of the National Academy of Sciences, 109(26):10164–10168, 2012.
- [222] Mark D Zoback, Arjun Kohli, Indrajit Das, Mark William Mcclure, et al. The importance of slow slip on faults during hydraulic fracturing stimulation of shale gas reservoirs. In SPE Americas Unconventional Resources Conference. Society of Petroleum Engineers, 2012.
- [223] Mark D Zoback and Jens C Zinke. Production-induced normal faulting in the valhall and ekofisk oil fields. In The Mechanism of Induced Seismicity, pages 403–420. Springer, 2002.